國立臺灣大學理學院物理學系

博士論文

Department of Physics College of Science

National Taiwan University

Doctor Thesis

以有限時域差分法與高效率化介電函數研究核殼奈米結構的侷域性表面電漿模態

Study of Localized Plasmon Modes in Core-shell Nanostructures by using FDTD Method with an Efficient Dielectric Function

呂駿佑

Chun-Yu Lu

指導教授：張顏暉 博士

Advisor: Yuan-Huei Chang, Ph.D.

中華民國99年11月

November, 2010

國立臺灣大學博士學位論文
口試委員會審定書

以有限時域差分法與高效率化介電函數研究核殼奈米結構的

侷域性表面電漿模態

Study of Localized Plasmon Modes in Core-shell Nanostructures

by Using FDTD Method with An Efficient Dielectric Function

本論文係呂駿佑君（f95222042）在國立臺灣大學物理學系、所完成之博士學位論文，於民國 99 年 11 月 24 日承下列考試委員審查通過及口試及格，特此證明

口試委員：

張顧暉（簽名）

（指導教授）

誌謝

轉眼間，在台大的碩、博士班生涯結束了，人生將邁入另一個嶄新的里程。非常感謝張老師對我的指導與照顧，使我在學業跟待人處世上都受益良多。另外也很感謝陳永芳老師和梁啟德老師在我每次報告及畢業口試時，都能給予寶貴的意見。此外也很感謝口試委員郭光宇教授、賴暎杰教授、以及魏培坤研究員，在畢業口試及論文上給予極寶貴的意見，使得這本論文更加地完整。

從進來台大到畢業這期間要感謝的人真是太多人，從學長、學姊到學弟、學妹等都是我的貴人。感謝大家寶貴的幫助及意見，使我學習到不少知識及技術。感謝邱國斌、跟莊佩蓁，從碩班陪伴我到畢業，不論是生活上跟精神上都給予我極大的幫助，使我能專心於研究上。感謝蔡定平老師在我研究所開始的一兩年所給予我的指導，感謝軒逸、日新、辛宇、俊昌、小戴、俊穎、昱位，你們在實驗室的支援與幫忙，讓我可以研究上更加順利！還有仲良、志瑋、群雄、函宇、勇廷、威宏…等，謝謝你們的幫助才使這本論文更加豐富。感謝我的朋友律行、志宏、明宏、家瑋、旻璇、羽婕，謝謝你們的鼓勵讓我有動力繼續奮鬥下去。

最後我要感謝我的父母，從小對我的栽培與細心照顧，讓我可以放心在學校做研究。感謝大哥、三弟分擔家計，讓我可以無後顧之憂完成博士學位。

摘要

由於其侷域性表面電漿模態會與光有強烈交互作用，貴重金屬奈米顆粒之光學性質已成為一重要研究領域。 製程技術的進步使得我們能夠設計擁有多種形狀跟功能的核殼結構，像是奈米米、奈米環和奈米核殼,這些核殼結構由他們在光電、生物和電子設備上的應用吸引到很多注意。這份論文研究光與電介質核金屬殼奈米結構的交互作用，在論文內所使用的模擬的工具是圖形處理器單位化的有限時域差分法，圖形處理器可以加速我們模擬的效率並且減少模擬時間。 此外，一個新且有效率的介電函數模型被併入在我們有限時域差分法中，此模擬結果可以準確地描述金跟銀的色散在波長 180 奈米到 2000 奈米之間，於是我們使用此有限時域差分法研究電介質/金屬核殼圓柱對的侷域性表面電漿模態。

首先，我們先著重一對電介質/金屬核殼奈米圓柱的侷域性電漿模態。 模擬的結果發現避雷針作用跟混成電漿模態是兩個造成強烈電場分佈的重要因素，同時我們也利用相位延遲效應來激發無偶極矩的電漿模態。 除了模擬電場分佈跟消散光譜外，我們也研究能量流與電漿模態偶合的關係，結果發現與電漿模態有關的光學奇異點可以被發現在一對核殼奈米圓柱中的，光旋渦與鞍點可以在光與這圓柱對作用的同相對稱偶極矩模之能量流中發現，其中光漩渦的轉動方向可以藉由變化兩圓柱間的寬度以及介質核的光學常數來控制。 最後，我們延伸對於電介質/金屬核殼圓柱對的討論從一對到三對，研究結果顯示電介質/金屬核殼圓柱對可以同時作為表面增強拉曼散射和表面增強紅外吸收光譜的選擇。

Abstract

Noble metal nanoparticles (NPs) are well-known to exhibit a strong interaction with light due to the excitation of localized surface plasmons. Recent advances in nanofabrication have enabled us to design the nanostructures with different shapes and functionalities, such as nanorices, nanorings, and nanoshells. These core-shell nanostructures have attracted much attention due to their applications in opto-electric, biological, and electronic devices. This dissertation reports the studies of the interactions between the light and dielectric-core metallic-shell nanostructures. The simulation tool used in this dissertation is Graphic-Process-Unit-Based (GPU-Based) finite-difference time-domain (FDTD) method. The GPU is graphic processor unit that can greatly speed up our simulation efficiency and reduce simulation time. In addition, a new and efficient dielectric function model was developed and incorporated into our FDTD, and the simulation result can describe accurately the dispersion of gold and silver in the wavelength range between 180nm and 2000nm. This FDTD tool was then used to study the localized plasmon modes in dielectric-core gold-shell nanocylinders.

First, we focus on the plasmon modes of a core-shell nanocylinder pair. The simulations results show the lightning-rod effect and hybridized plasmons are two important factors in enhancing the electric field. We also studied the excitation of non-dipolar plasmon modes by using the phase retardation effect. In addition to simulating the extinction spectra and electric field distributions, the relation of energy flows and localized plasmon modes is also studied. Optical singularities associated with plasmon modes are found to exist in a core-shell nanocylinder pair. The optical vortices as well

as saddle points can be observed in the energy flow pattern of light interacting with the core-shell nanocylinder pair in its in-phase symmetric dipolar plasmon mode. The rotating direction of the optical vortices can be tuned by varying the width of the gap between the nanocylinder pair and the value of the permittivity of the dielectric core. Finally, we extend our studies on core-shell nanocylinder pairs from one pair to three pairs. The results show the core-shell nanostructures have a property that makes it an ideal candidate for both surface enhanced Raman scattering (SERS) and surface enhanced infrared absorption spectroscopes (SEIRA).

Publication list

1. **J. Y. Lu** and Y. H. Chang," Optical singularities associated with the energy flow of two closely spaced core-shell nanocylinders", Optics Express **17**, 19451 (2009).
2. **J. Y. Lu** and Y. H. Chang, "Implementation of an efficient dielectric function into the finite difference time domain method for simulating the coupling between localized surface plasmons of nanostructures", Superlattices and Microstructures **47**, 160 (2010).
3. H. Y. Chao, J. H. Cheng, **J. Y. Lu**, Y. H. Chang, C. L. Cheng, Y. F. Chen and C. T. Wu, "Growth and characterization of type-II ZnO/ZnTe core-shell nanowire arrays for solar cell applications", Superlattices and Microstructures **47**, 160 (2010).
4. **J. Y. Lu** and Y. H. Chang, "The lightening mode in a core-shell nanocylinder dimer", Optics Communications **283**, 2627 (2010).
5. H. Y. Chao, S. H. You, **J. Y. Lu**, J. H. Cheng, Y. H. Chang, and C. T. Wu "The growth and characterization of ZnO/ZnTe core-shell nanowires and the electrical properties of ZnO/ZnTe core-shell nanowires field effect transistor", J. of Nanoscience and Nanotechnology, (in press) (2010).
6. **J. Y. Lu,** H.Y. Chao, J.C. Wu, S.Y. Wei, Y.H. Chang, S.C. Chen, "Retardation-induced plasmon modes in silica-core gold-shell nanocylinder pair", Physica E **42**, 2583 (2010).
7. H. Y. Chao, J. H. Cheng, **J. Y. Lu**, Y. H. Chang, Y. F. Chen, C.-T. Liang, "Growth and characterization of ZnO/ZnSe core-shell nanowires and their applications", submitted to Nanoscale Research Letters.

8. **J. Y. Lu**, H. Y. Chao, J. C. Wu, S. Y. Wei, and Y. H. Chang, “Metallic-shell nanocylinder arrays for surface enhanced spectroscopes”, submitted to Nanoscale Research Letters.

Contents

List of Figures

Chapter 1 Introduction

Chapter 2 Theory

Chapter 3 Finite-difference time-domain method

Chapter 4 Implementation of an efficient dielectric function into finite difference time domain method for simulating the coupling between localized surface plasmon of nanostructures

Chapter 5 The lightning-rod mode in a core-shell nanocylinder dimer

Chapter 6 Retardation-effect-induced plasmon modes in a silica-core gold-shell nanocylinder pair

Chapter 7 Optical singularities associated with the energy flow of two closely spaced core-shell nanocylinders

Chapter 8 Multiple Metallic-shell nanocylinders for surface enhanced spectroscopes

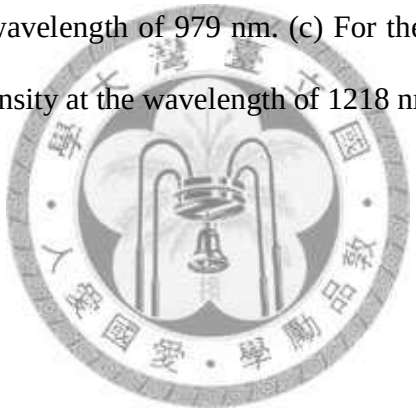

List of Tables

Chapter 1

Introduction

1.1 Surface plasmon oscillations of Metals

Physicist Richard P. Feynman once said “There’s plenty of room at the bottom”, which implies that fabricating tiny materials and studying phenomena of them have been a trend in science and technology. Since R. W. Wood [1] discovered the strange reflection spectra of optical diffraction gratings in 1902, the optical properties of metals in nanosize has been attractive to the scientists and engineers. The phenomenon found by R. W. Wood was explained by U. Fano [2], who describes this result as the electromagnetic wave propagating along the surface of metals. This explanation is known as surface plasmon theory. Since then, the interactions between metals and electromagnetic waves become an important topic in optics.

As the fabrication of technology has been improved, the feasibility of nanostructures has enabled us to design the devices to control electromagnetic wave in nanoscale region. Surface plasmons have been employed in a wide spectrum of studies, which are ranged from electrochemistry [3], biosensing [4-6], solar cells [7-8], to scanning tunneling miscroscopy [9]. Recently, another interesting effect of light interacting with structured metal has been discovered: the enhanced transmission through periodic arrays of subwavelength hole in optically metallic film can be orders of magnitudes larger than expected from the standard aperture theory [10]. Apart from its fundamental theory, this

extraordinary transmission effect can be applied in subwavelength photolithography [11], near-field microscopy, and flat-panel displays.

1.2 Localized surface plasmon oscillations of metal nanoparticles and their applications

Individual metallic nanoparticles also exhibit unusual optical properties, which are called localized surface plasmon (LSP) [12]. Plasmonic structures are often made of noble metals such as gold (Au) and silver (Ag), because these metals are stable under ambient conditions and show strong localized surface plasmon resonances. The localized surface plasmon (LSP) means that the non-propagated excitations of the conduction electrons at the surface of metallic particles. Significantly enhanced scattering and absorption at their LSP resonances can be applied in optical imaging and photothermal therapy. Furthermore, the intense electric field intensity near the surface of the metal nanoparticles generated by the LSP can be utilized for the surface enhanced spectroscopies (SES) [13-14].

The most widely used surface enhanced spectroscopy (SES) is surface enhanced Raman scattering (SERS), where the electromagnetic enhancement factor is proportional to the fourth power of the electric field incident on the molecule [15-16]. The typically quoted values of the SERS enhancement factor, i.e., the ratio between a measured Raman cross section in the presence and in the absence of a metal surface, ranged from 10^3 and 10^6 in the case of silver colloids [17]. Later, new single-molecule SERS experiments on Ag and Au colloids have indicated that a much larger enhancement factor occurring under special

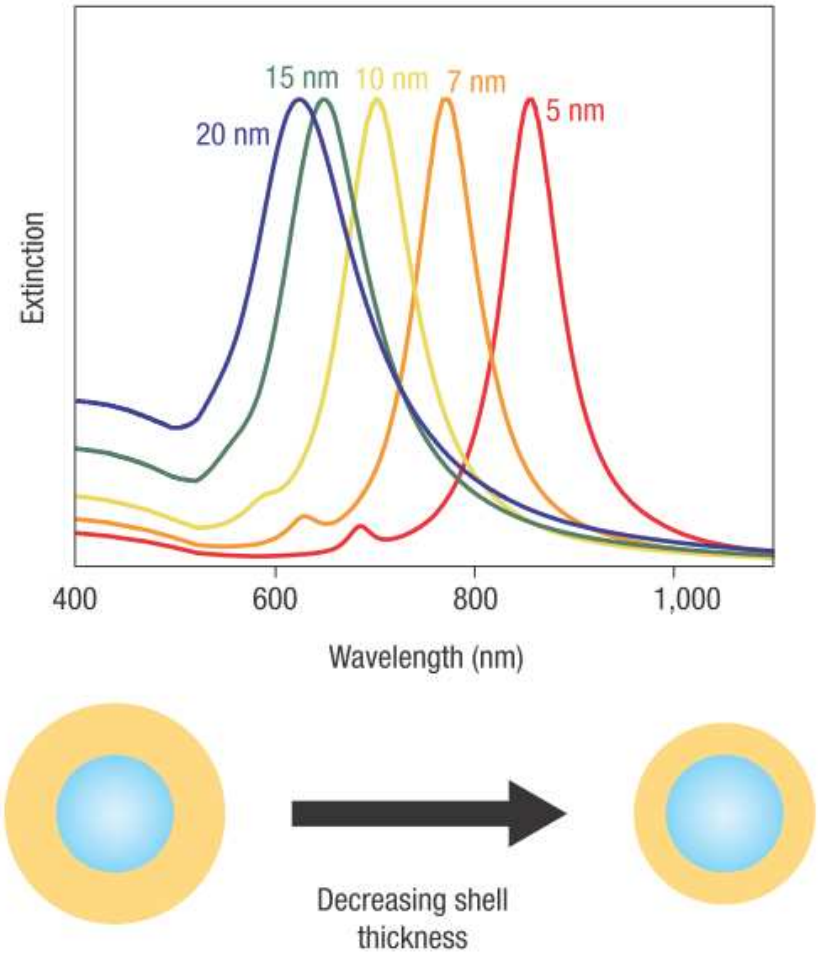

Figure 1.1 The plasmon resonances of a 120-nm-diameter silica core coated with varying thicknesses of gold shell. Note the blue shift in the plasmon resonance as the size of the gold layer increases from 5 nm to 20 nm. (Surbhi LaL et al. Nature Photonics, **1**, 641-648 (2007))

circumstances [16-18]. It's now well accepted that almost all single molecule SERS signals detected in colloidal aggregates result from pairs of directly adjacent metallic nanoparticles and not from single isolated metallic nanoparticles. The region between nanoparticle pairs contains hot spots that give rise to the enormous enhancement factors, which are required to observe single molecule SERS.

Recent advances in nanofabrication have enabled us to design the nanostructures with different shapes and functionalities, such as nanorices [19], nanorings [20], and nanoshells [21]. Compared to solid metallic particles, these core-shell nanostructures exhibit highly tunable plasmon modes, which is shown in figure 1.1, that can be tuned over an extended wavelength range between visible and near infrared regions and the variation of the plasmon resonance wavelength is interpreted as originating from coupling of localized surface plasmon modes at the inner and outer surfaces of the core-shell structure [20,22]. Since the first fabrication of the nanoshells in 1998 [23], the metallic nanoshell has been studied intensively in various imaging and spectroscopic applications, by employing the high tunability in its plasmon resonance frequency as well as the enhanced local fields in the vicinity of the nanoshells [24–26]. In particular, surface enhanced Raman scattering (SERS) from these nanoshell substrates has been studied systematically in several recent works published by the Halas group [21-23, 26]. In these studies, SERS was observed from either solutions containing these metallic nanoshells or nanoshell thin filmsubstrates [27], with enhancement at least as strong as those obtained from colloidal aggregates of metallic particles. For example, the enhancement factor of about 10^9 has been achieved with SERS for para-mercaptoaniline

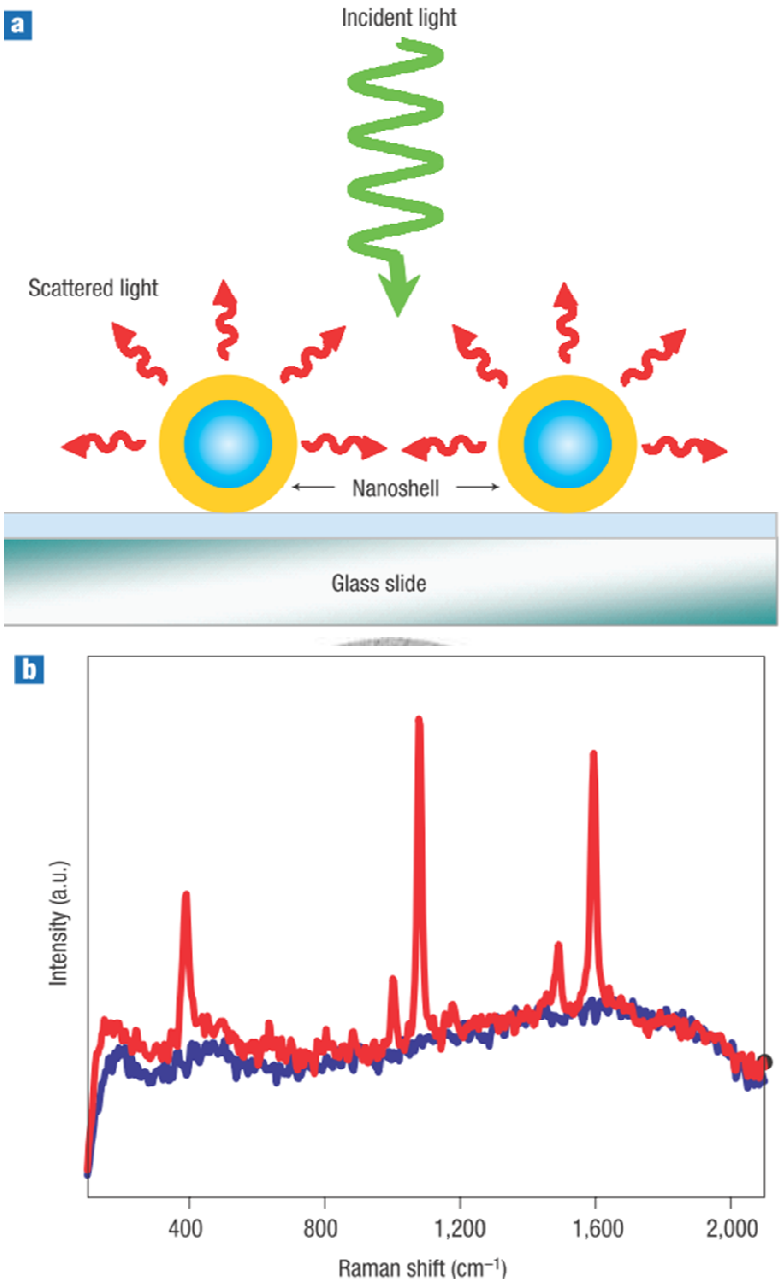

Figure 1.2 Surface enhanced Raman scattering spectroscopy: (a) the schematic geometry for gold-nanoshell substrate and (b) Raman spectrum of p-mercaptoaniline collected with no nanoshells (blue) and SERS spectra with nanoshells. (Surbhi LaL et al. Nature Photonics, **1**, 641 (2007)).

(pMA) on gold nanoshells in figure 1.2. Furthermore, SERS was achievable with infrared nanoshells, with the tenability of resonance wavelengths depending crucially on the ratio of the inner and outer shell radii as well as the shell thickness [28].

Another common used SES is surface enhanced infrared absorption (SEIRA) [29-32], where the enhancement is only proportional to the square of the electric field. However, SEIRA plays an important role in the field of chemical and biological sensing since it probes dipole-active vibrational modes, which provide a complementary analysis of analyte molecules. The reason why SERIA is less attractive than SERS is mainly because of the excitations of plasmonic nanostructures typically occurring in the visible and UV regions. Recently, it has been shown that a two-dimensional hexagonal close-packed (HCP) array of nanoshells with nanoscale gaps between nanoparticles provides signicant enhancements to both SERS and SERIA, effectively combining both spectroscopies on a single substrate [33]. An application of nanoshells aggregates in probing vibrational modes of adenine is realized in [34], which is shown in figure 1.3. The figure shows the transmission spectrum of neat adenine and SEIRA spectrum of adenine on nanoshells aggregates, which produces high quality spectra required for vibrational spectroscopy. The surprising discovery in this experiment is that the same substrate can provide strong electromagnetic enhancements at the same spatial locations in both the near-infrared (NIR) and the mid-infrared (MIR) regions of the spectrum.

1.3 Organization of the dissertation

In this dissertation, we focuses on the optical properties of nanocylinders composed of a

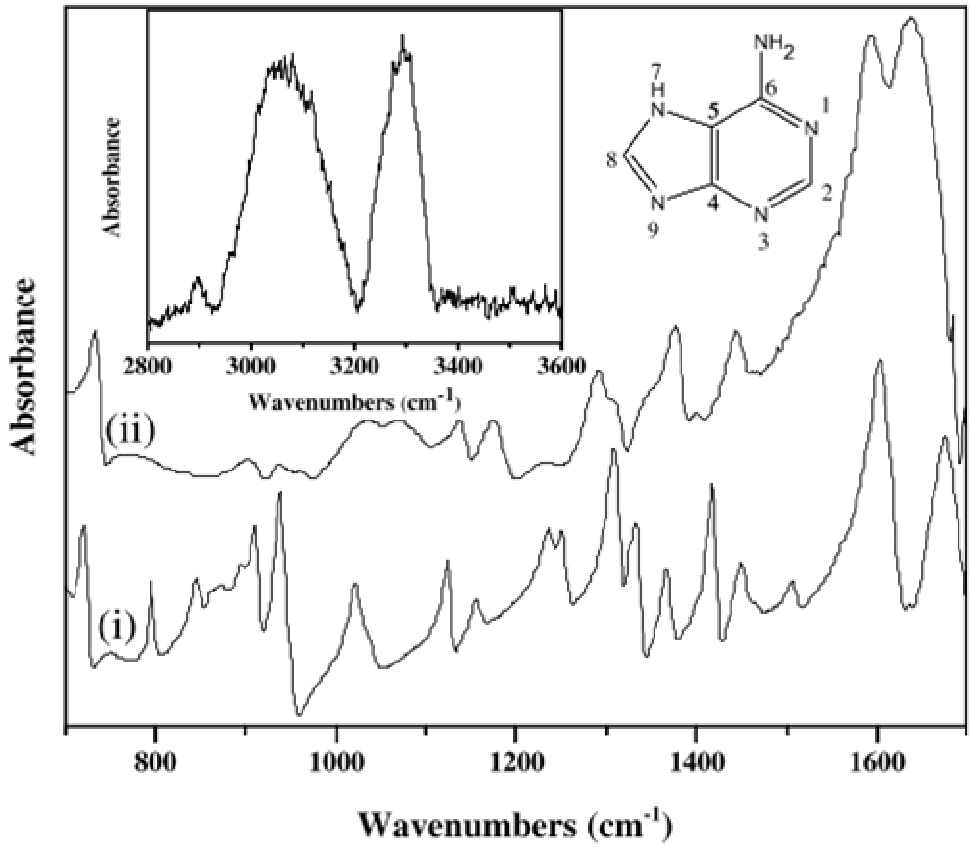

Figure 1.3 Transmission spectra of (i) of neat adenine and (ii) transmission spectrum of adenine on nanoshell aggregates. Inset shows the high wavenumber spectra for (ii). Strong molecular peaks from adenine are seen in the fingerprint region of the SERIA (ii) spectra. (J. Kundu et al. Chemical Physical Letters, **452**, 115 (2008)).

metallic shell (Au) and a dielectric core (silica), with an emphasis on the coupling between these core-shell nanocylinders. The interaction between the metallic nanostructures results in large variations of the absorption, scattering, electric field intensity and energy flow distribution. Thus, a systematic study on the coupling of localized surface plasmon in core-shell nanostructure is important.

In chapter 2, we briefly review the surface plasmon theory, localized surface plasmon theory, and the plasmon hybridization method (PH). The PH method gives an intuitive and simple way to determine the plasmon resonance frequencies of nanostructures of varying complexities.

In chapter 3, the optical properties of the core-shell nanostructures in this dissertation are studied by using finite-difference time-domain method (FDTD). We will introduce the fundamental theory of FDTD method, and then explain how to use the FDTD method to obtain the extinction, scattering, and absorption spectra. Finally, we speed up FDTD simulations by using graphics processor units.

Compared with other frequency-domain electromagnetic simulation methods, the FDTD method has the advantage that it can get full spectrum in a single simulation by propagating a short pulse, but it requires a good analytical model for the description of the dispersion of materials. In chapter 4, such an efficient dielectric function is implemented into finite difference time domain method for simulating the localized surface plasmon modes in core-shell nanostructures

Chapter 5 shows the optical properties of a dielectric-core gold–shell nanocylinder pair. The plasmonic interaction between the two dielectric-core gold-shell nanocylinders could contain an additional plasmon mode, which can’t be explained by the plasmon

hybridization method (PH method). This additional plasmon mode is resulted from the coupling of the electron at the outer surfaces of the two nanocylinders due to the lightning rod effect.

In chapter 6, the retardation effect on the plasmon modes in a silica-core gold-shell nanocylinder pair is studied. We show that for light polarized perpendicular to the axis connecting the pair, the spectrum depends sensitively on the size of nanocylinder pair. As the size increases, several retardation-induced non-dipolar plasmon modes including multipolar modes appear in the spectrum and the resonance wavelength and strength of its plasmon modes can be tuned by changing separation width between the nanocylinder pair. In chapter 7, we first introduce the fundamental principle of optical singularity and then discuss optical singularities associated with the energy flow of two closely spaced dielectric-core gold-shell nanocylinders. The optical vortices as well as saddle points can be observed in the energy flow pattern of light interacting with the core-shell nanocylinder pair in its in-phase symmetric dipolar plasmon mode. The rotating direction of the optical vortices can be tuned by varying the width of the gap between the nanocylinder pair and the value of the permittivity of the dielectric core.

In chapter 8, we discuss the optical properties of multiple dielectric-core gold-shell nanocylinder pairs. The lightning-rod effect on the LSP modes of multiple core-shell nanocylinders results in the large electric field intensity in the infrared region at long wavelength. The lightning-rod and hybridized plasmonic are two important factors that make multiple core-shell cylinders an ideal candidate for both SERS and SERIA.

Finally, the conclusions of this dissertation are drawn in Chapter 9.

References

[1] R. W. Wood, Philos. Mag. **4**, 396 (1902).

[2] U. Fano, J. Opt. Soc. Am. **31**, 213 (1941).

[3] W. Knoll, Annu. Rev. Phys. Chem. **49**, 569 (1998).

[4] M. Malmqvist, Nature **261**, 186 (1993).

[5] C. M. Braguglia, Chem. Biochem. Eng. Q. **12**, 183 (1998).

[6] F. C. Chien and S. J. Chen, Biosensors. Bioelectron. **20**, 633 (2004).

[7] P. Andrew, S. C. Kitson, and W. L. Barnes, J. Mod. Opt. **44**, 395 (1997).

[8] M. Westphalen, U. Kreibig, J. Rostalski, H. Luth, and D. Meissner, Sol. Energy Mat. Sol. Cells. **61**, 97 (2000).

[9] R. Berndt, J. K. Gimzewski, and P. Johansson, Phys. Rev. Lett. **67**, 3796 (1991).

[10] T. W. Ebbesen, H. J. Lezec , H. F. Ghaemi, T. Thio, and P. A. Wolff, Nature **391,** 667 (1998).

[11] W. Srituravanich, N. Fang, C. Sun, Q. Luo, and X. Zhang, Nano Lett. **4**, 1085 (2004).

[12] S. A. Maier and H. A. Atwater, J. Appl. Phys. **98,** 011101 (2005).

[13] B. G. Janesko and G. E. Scuseria, J. Chem. Phys. **125**, 124704 (2006).

[14] Z. E. Goude, P. T. Leung, Solid State. Comm. **143**, 416 (2007).

[15] M. Moskovits, Rev. Mod. Phys. **57**, 783 (1985).

[16] K. Kneipp, Y. Wang, H. Kneipp, I. Itzkan, R. R. Dasari, and M. S. Feld, Phys. Rev. Lett. **76**, 2444 (1996).

[17] S. Nie and S.R. Emory, Science **275**, 1102 (1997).

[18] H. Xu, E.J. Bjerneld, M. KaÈll, and L. BoÈrjesson, Phys. Rev.Lett. **83**, 4357 (1999).

[19] H. Wang, D.W. Brandl, F. Le, P. Nordlander, and N.J. Halas, Nano Lett. **6**, 827

(2006).

[20] J. Aizpurua, P. Hanarp, D.S. Sutherland, M. Kall, G.W. Bryant, and F.J. Garcia de Abajp, Phys. Rev. Lett. **90**, 057401 (2004).

[21] S.J. Oldenburg, J.B. Jackson, S.L. Wescott, and N. J. Halas, Appl. Phys. Lett. **75**, 2997 (1999).

[22] E. Prodan, C. Radloff, N.J. Halas, and P. Norlander, Science. **302**, 419 (2003).

[23] S.J. Oldenburg, R.D. Averitt, S.L. Westcott, and N.J. Halas, Chem. Phys. Lett. **288**, 243 (1998).

[24] C. Graf, A.V. Blaaderen, Langmuir **18**, 524 (2002).

[25] Y. Sun and Y. Xia, Anal. Chem. **74**, 5297 (2002).

[26] J. B. Jackson, S. L. Westcott, L.R. Hirsch, J.L. West, and N.J. Halas, Appl. Phys. Lett. **82**, 257 (2003).

[27] J.B. Jackson and N.J. Halas, Proc. Natl. Acad. Sci. **101,** 17930 (2004).

[28] Z. E. Goude and P.T. Leung, Solid State Commun. **143**, 416 (2007).

[29] M. Osawa, Top. Appl. Phys. **81**, 163 (2001).

[30] T. R. Jensen and R. P. van Duyne, Appl. Spectrosc. **54**, 371 (2000).

[31] N. Goutev and M. Futamata, Appl. Spectrosc. **57**, 506 (2003).

[32] E. A. Carrasco, F. M. C. Vallette, P. Leyton, G. Diaz, R. E. Clavijo, J. V. Garcia Ramos, N. Inostroza, C. Domingo, S. Sanchez Cortez, and R. Koch, J. Phys. Chem. A **107,** 9611 (2003).

[33] F. Le, D. W. Brandl, Y. A. Urzhumov, H. Wang, J. Kundu, N. J. Halas, J. Aizpurua , and P. Nordlander, ACS Nano **2**, 707 (2008).

[34] J. Kundu, F. Le, P. Nordlander, and N. J. Halas, Chem. Phys. Lett. **452**, 115 (2008).

Chapter 2

Theory

2.1 Fundamental properties: dispersion relation, propagation length, and excitation of surface plasmons

The electron charges on a metal boundary can perform coherent fluctuations which are called surface plasmon oscillations [1]. These charge oscillations, which can be localized perpendicular to the surface within about 1 Å (Thomas-Fermi scattering length), are accompanied by a combination between transversal and longitudinal electromagnetic fields shown in figure 2.1.

We consider a model consisting of two semi-infinite media with dielectric functions ε_m and ε_d separated by a planar interface. The interaction between the surface charges and the electromagnetic field results in the momentum of the surface plasmons (SPs) mode, which is larger than that of a photon of the same frequency in free space. This can be inferred from the SP dispersion relation [2], which is obtained by solving Maxwell's equations under the appropriate boundary conditions. The dispersion relation in figure 2.2 can be written as

$$K_{sp} = K_o \sqrt{\frac{\varepsilon_d \varepsilon_m}{\varepsilon_d + \varepsilon_m}} \ , \tag{2.1}$$

where ε_m and ε_d are the permittivity of the metal and dielectric, respectively. The K_0 is the wave-vector of free space and the K_{sp} is SP wave-vector. In order to satisfy the

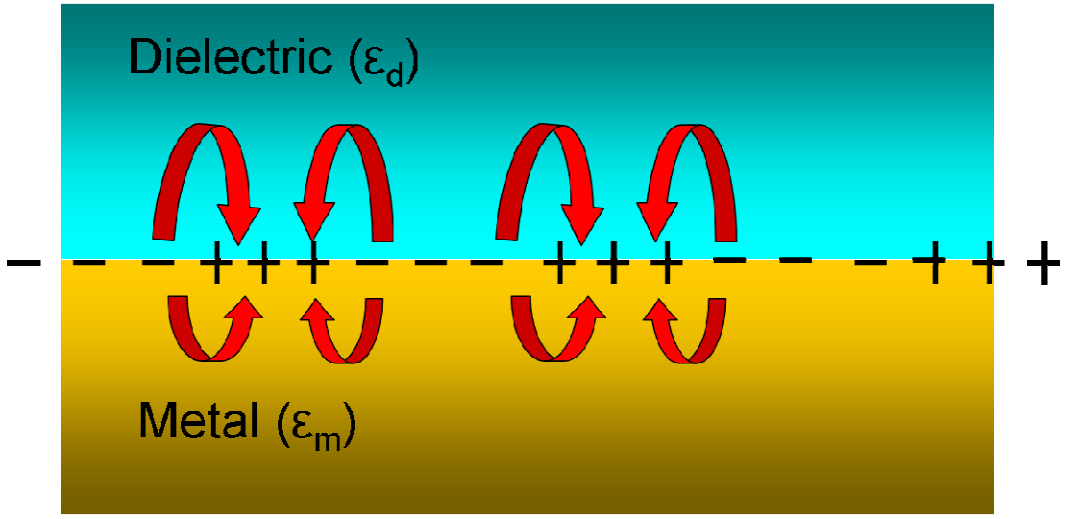

Figure 2.1 The charges and EM fields of SPs propagating along a interface between the metal and dielectric.

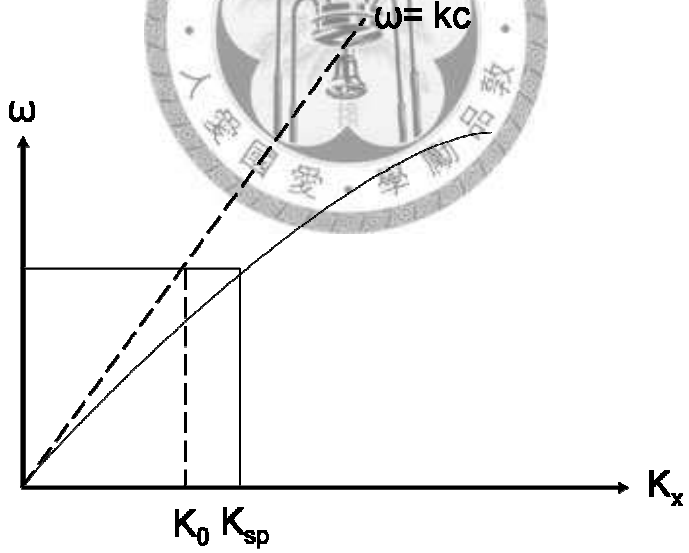

Figure 2.2 The dispersion relation of SPs.

equation (2.1), the ε_m and ε_d must have opposite signs if the SPs are to be possible at the interface between the metal and dielectric. This condition is satisfied for metal because its permittivity is both negative and complex. The dispersion relation shows that there is a momentum mismatch between light and SPs at the same frequency. Therefore, to excite SPs is needed to provide an increase in momentum. Once the SPs have been excited by incident light, the surface plasmon wave will propagate along the surface but also attenuate. The attenuation is originated from the absorption of metals. The propagation length of SP, δ_{sp}, can be obtained by evaluating the imaginary part of surface plasmon wave-vector, K_{sp}'', [3]. We should note that $K_{sp}=K_{sp}'+iK_{sp}''$.

$$\delta_{sp} = \frac{1}{2K_{sp}''} = K_o\left(\frac{\varepsilon_d + \varepsilon_m}{\varepsilon_d \varepsilon_m'}\right)^{\frac{3}{2}} \frac{(\varepsilon_m')^2}{\varepsilon_m''}, \qquad (2.2)$$

where ε_m' and ε_m'' are the real and imaginary parts of the dielectric function of the metal, that is to say, $\varepsilon_m = \varepsilon_m' + i\varepsilon_m''$. As an example, silver (Ag) is the metal with the low loss in the visible range: propagation distances are typically in the range 10-100 μm. The figure 2.3 shows that the electric field of SP modes in the perpendicular direction is evanescent, which reflects the non-radiative property of SPs.

The excitation of SPs by light is needed to overcome the momentum mismatch. There are three main techniques by which the missing momentum can be provided. The first case is to make use of a prism to increase the momentum of the incident light [4-5], which is called as ATR coupler. If light is incident inside the dielectric medium (ε>1), its momentum becomes $(\omega/c)\sqrt{\varepsilon}$ and its projection on the surface is $(\omega/c)\sqrt{\varepsilon}\sin\theta$.

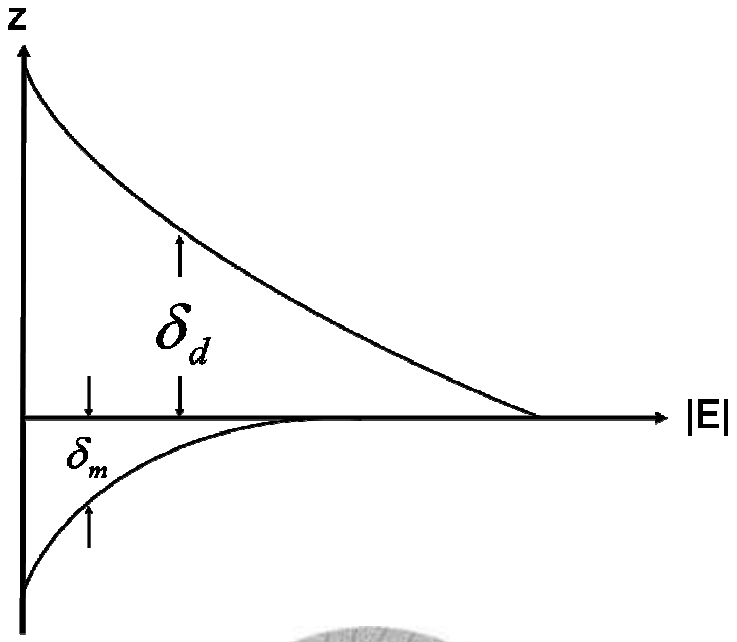

Figure 2.3 The propagation length of the SPs.

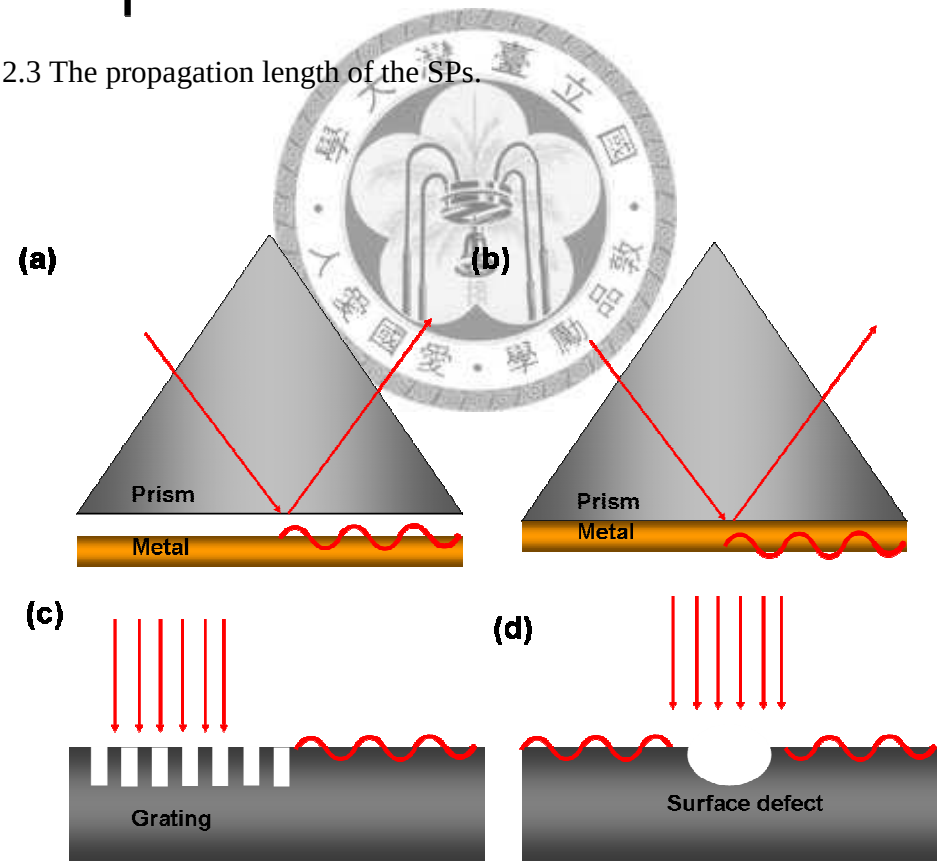

Figure 2.4 The configurations for excitation of SPs by light. (a) Otto configuration, (b) Kretschmann configuration, (c) grating, (d) surface defect.

The equation (2.1) can thus be satisfied by the device shown in figure 2.4(a)-(b). The second excitation way is to use a periodic corrugation in the metal's surface [6]. The last configuration is to use the scattering by a defect on a metallic surface, such as a subwavelength hole, which provides a convenient way to generate SPs locally.

2.2 Introduction to localized surface plasmon resonance

For the case of localized surface plasmons shown in figure 2.5, light interacts with particles that are much smaller than the incident wavelength. The LSP resonance means that the collective electrons oscillate around the particle surface with a specific frequency [8]. Similar to the surface plasmon resonance, the localized surface plasmon resonance is sensitive to changes in the local dielectric environment [9-10].

A compact treatment of localized surface plasmons is presented here. We consider a spherical nanoparticle with radius of a that is irradiated by z-polarized light of wavelength λ in the limit of $(a/\lambda) < 0.1$. In this limit, the magnitude of the electric field appears static around the nanoparticles. Therefore, we can use a quasi-static approximation to solve Maxwell's equations. The resulting solution for the EM field outside the nanoparticles is given by

$$E_{out}(x,y,z) = E_0\hat{z} - (\frac{\varepsilon_m - \varepsilon}{\varepsilon_m + 2\varepsilon})a^3 E_0(\frac{\hat{z}}{r^3} - \frac{3z}{r^5}(x\hat{x} + y\hat{y} + z\hat{z}), \quad (2.3)$$

where ε_m and ε are dielectric constant of the metal nanoparticles and surrounding medium, respectively. The equivalent dipole moment $\vec{P}$ is given by

$$\vec{\mathrm{P}} = 4\pi\varepsilon_0\varepsilon a^3(\frac{\varepsilon_m - \varepsilon}{\varepsilon_m + 2\varepsilon})\vec{E}_0 = \varepsilon_0\varepsilon\alpha\vec{E}_0, \quad (2.4)$$

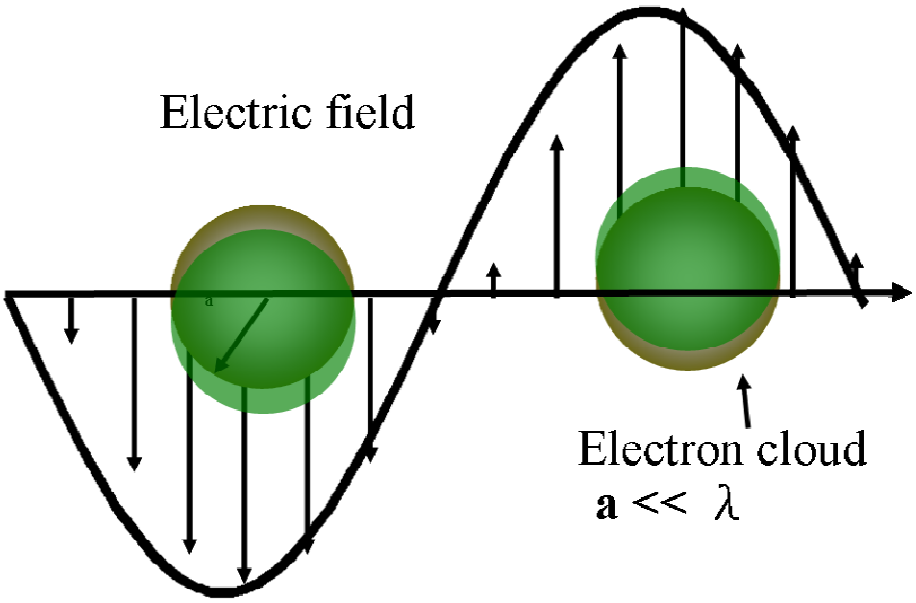

Figure 2.5 The schematic diagram of the localized surface plasmon: the diagram shows that for plasmon oscillation for a sphere, the displacement of the conduction electron charge cloud relative to the nuclei.

where α is the polarizability. From the equation (2.4), we can infer that when the dielectric constant of the metal is roughly equal to -2ε, the electromagnetic field is enhanced relative to the incident field. For example, the cases of the silver and gold are met in the visible region of the spectrum.

In the near field zone (kr<<1), we can describe the electric field and the magnetic field resulted form the dipole moment $\vec{P}$ as follows.

$$\vec{\mathrm{E}} = \frac{3\hat{\mathrm{n}}(\hat{\mathrm{n}} \cdot \vec{\mathrm{p}}) - \vec{\mathrm{p}}}{4\pi\varepsilon_0\varepsilon} \frac{1}{r^3} \tag{2.5}$$

$$\vec{\mathrm{H}} = \frac{i\omega}{4\pi}(\hat{n} \times \vec{p}) \frac{1}{r^2}, \tag{2.6}$$

where k=$2\pi/\lambda$ and $\hat{n}$ is unit vector in the direction of the observation point. On the other hand, in the limit of the radiation zone (kr>>1), the dipole fields are of the well-known spherical-wave form

$$\vec{\mathrm{H}} = \frac{ck^2}{4\pi}(\hat{n} \times \vec{p}) \frac{e^{ikr}}{r}, \tag{2.7}$$

$$\vec{\mathrm{E}} = \sqrt{\frac{\mu_0}{\varepsilon_0\varepsilon}} \vec{H} \times \hat{n}. \tag{2.8}$$

By using the analytical solutions, we can obtain the optical properties of the material whose shapes are spheres and spheroids. Although only few geometries have the analytical solution, researchers have developed several numerical methods that can help us study the optical properties of nanostructures such as discrete dipole approximation (DDA) and finite-difference time-domain method (FDTD) [11-12]. The FDTD numerical method will be introduced in chapter 3.

2.3 Plasmon hybridization method

As mentioned earlier, an analytical solution, such as Mie scattering theory, can be used to describe the optical properties of highly symmetric spherical nanostructures. Using the electromagnetic computational methods, such as DDA and FDTD, has enabled calculations of the plasmonic properties for more complicated nanoparticles and nanostructures. Although these methods can obtain the optical properties of arbitrary nanoparticles geometries directly, they give very little physical insight into the nature of plasmon resonances. Fortunately, the plasmon hybridization method developed by the P. Nordlander Group provides researchers an intuitive method for calculating the plasmonic properties of nanostructures [13-18].

Plasmon hybridization method is a mesoscale electromagnetic theory similar as how atomic orbitals interact to form molecular orbitals in electronic structure theory. In other words, the concept of the Plasmon hybridization method is that it deconstructs a nanoparticles or composite structure into more elementary shapes, and then calculates the plasmon resonance energy of the composite nanoparticles. This theory enables us to predict intuitively the plasmonic properties of complex nanostructures from the experience of molecular orbital theory.

2.3.1 Plasmons of a cavity and a solid sphere

In this section, we introduce the plasmonic properties of a nanoshell (a core-shell spherical particle consisting of a dielectric core with a thin metallic shell) based on the plasmon hybridization method. The nanoshell was realized experimentally fabricated

with a thin noble metal shell grown onto a functionalized silica core [19]. The plasmonic characteristic of the nanoshell is viewed as a hybridization of the plasmon resonances of a nanosphere and a nanocavity.

Plasmons are thought of as incompressible irrotational deformations of the conduction electron gas in metallic structures. We assume that the electrons form a liquid of uniform electron density on the ion cores. The ion cores occupy the fixed positions to form a rigid uniform background charges. The system is assumed to be charge neutral and shown in figure 2.6. We define a scalar potential η that satisfies the Laplace equation to describe the deformation of the liquid. It follows that the fluid velocity can be written as $\vec{v} = \nabla\eta$. The dynamics of the charge distribution are derived in detail in [20]. After determining the dynamics of small deformations in this fluid, we apply this formalism to calculate the plasmonic responses of a nanoshell. The dispersion of the metal is modeled by a Drude dielectric function, which is given by

$$\varepsilon(\omega) = 1 - \frac{\omega_B^2}{\omega^2}, \tag{2.9}$$

where ω_B is the bulk frequency. For brevity, the effects of the dielectric polarizibilities of metal due to the ion cores and of the medium are both ignored.

The plasmonic responses of a nanoshell can be viewed as the interaction between a solid metallic sphere and a spherical cavity inside a bulk metal. First we consider the plasmonic properties of a cavity. For a cavity of radius a inside a bulk metal, the η can be written as a sun of spherical harmonics, $\mathrm{Y}_{lm}(\Omega)$,

$$\eta(r,\Omega) = \sum_{l,m} \sqrt{\frac{a^{2l+1}}{l+1}} \dot{C}_{lm}(t) r^{-l-1} Y_{lm}(\Omega), \tag{2.10}$$

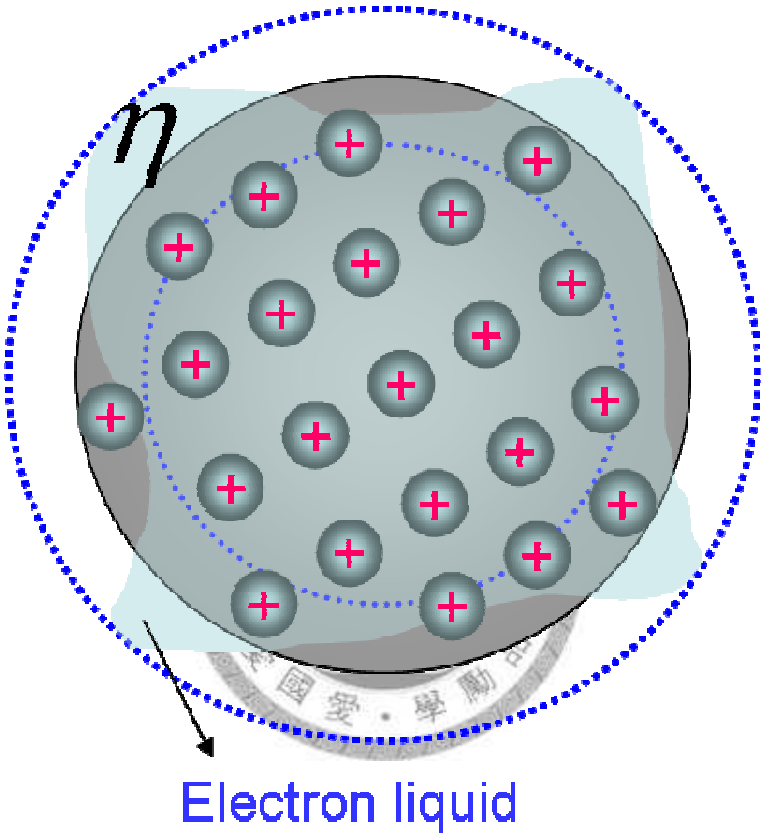

Figure 2.6 Plasmons are thought of as incompressible irrotational deformations of the conduction electrons in metallic structure. The liquid of uniform density is electrons (blue) and the rigid background charges are ion cores.

where the normalization constants, C_{lm}, were chosen for convenience, l is the angular momentum (multipolar order), and m is the azimuthal index. According to the dynamics of the charge distribution in [20], a calculation of the kinetic and electrostatic energy of the void can be evaluated. Then, the Lagrangian for the electron gas of the void inside the bulk metal can be obtained as

$$L_c = \frac{n_0 m_e}{2} \sum_{l,m} [\dot{C}_{lm}^2 - \omega_{c,l}^2 C_{lm}^2]. \tag{2.11}$$

The solution of this Lagrangian is a set of decoupled oscillators with frequency $\omega_{c,l}$, which is the plasmon frequency predicted by classical Mie scattering theory [21]

$$\omega_{c,l} = \omega_B \sqrt{\frac{l+1}{2l+1}} \tag{2.12}$$

A similar calculation can be followed for a solid metallic sphere of radius b. The η can be also written as a sun of spherical harmonics, $Y_{lm}(\Omega)$,

$$\eta(r,\Omega) = \sum_{l,m} \sqrt{\frac{1}{lb^{2l+1}}} \dot{S}_{lm}(t) r^l Y_{lm}(\Omega), \tag{2.13}$$

where S_{lm} are normalization constants for a solid sphere.

The Lagrangian for the electron gas of a solid sphere is

$$L_c = \frac{n_0 m_e}{2} \sum_{l,m} [\dot{S}_{lm}^2 - \omega_{c,l}^2 S_{lm}^2]. \tag{2.14}$$

This solution is similar to that of a void inside the bulk metal and the $\omega_{s,l}$ is equal to the plasmon frequency predicted by Mie scattering theory for a solid sphere.

$$\omega_{s,l} = \omega_B \sqrt{\frac{l}{2l+1}}. \tag{2.15}$$

2.3.2 Hybridization of nanoshells

For a metallic nanoshell with inner radius of a and outer radius of b, the general solution of Laplace equation η is given by

$$\eta(r,\Omega)=\sum_{l,m}(\sqrt{\frac{1}{lb^{2l+1}}}\dot{S}_{lm}(t)r^{l}+\sqrt{\frac{a^{2l+1}}{l+1}}\dot{C}_{lm}(t)r^{-l-1})Y_{lm}(\Omega), \tag{2.16}$$

following the similar procedure in above section, the Lagrangian of the nanoshell is

$$\mathrm{L}_{\mathrm{NS}}=(1-x^{2l+1})(L_s+L_c+n_0m_e\omega_{C,l}\omega_{S,l}x^{l+1/2}C_{lm}S_{lm}). \tag{2.17}$$

For each angular number l, this system has two fundamental frequencies

$$\omega_{l\pm}^2=\frac{\omega_B^2}{2}(1\pm\frac{1}{2l+1}\sqrt{1+4l(l+1)(\frac{a}{b})^{2l+1}}. \tag{2.18}$$

From equation (2.18), the plasmon responses of a nanoshell can be understood as the interaction of the sphere and cavity plasmons. Here we conceptually introduce the hybridization of nanoshells. The hybridization between the plasmons of a cavity and a sphere results in a splitting of a lower energy symmetric plasmon and a higher energy antisymmetric plasmon, which is shown in figure 2.7. The hybridized plamons support an antisymmetric higher energy dipolar plasmon (the charge distribution on the inner and outer surface of the shell are opposite in sign) and a symmetric lower energy dipolar plasmon. The symmetric plasmon mode has a larger dipole moment than antisymmetric mode, and therefore it is easier to be excited by incident waves. Most importantly, the thickness of the metallic shell decides the interaction distance between the sphere and cavity plasmons, which leads to the well-known tunable plasmons.

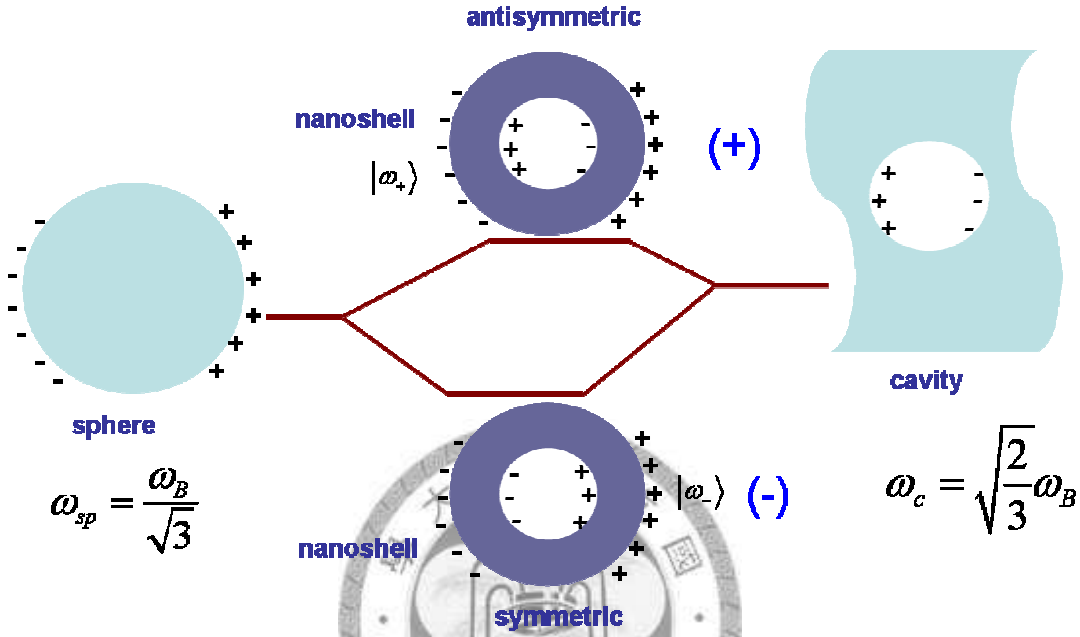

Figure 2.7 The energy diagram for the hybridization model of a nanoshell. Hybridization of a sphere and cavity plasmon to from the symmetric and anti-symmetric nanoshell plasmons.

References

[1] R. H. Ritchie, Phys Rev. **106**, 874 (1957).

[2] F. Z. Yang, J. R. Sambles, and G. W. Bradberry, Phys. Rev. B **44**, 5855 (1991).

[3] H. Raether, Surface Plasmons, (Springer, 1988).

[4] E. Kretschmann and H. Raether. Radiative. Z. Naturforsch. **23A**, 2135 (1968).

[5] A. Otto, Z. Phys. **216**, 398 (1968).

[6] R. H. Ritchie, E. T. Arakawa, J. J. Cowan, and R. N. Hamm, Phys. Rev. Lett. **21**, 1530 (1968).

[7] B. Hecht, H. Bielefeldt, L. Novotny, Y. Inouye, and D. W. Pohl, Phys. Rev. Lett. **77**, 1889 (1996).

[8] K. L. Kelly, E. Coronado, L. Zhao, and G. C. Schatz, J. Phys. Chem. B **107**, 668 (2003).

[9] M. M. Miller and A. A. Lazarides, J. Phys. Chem. B **109**, 21556 (2005).

[10] T. R. Jensen, M. L. Duval, L. Kelly, A. Lazarides, GC. Schatz, and R. P. Van Duyne, J. Phys. Chem. B **103**, 9846 (1999).

[11] B.T. Draine and P.J. Flatau, J. Opt. Soc. Am. A **11**, 1491 (1994).

[12] M. Futamata, Y. Maruyama, and M. Ishikawa, J. Phys. Chem. B **10**, 7607 (2003).

[13] P. Nordlander, C. Oubre, E. Prodan, K. Li, and M.I. Stockman, Nano Lett. **4**, 899 (2004).

[14] P. Nordlander and E. Prodan, Nano Lett. **4**, 2209 (2004).

[15] E. Prodan and P. Nordlander, J. Chem. Phys. **120**, 5444 (2004).

[16] E. Prodan, C. Radloff, N.J. Halas, P. Nordlander, Science **302**, 419 (2003).

[17] C. Radloff, N.J. Halas, Nano Lett. **4**, 1323 (2004).

[18] B. Nikoobakht and M.A. El-Sayed, Chem Mater. **15**, 1957 (2003).

[19] E. Prodan and P. Nordlander, J. Chem. Phys. **120**, 5444 (2004).

[20] G. Mie, Ann. Phys. **25**, 377 (1908).

Chapter 3

Finite-difference time-domain method

In this chapter we will introduction the finite-difference time-domain (FDTD) method. In 1966, Kane Yee [1] proposed the FDTD method, which was the Maxwell's curl equations based on the central difference method. Originally, the FDTD method was not popular due to the large computational efforts. However, the advances of the computer performance and parallel computational techniques have enabled us to do electromagnetic simulation using the FDTD method more easily. An excellent textbook on the FDTD algorithm was written by Taflove et al [2] and can be used as a self-learning textbook. Here we only briefly present the FDTD algorithm.

3.1 Fundamental Maxwell's equations

The two Maxwell's curl equations for an isotropic medium are

$$\frac{\partial \vec{H}}{\partial t} = -\frac{1}{\mu}\nabla \times \vec{E} \tag{3.1}$$

$$\frac{\partial \vec{E}}{\partial t} = \frac{1}{\varepsilon}\nabla \times \vec{H}\,. \tag{3.2}$$

First, the FDTD method solves Maxwell's equations by discretizing the equations via central differences in time and space. The most common method to discrete these equations is based on Yee's mesh [1] and computes the ***E*** and ***H*** field components at points on a grid with grid points spaced Δx, Δy, and Δz apart. The ***E*** and the ***H*** field components are then interlaced in all three spatial dimensions as shown figure 3.1.

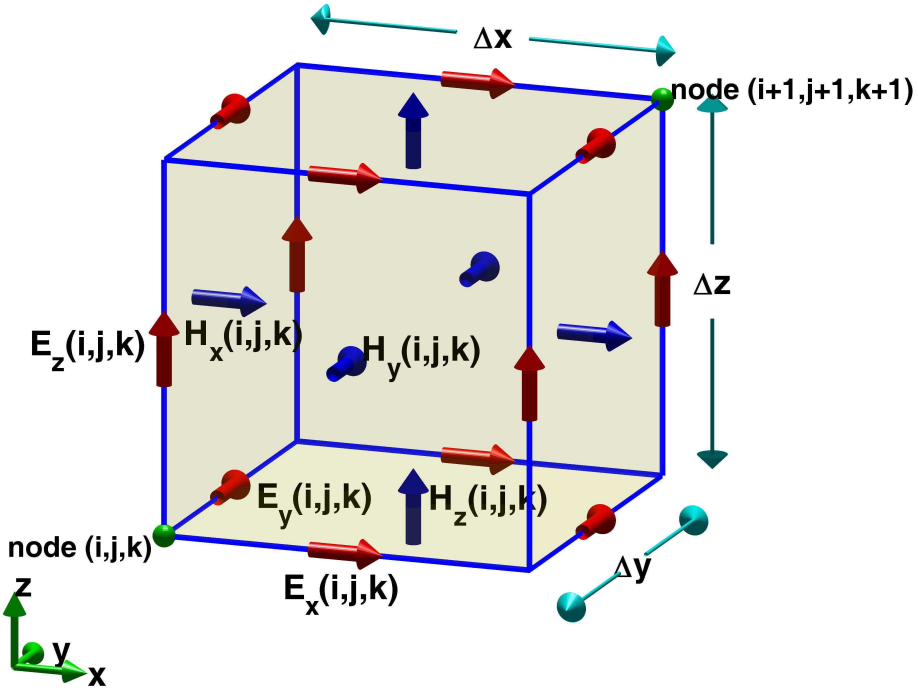

Figure 3.1 Position of the E and H fields inside a cubic unit cell of the Yee space lattice. Every E field is located ½ grid size from the origin in the direction of its polarization and every H field is offset ½ grid size in each direction except its polarization direction. (A. Z. Elsherbeni, The Finite-Difference Time-Domain Method For Electromagnetics With MATLAB Simulations, Scitech Publishing (2008))

The Yee algorithm solves for both the **E** and **H** fields in a systematic approach. After discretizing these equations (3.3)-(3.10), we can obtain six difference equations that can be computed at a given mesh point and a given time step.

$$\frac{\partial \mathrm{H}_x}{\partial t} = -\frac{1}{\mu}\left(\frac{\partial E_z}{\partial y} - \frac{\partial E_y}{\partial z}\right) \tag{3.3}$$

$$\frac{\partial \mathrm{H}_y}{\partial t} = -\frac{1}{\mu}\left(\frac{\partial E_x}{\partial z} - \frac{\partial E_z}{\partial x}\right) \tag{3.4}$$

$$\frac{\partial \mathrm{H}_z}{\partial t} = -\frac{1}{\mu}\left(\frac{\partial E_y}{\partial x} - \frac{\partial E_x}{\partial y}\right) \tag{3.5}$$

$$\frac{\partial \mathrm{E}_x}{\partial t} = \frac{1}{\varepsilon}\left(\frac{\partial H_z}{\partial y} - \frac{\partial H_y}{\partial z}\right) \tag{3.6}$$

$$\frac{\partial \mathrm{E}_y}{\partial t} = \frac{1}{\varepsilon}\left(\frac{\partial H_x}{\partial z} - \frac{\partial H_z}{\partial x}\right) \tag{3.7}$$

$$\frac{\partial \mathrm{E}_z}{\partial t} = \frac{1}{\varepsilon}\left(\frac{\partial H_y}{\partial x} - \frac{\partial H_x}{\partial y}\right) \tag{3.8}$$

Then, two major problems need to be solved: one is the numerical dispersion, and the other is the boundary conditions.

3.2 Courant-Friedrichs-Levy (CFL) condition for the FDTD method

The finite-difference time-domain method samples the electric and magnetic fields at discrete points in both time and space. The choice of the sampling must follow certain restrictions to guarantee the stability of solution, because the hyperbolic partial differential equations have a finite physical domain of dependence due to the finite traveling speeds of waves. The numerical stability of the FDTD method is determined by the Courant-Friedrichs-Levy (CFL) condition [2]**.** The CFL condition is the principle that

requires a specific bound between the time step Δt and the lattice space size. The CFL condition is given by

$$\Delta t \le \frac{1}{c\sqrt{\frac{1}{(\Delta x^2)}+\frac{1}{(\Delta y^2)}+\frac{1}{(\Delta z^2)}}} \tag{3.9}$$

where c is the speed of light in free space. If the spatial grid is chosen as a cubic, where $\Delta x = \Delta y = \Delta z$, the equation (3.9) reduces to

$$\Delta t \le \frac{\Delta x}{c\sqrt{3}} \tag{3.10}$$

Therefore, if we want to control the numerical dispersion, the maximum allowed time step is always smaller than the minimum of $(\Delta x, \Delta y, \Delta z)/c$. In the one-dimensional case where $\Delta y \to \infty$ and $\Delta z \to \infty$ in equation (3.9), the CFL condition reduces to

$$\Delta t \le \frac{\Delta x}{c}. \tag{3.11}$$

This equation implies that a wave can't be allowed to travel more than one cell size in space during one time step.

3.3 Absorbing boundary conditions

The FDTD simulation domain is finite, which is limited by the computational storage space, and this domain needs to be truncated by special boundary conditions. In this dissertation, we focus on the studies of EM scattering problems. The boundary condition should be chosen as the absorption boundary condition so that the simulated domain can be modeled as an open space. Without absorption boundary conditions, the outgoing wave would reflect at the boundary. This will result in non-physical simulation results

after a certain amount of simulation time. So far, several various types of absorption boundary conditions (ABCs) have been developed. The perfectly matched layers (PMLs) introduced by Berenger [3] has been proven to be one of the most robust absorption boundary conditions.

Since 1994, the PMLs introduced by Berenger was used as a boundary to terminate the FDTD lattices to simulate open boundary condtions, the PMLs were shown to be ineffective for absorbing evanescent wave. As a result, the PMLs must be placed sufficiently far from the simulation obstacles such that evanescent waves have sufficiently decayed [4]. Another problem for PMLs is that it suffers from late-time reflections when terminating highly elongated lattices or when simulating field with very long time signatures [4]. Therefore, the two PML formulations, which are uniaxial PML (UPML) and complex frequency-shifted PML [5](CPML), were developed to have increased ability to absorb evanescent waves, and therefore can in principle be placed closer to a simulated scattering or radiating structure than Berenger's original formulation.

In order to check our correctness of the implantation for UPML and CPML, we do a numerical experiment as similar to the case in [2]. Figure 3.2 illustrates an example: three-dimensional electromagnetic scattering by a thin PEC plate, having dimensions of 25×100 mm. The FDTD simulation domain is discretized spatially with uniform cubic cells with size of 1mm, and temporally with a time step $\Delta t = 1.9066$ ps. The excitation is provided by a z-directed electric dipole located 1mm above one of the corner of the PEC plate, which is the differentiated Gaussian pulse in time domain. In this case, we set up the observation point in the plane of the PEC plate at its opposite corner, in a direction

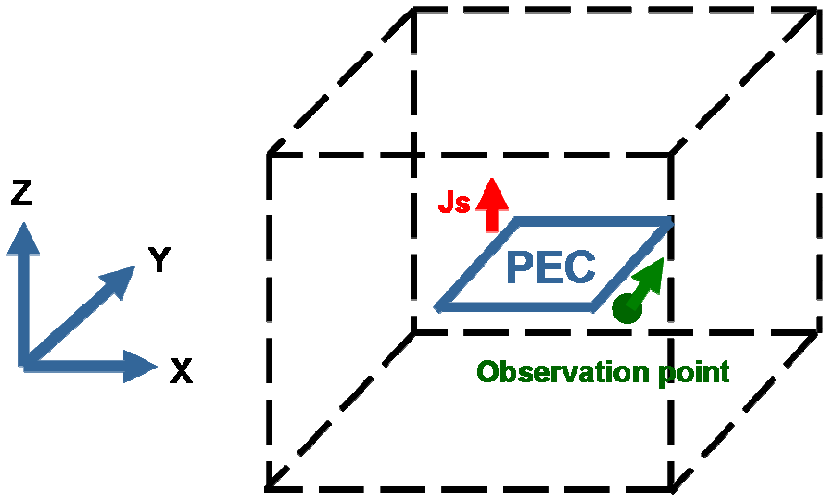

Figure 3.2 Numerical experiment: the geometry of an electric current dipole placed 1 mm above the corner of a 25×100 mm thin PEC plate. The observation point is at its opposite corner, in a direction normal to the plate edge at a distance of 1 mm.

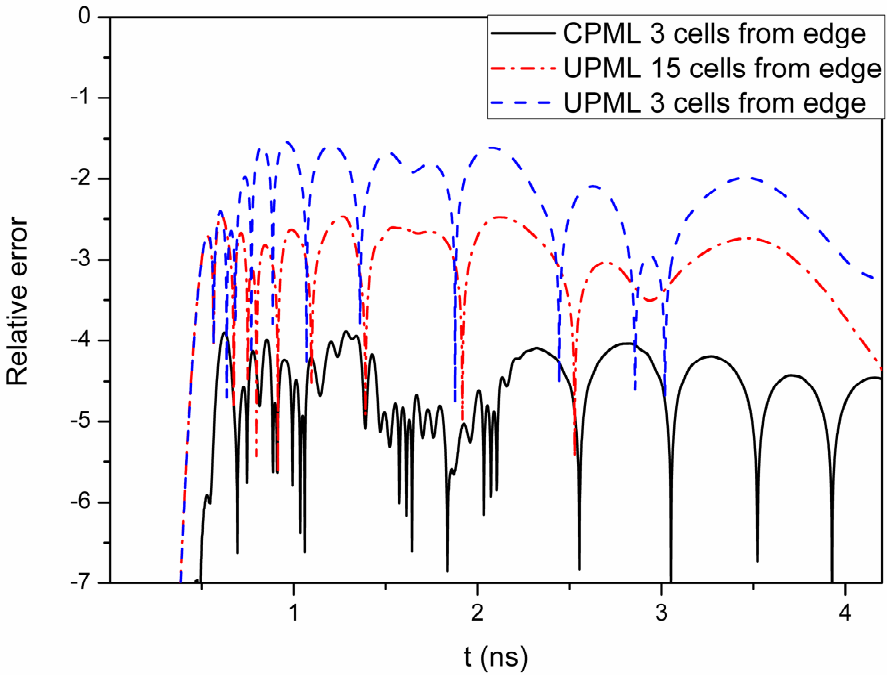

Figure 3.3 Relative errors in E_y in time domain, for 10-cells UPMLs placed 3 and 15 cells from the plate, and a 10-cell CPMLs placed 3 cells from the plate.

normal to the plate edge at a distance of 1mm form the edge. There is an evanescent wave due to the presence of the edge singularity. In order to assess the accuracy of our simulation, we compare the FDTD simulation results with the reference data that was obtained using a much larger FDTD simulation domain ($201\times276\times176$ cells). The absorption boundary is 10-cell CPML absorption boundary layers at each of outer domain boundaries. Figure 3.3 illustrates the errors in the calculated E_y at the observation point for three different cases. The first case is that UPML was placed only 3 cells from the plate in all directions. For the second case, the UPML was placed 15cells from the plate in all directions. For the third case, we use CPML placed only 3 cells from the plate to simulate the same as above cases. From figure 3.3, we can see that CPML is much better than UPML even at the case which was placed only 3 cells from the plate. Therefore, we can infer that the CPML formulation permit a much smaller space lattice to be employed.

3.4 Simulation domain

Our simulation domain, which is shown in figure 3.4, consists of three regions:

1. Region 1: Total field ;
2. Region 2: Scattered Field;
3. Region 3: Absorption boundary;

In the Region 1, the total field contains incident wave and scattering wave. The scattering wave propagates into the Region 2 and finally is absorbed by the Region 3 (CPMLs). The total field/scattered field formulation (TF/SF) is resulted from attempts to realize a plane-wave source. The TF/SF technique has enabled FDTD simulation to model a long pulse or sinusoidal incidence for arbitrary propagation directions. This formulation is based on

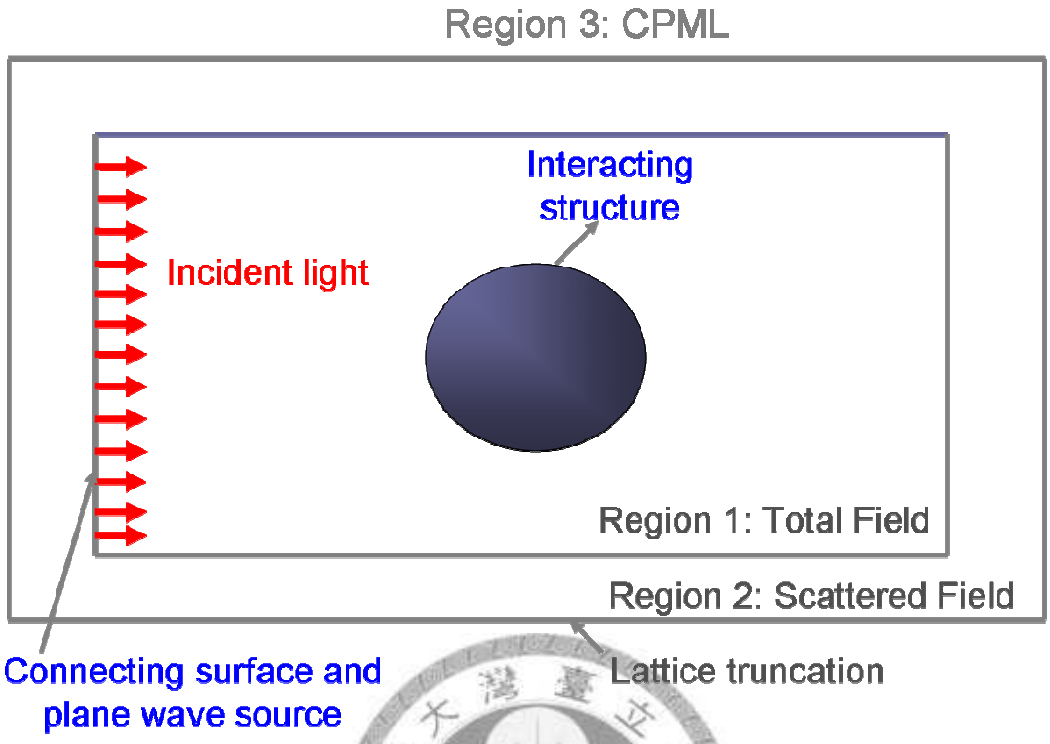

Figure 3.4 Simulation domain consists of total field, scattered field, and absorption boundary condition.

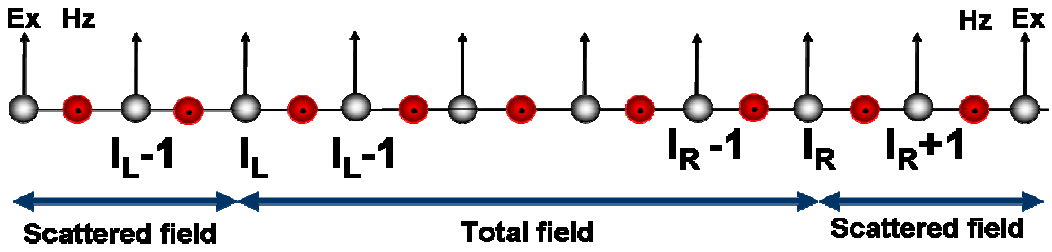

Figure 3.5 Detail of field component locations in one-dimension.

the linearity of Maxwell's equations. It assumes that the total electric $\vec{E}_{total}$ and magnetic field $\vec{H}_{total}$ can be decomposed in the following way

$$\vec{E}_{total} = \vec{E}_{inc} + \vec{E}_{scat} \tag{3.12}$$

$$\vec{H}_{total} = \vec{H}_{inc} + \vec{H}_{scat} \tag{3.13}$$

where the $\vec{E}_{inc}$ and $\vec{H}_{inc}$ are the incident fields, which are assumed to be known at all points of the space lattice at all time steps. The $\vec{E}_{sca}$ and $\vec{H}_{sca}$ are scattered fields, which are initially unknown. For one-dimensional case, which consists of E_x and H_z, is shown in figure 3.5. The TF/SF formulation provides us several advantages in the FDTD simulation. These advantages include arbitrary incident field, relatively simple program, and far-field responses. Therefore, we adopt the TF/SF formulation into our simulation domain and truncate simulation domain with CPML in order to study scattering problems.

3.5 Dispersion models

The optical properties of metals are usually frequency-dependent. Conventionally, the dispersion of metals is described by the Drude model. FDTD method is an electromagnetic field simulation tool in time domain, so its major advantage is to provide a full spectrum in a single simulation by propagating a short pulse in the time-domain. Implementation of an dielectric function into FDTD can be based on auxillary differential equation (ADE) method [6], recursive convolution method (RC) [7], or z transform method [8]. In this section, we briefly introduce the recursive convolution method to implement the Drude model into FDTD by using RC method.

The Drude model is given by

$$\varepsilon(\omega)=\varepsilon_{\infty}-\frac{\omega_D^2}{\omega^2+i\gamma\omega}, \tag{3.14}$$

where ω_D is the plasma frequency and γ is the damping coefficient. The susceptibility function is thus obtained by

$$\chi(\omega)=\varepsilon(\omega)-\varepsilon_{\infty}=-\frac{\omega_D^2}{\omega^2+i\gamma\omega}. \tag{3.15}$$

We can then fourier transform the equation 3.15 in to time domain as

$$TF[\chi(\omega)]=TF[-\frac{\omega_D^2}{\gamma}(\frac{1}{i\omega}-\frac{1}{\gamma-i\omega})]=-\frac{\omega_D^2}{\gamma}(U(t)-e^{-rt}U(t)). \tag{3.16}$$

The update equation becomes

$$\vec{\Psi}\Big|^{n}=(-\frac{\omega_D^2}{\gamma^2}(1-e^{-\gamma\Delta t})^2)\vec{E}\Big|^{n}+e^{-\gamma\Delta t}\vec{\Psi}\Big|^{n-1}, \tag{3.17}$$

where Δt is the temporal discretization used in the FDTD algorithm and n stands for the instant $t=n\Delta t$. One additional quantity χ^0 needs to be defined for the update equation of E field that will be given by equation (3.18),

$$\chi^0=-\frac{\omega_D^2}{\gamma^2}(1-e^{-\gamma\Delta t})+\frac{\omega_D^2}{\gamma}\Delta t. \tag{3.18}$$

We can finally write the update equation for E field as

$$\vec{E}\Big|^{n+1}=\frac{\varepsilon_{\infty}}{\varepsilon_{\infty}+\chi^0}\vec{E}\Big|^{n}+\frac{\Delta t}{\varepsilon_0(\varepsilon_{\infty}+\chi^0)}\nabla\times\vec{H}\Big|^{n+\frac{1}{2}}+\frac{1}{\varepsilon_{\infty}+\chi^0}\vec{\Psi}\Big|^{n}. \tag{3.19}$$

From above discussions, we can set a flow chart to demonstrate our FDTD simulation. The figure 3.6 shows a standard FDTD simulation flow chart for computing frequency domain responses. Through these processes, the frequency spectra can be obtained by the

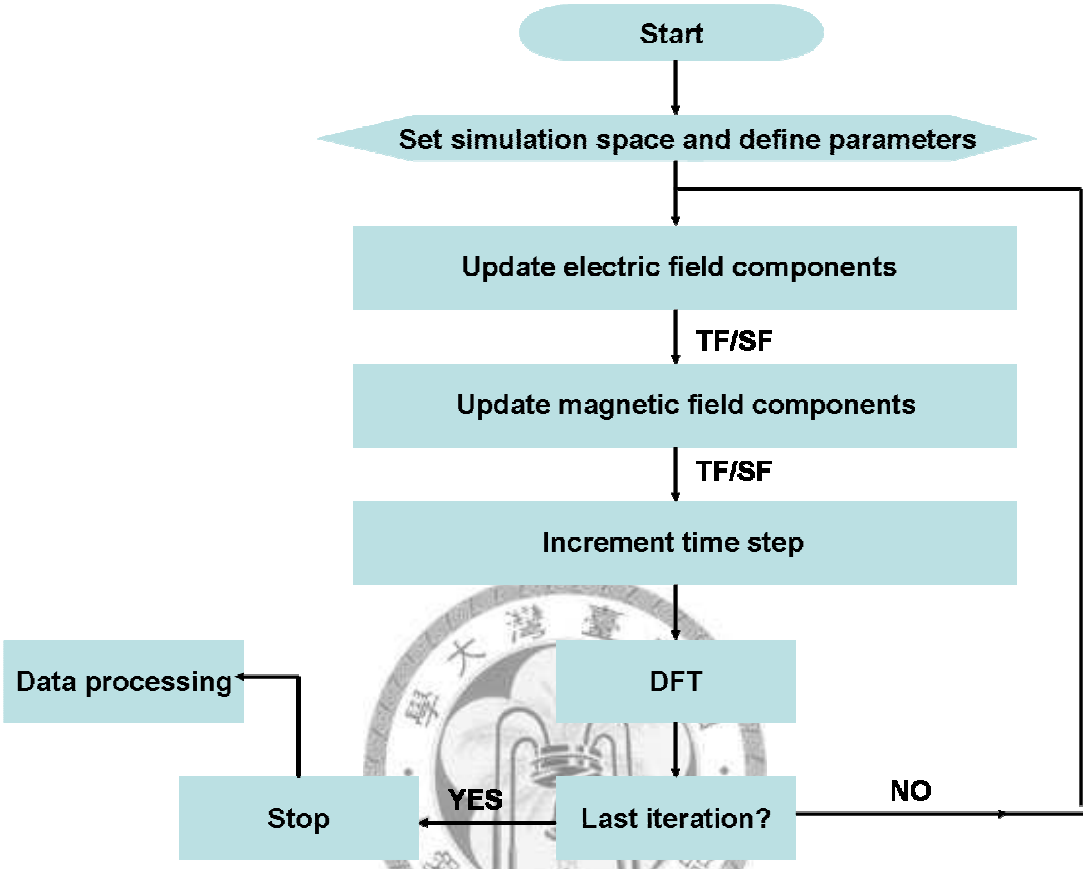

Figure 3.6 FDTD flow chart for computing frequency-domain responses.

discrete Fourier transform (DFT) if the initial excitation is a pulse in time domain. The discrete Fourier transformation means the transformation of the discrete processing data, which is obtained in time domain. We should note that the field values in the frequency domain obtained by using DFT should be normalized by the Fourier transform of the incident wave so that the frequency response of the scattering particle will return to a unit incident harmonic wave.

3.6 Cross sections

The scattering, absorption and extinction spectra can provide us with important information for the plasmonic properties of metallic nanostructures. In this section, we will show how to use FDTD method to obtain the extinction, scattering, absorption spectra of nanostructures [9]. To establish the theorem, we consider the geometry shown in figure 3.7. Since we use the TF/SF technique in our FDTD simulation domain, the incident field $(\vec{E}_i, \vec{H}_i)$ is incident on a finite scatter that lies inside the surface S. The scattered field $(\vec{E}_s, \vec{H}_s)$ propagates out from the scatter. The total field in space is defined as

$$\vec{E} = \vec{E}_i + \vec{E}_s \tag{3.18}$$

$$\vec{H} = \vec{H}_i + \vec{H}_s , \tag{3.19}$$

which is the same as in section 3.4. In general, the scattering particle can be dispersive and absorptive. The absorbed power can be obtained by integrating the inward-going component of the Poynting vector of the total fields over the surface S.

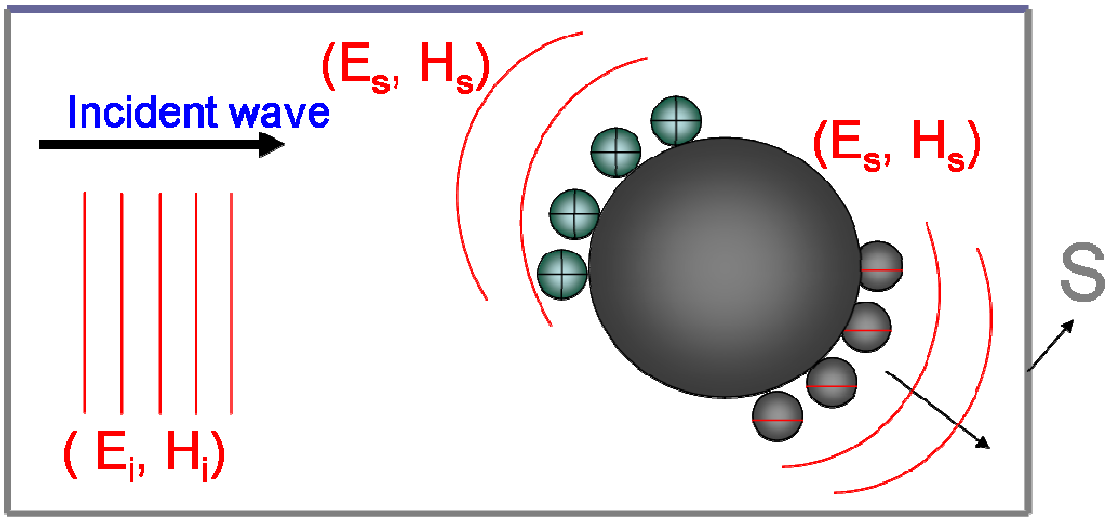

Figure 3.7 A plane wave is incident on a scatter. The scatter gives rise to a scattered wave that adds coherently to the incident wave to give a modified wave at the surface S

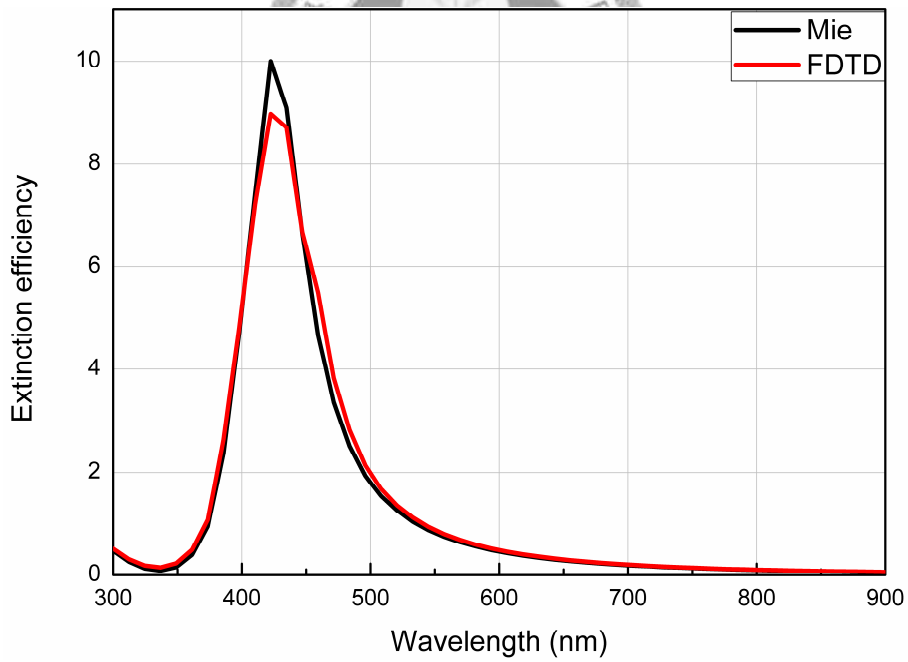

Figure 3.8 The comparison of the extionction spectra of a sphere with the radius 50nm between the three dimensional FDTD and the analytical solution in free space.

$$P_{abs} = -\frac{1}{2}\oint_S \mathrm{Re}(\vec{E}\times\vec{H}^*)\cdot\vec{n}ds \tag{3.20}$$

The scattered power can be obtained by integrating the outwardly directed component of the scattered Poynting vector over the surface S:

$$P_{sca} = \frac{1}{2}\oint_S \mathrm{Re}(\vec{E}_s\times\vec{H}_s^*)\cdot\vec{n}ds \tag{3.21}$$

The extinction power is the sum of the scattered and absorbed power:

$$P_{ext} = -\frac{1}{2}\oint_S \mathrm{Re}(\vec{E}_s\times\vec{H}_i^* + \vec{E}_i^*\times\vec{H}_s)\cdot\vec{n}ds \tag{3.22}$$

The extinction cross section is the extinction power normalized by the incident power as equation (3.23).

$$C_{ext} = \frac{-\frac{1}{2}\oint_S \mathrm{Re}(\vec{E}_s\times\vec{H}_i^* + \vec{E}_i^*\times\vec{H}_s)\cdot\vec{n}ds}{-\frac{1}{2}\oint_S \mathrm{Re}(\vec{E}_i\times\vec{H}_i^*)\cdot\vec{n}ds} = \frac{P_{ext}}{P_{inc}} \tag{3.23}$$

where the P_{inc} is the incident power. The extinction efficiency can be obtained by normalizing the cross section to cross sectional area πa_{eff}^2. The a_{eff} is the effective radius, which can be obtained from equation (3.24).

$$\frac{4}{3}\pi a_{eff}^3 = V\,. \tag{3.24}$$

The extinction efficiency is defined as follows:

$$Q_{ext} = \frac{C_{ext}}{\pi a_{eff}^2} \tag{3.25}$$

And then, we compare the extinction efficiencies obtained from the analytical solution and FDTD method in order to check this implementation. The numerical experiment

shows the extinction spectra of a metallic sphere with the radius of 50nm obtained from Mie theory [10] and 3D-FDTD. The simulation is shown in figure 3.8, which was done with the grid size of 1.25nm, courant constant of 0.5, and the total simulation time of 60000 time steps. From this validation, we know the FDTD codes we developed are accurate enough that the extinction spectrum can be matched with the result from Mie theory.

3.7 FDTD computations using a graphics accelerator

Introduction of CUDA (Compute Unified Device Architecture) by Nvidia, a leading GPU manufacturer, gave rise to a new era of graphics computing [11]. CUDA has also been used to accelerate non-graphical applications in computational biology, cryptography and electromagnetic fields simulations by an order of magnitude or more. Graphics computing is more accessible than ever and will become an important technique in computational electromagnetics in years to come [12]. In this section, The CUDA is implemented into FDTD method to accelerate our simulation efficiency.

The reason behind the discrepancy in floating-point capability between the CPU and GPU is that the GPU is specialized for compute-intensive, highly parallel computation. Therefore, more transistors are devoted to data processing rather than data caching and flow control, which is schematically illustrated by figure 3.9. More precisely, the GPU is suitable for data-parallel problems. The data-parallel problem means that the same problem is executed on many data elements in parallel. Since the finite-difference time-domain method is essentially the data-parallel problem. We can expect the

Figure 3.9 The GPU devotes more transistors to data processing. More precisely, the GPU is suitable for problems that are data-parallel. (CUDA Programming Guide Version 1.0. 2007)

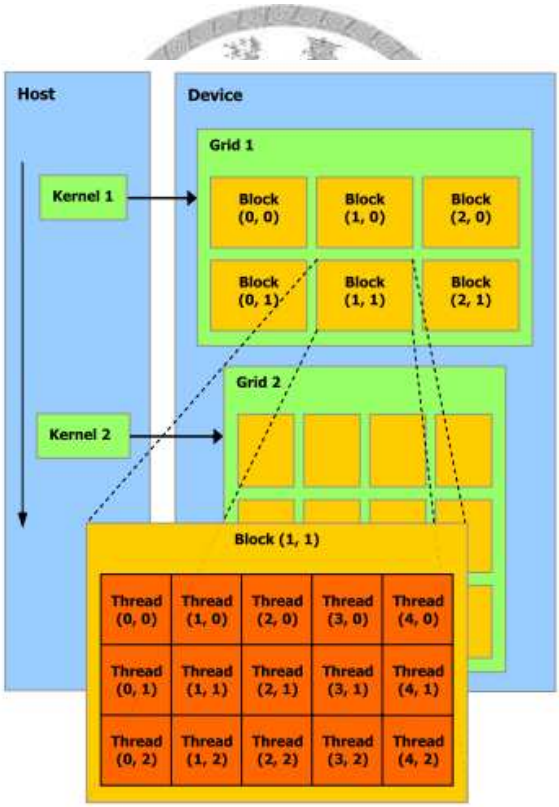

Figure 3.10 The host issues a succession of kernel invocations to the device. Each kernel is executed as a batch of threads organized as a grid of thread blocks. (CUDA Programming Guide Version 1.0. 2007)

implementation of GPU-CUDA is suitable for the acceleration of the FDTD method.

3.7.1 CUDA programming model

In this section, we introduce the main concepts that make up the CUDA programming model by explaining how they are exposed in C. C for CUDA extends C by allowing the programmer to define C functions, which are called kernels. When we called the kernels, they will be executed by CUDA threads. On current GPUs, a thread block may containup to 512 threads. A kernel should be executed by the same shaped thread blocks, so that the total number of threads is equal to the number of threads per block times the number of blocks. Therefore, these blocks are organized into 1D or 2D grid as shown in figure 3.10.

In order to optimize our GPU-Based FDTD efficiency, we should consider not only the threads but also the memory hierarchy. The issue on the efficient memory usage can be found in [11]. Each thread has a private local memory. Each block has shared memory spaces, which are available to all threads of the block. Finally, all threads have access to the same global memory. The shared memory is expected to be much faster than global memory. Any opportunity to replace global memory by shared memory should be an important issue.

For the optimization of reading data, there are two read-only memory spaces accessible by all threads: the constant and texture memory spaces. There is a total of 64 KB constant memory on a device. The constant memory space is cached but only for the threads of a half warp. Reading from the constant cache is as fast as reading from a register as long as all threads read the same address. In addition, the read-only texture memory space is also cached. The texture cache is optimized for 2D spatial locality, so threads of the same

warp that read texture addresses that are close together will achieve best performance. Using these two memory spaces can make the executed speed much faster. After considering these techniques, our 2-D FDTD update equation becomes as the following CUDA code:

```
0 texture<float, 2, cudaReadModeElementType> texref2dcaey;
1 texture<float, 2, cudaReadModeElementType> texref2dcbey;
2 texture<float, 2, cudaReadModeElementType> texref2dccey;
3 #define texcaey(i,j) tex2D(texref2dcaey,i,j)
4 #define texcbey(i,j) tex2D(texref2dcbey,i,j)
5 #define texccey(i,j) tex2D(texref2dccey,i,j)
6  __global__ void tex2d_update_Ey_field(float* hEy,float* hHz,float* hphidruey1,int nx, int ny){
7
8         const     int i=blockIdx.x*blockDim.x+threadIdx.x;
9         const     int j=blockIdx.y*blockDim.y+threadIdx.y;
10
11        const     int in=blockIdx.x*blockDim.x+threadIdx.x-1;
12
13                  if(i<nx-1&&j<ny-1&&i>0){
14
15
16        hEy(i,j)=texcaey(i,j)*hEy(i,j)+texcbey(i,j)*(hHz(i,j)+hHz(in,j))+texccey(i,j)*hphidruey1(i,j);
17                  }
18
19 }
```

The simple function has the information for the update equations and the optimization of reading data. First, we need to declare the texture reference (line 0 to 2). Then these

definitions are used to simply the matrix index. The texcaey(i,j), texcbey(i,j), and texccey(i,j) are the real-value matrices whose values are constant throughout the simulation. Thus we read those matrices by using texture memory.

3.7.2 Host and Device

CUDA programming model assumes that the CUDA threads execute on a physically separate device that operates as a coprocessor to the host running the C programming. In other words, the device is GPU and the host is CPU. The initial values are initialized at the host and then transferred to GPU. The part of the FDTD that costs most of computation time should be executed at the device to obtain the maximum optimization. Therefore, the FDTD flow chart should be changed into figure 3.11. In order to compare the efficiency between the CPU-FDTD and GPU-FDTD, we simulate a single metallic nanocylinder with radius of 20nm by using two-dimensional finite-difference time-domain method. The test machines are the Nvidia C870 and the 3.3GHz Intel Xeon, Quad-core, respectively. The numerical experiment was done with two different numbers of grids. In the first time, the experiment was done with the gird number 2048×2048, and in the other time, it was done with the grid numbers 3072×3072. The comparison can be found in Table 3.1. The efficiency is defined as the simulation time cost by CPU divided by the simulation time cost by GPU. Compared with CPU-FDTD, the GPU-FDTD is 25 times faster. The results show that the GPU-FDTD enables us to do electromagnetic simulation more efficiently.

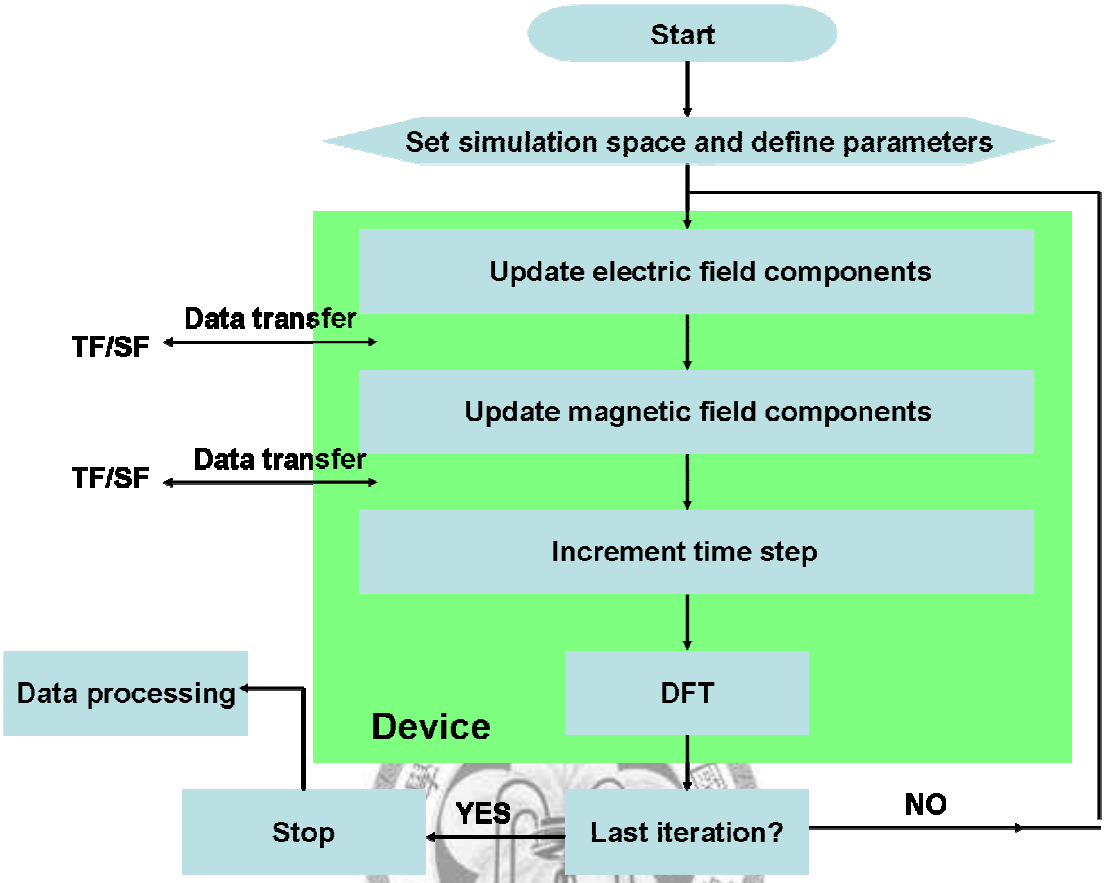

Figure 3.11 The host dominates the initial parameters and field value records, and the device dominates the FDTD update equation, which costs most of simulation time. The green region is the part of FDTD by using the device.

Grid number		GPU-FDTD	CPU-FDTD
2048×2048	**efficiency**	25.1279	1
3072×3072	**efficiency**	26.0201	1

Table 3.1 The comparison of the efficiency between GPU-FDTD and CPU-FDTD. The speed-up of GPU-Based FDTD is about 25 times.

References

[1] K. Yee, IEEE Trans. Antennas Propag. **14**, 302 (1966).

[2] A. Taflove and S. C. Hagness, Computational Electrodynamics: The Finite Difference Time Domain Method (Artech House, London, 2000).

[3] J. P. Berenger, J. Comp. Physiol. **127**, 363 (1996).

[4] J. P. Berenger, IEEE Trans. Antennas Propagat. **47**, 1497 (1999).

[5] J. Roden and S. Gedney, Microwave Opt. Technol. Lett **27**, 334 (2000).

[6] T. Kashiwa and I. Fukai, Microwave Opt. Technol. Lett. **3**, 203 (1990).

[7] R. J. Luebbers, F. P. Hunsberger, K. S. Kunz, R. B. Standler, and M. Schneider, IEEE Trans. Electromagn. Compat. **32**, 222 (1990).

[8] D. M. Sullivan, IEEE Trans. Antennas Propag. **40**, 1223 (1992).

[9] S. K. Gray and T. Kupka, Phys. Rev. B **68**, 045415 (2003).

[10] G.Mie, Ann. Phys. **25**, 377 (1908).

[11] CUDA Programming Guide Version 1.0. 2007.

[12] S. E. Krakiwsky, L. E. Turner, and M. M. Okoniewski, in IEEE MTT-S International Microwave Symposium Digest **2**, 1033 (2004).

[13]M. J. Inman, A. Z. Elsherbeni, J. G. Maloney, and B. N. Baker, in IEEE Trans. Antennas Propag., 5255 (2007).

Chapter 4

Implementation of an efficient dielectric function into finite difference time domain method for simulating the coupling between localized surface plasmon of nanostructures

4.1 The advantage of the FDTD method: getting full spectrum in a single simulation

Comparing with other frequency-domain electromagnetic simulation methods which can obtain solutions at a definite frequency, the FDTD method has the advantage that it can get full spectrum in a single simulation by propagating a short pulse, but it requires a good analytical model for the description of the dispersion of materials. For the analytical model, the four-Lorentzian (L4) model proposed by Hao and Norlander showed a better fit than other frequently-used dielectric functions for gold and silver in the spectral range between 180nm and 2000nm [1]. The other analytical models, known as the Drude critical point model which includes one Drude terms and two critical point terms shows a better fitting quality than the L4 model in the near UV and visible region [2], but in the wide spectral range between 180nm and 2000nm the Drude critical point model is still less accurate than the L4 model overall.

In this chapter, an improved dielectric function model is developed, together with a comparison of the improved model and L4 model with experimental data [3] and the fitting parameters for gold and silver are presented. The results show that the model we present is better than the L4 model for gold and silver, both in accuracy and

computational efforts in the spectral range between 180nm and 2000nm. We use it to simulate the interaction between a pair of core-shell nanocylinders for polarization direction parallel to the axis of the pair. The results show that the plasmon resonance wavelength red-shifted with decreasing gap width.

4.2 Dispersion models

4.2.1 The L4 model

An analytical model including the four Lorentzian terms (L4) has been recently presented for the description of the dispersion of gold and silver in the wide wavelength range between 180nm and 2000nm. The model can be expressed as

$$\varepsilon(\omega) = \varepsilon_{\infty} + \frac{\sigma / \varepsilon_0}{i\omega} + \sum_{p=1}^{4} \frac{C_p}{\omega^2 + A_p i\omega + B_p} \tag{4.1}$$

We can implement the L4 model by recursive convolution (RC) method or auxiliary differential equation (ADE) method which can be derived from [4] into FDTD method with the fitting parameters given in [1]. Although this model is suitable for simulating highly tunable metallic nanostructures such as nanoshell and nano ring, we should note that having more Lorentzian terms increases the accuracy of the fitting quality, it also increases the memory needed in the FDTD simulation. In addition, the L4 model is not accurate enough to describe the permittivity of Ag due to large variations in the imaginary part of the permittivity as compared with the experimental data. For the above reasons, it is desirable to have an analytical model that can best describe the dispersion of materials accurately and cost the least amount of memory at the same time.

4.2.2 The CP3 model

In order to obtain such an analytical model, we try to use critical point terms to replace the Lorentzian terms of L4 model because the critical point term gives better description of the interband transition of noble metals. The result shows that we can get better fitting quality than the L4 model for gold and silver by just three critical point terms. The three critical point pole pairs (CP3) model can be expressed as

$$\varepsilon(\omega) = \varepsilon_\infty + \frac{\sigma/\varepsilon_0}{i\omega} + \sum_{p=1}^{3}\left(\frac{A_p\Omega_p e^{i\phi_p}}{\Omega_p - \omega - i\Gamma_p} + \frac{A_p\Omega_p e^{-i\phi_p}}{\Omega_p + \omega + i\Gamma_p}\right) \tag{4.2}$$

Since a critical point term in the time domain was proved to be close to the form of the Fourier transform of a Lorentzian term by A. Vial [5] as shown in equation (4.2). We can implement the critical point term of the CP3 model into the FDTD method similar to the Lorentizn term by the RC method or ADE method. In order for readers to implement it conveniently, we offer the numerical implementation of the CP3 model with the RC method in the appendix.

$$TF[G_p(\omega)] = 2A_p\Omega_p e^{-\Gamma_p}\sin(\Omega_p t - \phi_p) \tag{4.3}$$

4.2.3 Comparison of the models

In this section we compare the fitting quality of L4 model and CP3 model with tabulated values of gold and silver in [3]. The parameters of L4 model for gold and silver are taken from [1], and the parameters of CP3 model for gold and silver are displayed in Table 4.1. The comparisons show that we can use the CP3 model to simulate the plasmonic properties of highly tunable metallic nanostructures in a wide wavelength range between 180nm and 2000nm more precisely and easier (less memory and computing time) than

CP3		
	Au	**Ag**
ε_∞	1.1156	1.4783
σ	4.24×10^{16}	1.32863×10^{16}
A_1	0.5548	1.077
$\phi_1(rad)$	2.8463	-0.9621
$\Omega_1(rad\,s^{-1})$	4.506×10^{16}	6.617×10^{15}
$\Gamma_1(rad\,s^{-1})$	5.09×10^{16}	1.7415×10^{15}
A_2	679.7606	5377.4512
$\phi_2(rad)$	-0.0998	-0.0092
$\Omega_2(rad\,s^{-1})$	3.4587×10^{14}	1.3545×10^{14}
$\Gamma_2(rad\,s^{-1})$	3.064×10^{13}	6.56505×10^{12}
A_3	3.5244	2.6077
$\phi_3(rad)$	4.6586	-2.8539
$\Omega_3(rad\,s^{-1})$	3.5832×10^{15}	8.1007×10^{14}
$\Gamma_3(rad\,s^{-1})$	1.68784×10^{15}	8.7193×10^{12}
Φ	15.3895	18.1032
L4		
	Au	**Ag**
Φ	33.1722	191.489

Table 4.1 The optimized parameters for the CP3 model for gold and silver in the spectrum between 180 nm and 2000 nm and the values of the fitness function of the CP3 model and L4 model.

the L4 model. In figure 4.1, we compare the L4 and CP3 model with experimental data for gold. For the real part of the permittivity of gold, the L4 and CP3 model are both close to the–experimental data, with a better fit for CP3 model near 1900nm. For the imaginary part of permittivity of gold, the L4 and CP3 model give a similar description of the interband transitions of gold. Because of the plasmon resonance wavelength is determined by the real part of the permittivity, it is more important to get a better fitting with the real part of the permittivity than the imaginary part of the permittivity in the spectrum. In figure 4.2, we compare the L4 and CP3 model with experimental data for silver. For the real part of the permittivity of silver, the CP3 model gives a much better fit with experimental data for wavelengths between 1200nm and 2000nm, and the L4 model starts to deviate slightly from the experimental data at 1200nm. For the imaginary part of the permittivity of silver, the CP3 model behaves obviously better than the L4 model in the spectrum. The negative imaginary part of L4 model in some parts of the spectrum will result in an artificially near field enhancement in plane wave studies. Although the CP3 model is not very close to the experimental data, the values of the CP3 model are at least positive unlike the L4 model for silver.

In order to compare the two models more clearly, we define the fitness function Φ to compute the errors quantitatively for the wavelengths between 180nm and 2000nm

$$\Phi = \sum_{\omega} \left| \varepsilon_{tab}(\omega) - \varepsilon_{\text{model}}(\omega) \right|^2 \tag{4.4}$$

where $\varepsilon_{tab}(\omega)$ is the values tabulated from [3], and the sum is over the tabulated frequency values in [3]. The values of the fitness function of L4 and CP3 model are displayed in Table.4.1. For gold, the value of the fitness function of CP3 is smaller than

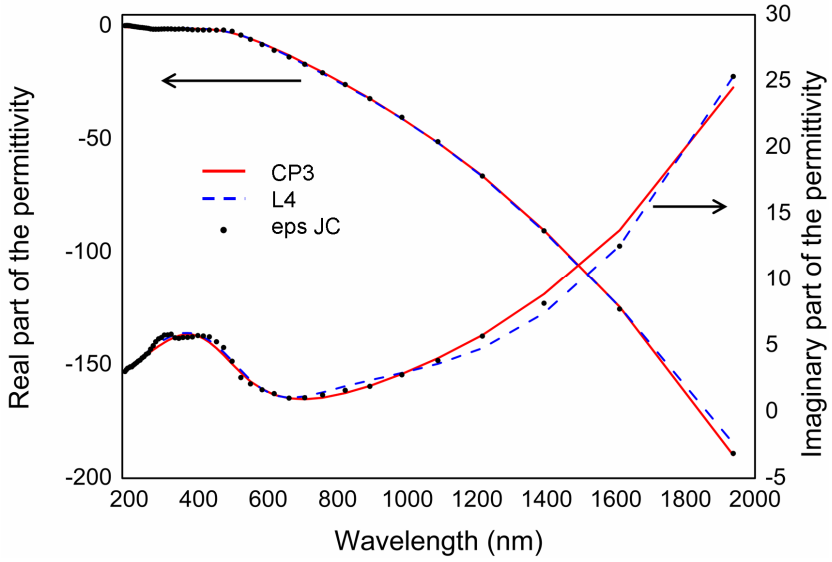

Figure 4.1 (a) The permittivity of gold obtained from tabulated data (dots) [3], the CP3 model (dash blue lines), and the L4 model (red line).

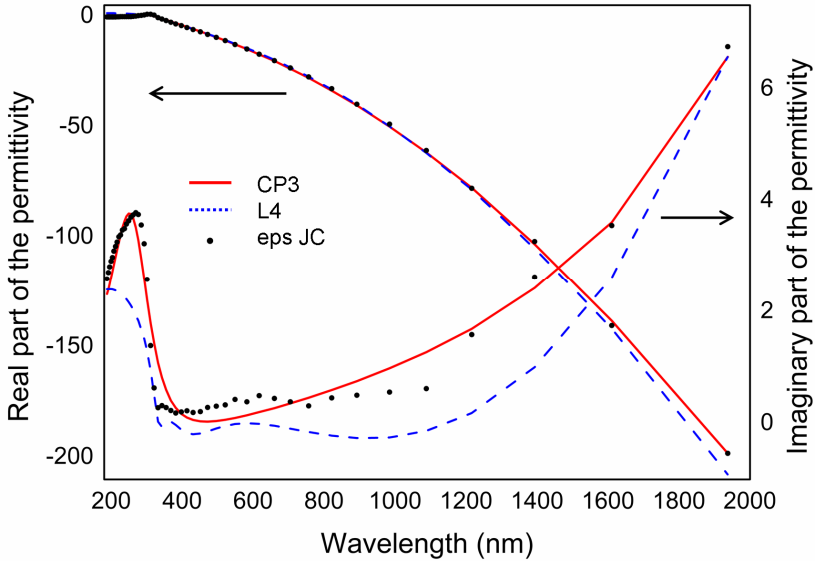

Figure 4.2 (a) The permittivity of silver obtained from tabulated data (dots) [3], the CP3 model (dash blue lines), and the L4 model (red line).

half of the L4 model. For silver, the value of the fitness function of CP3 is less than that of the L4 model by an order of magnitude. From the above comparisons, we can judge that the CP3 model plus the fitting parameters displayed in Table.4.1 can be used in

4.3 Results and discussions

The FDTD calculations were done using a mesh size 0.4 nm, a time step of 6.6697e-19s, and a Courant number of 0.5. The CP3 model was then incorporated into 2D-FDTD method to simulate the optical response of a pair of silica-core gold-shell nanocylinders with variable gap width for polarization direction parallel to the axis of the pair. In the simulation, the outer and inner diameter of the core-shell nanocylinder is set at 80 nm and 50 nm, respectively, the permittivity of the silica is 2.1, and the permittivity of gold material is described by the CP3 model with the parameters given in Table 4.1.

In the simulation, the propagating direction of the short EM pulse is perpendicular to the axis of the pair and electric field of the EM wave is parallel to the axis of the pair. In order to perform spectral analysis, we keep running the discrete Fourier transforms along the total field and scattering field boundary (TFSF boundary). In figure 4.3, the simulation results show that due to the coupling between the core-shell nanocylinders when the gap width between the nanocylinders decreases, the resonance wavelength of the localized surface plasmon mode shifted to lower energy and the extinction efficiency increases.

When the gap width decreases from 180nm to 6nm, the plasmon resonance wavelength shifted from 590 nm to 632 nm. These plasmon resonances are resulted from the dipole-dipole interaction between the nanocylinders and the dipole mode of the core-shell

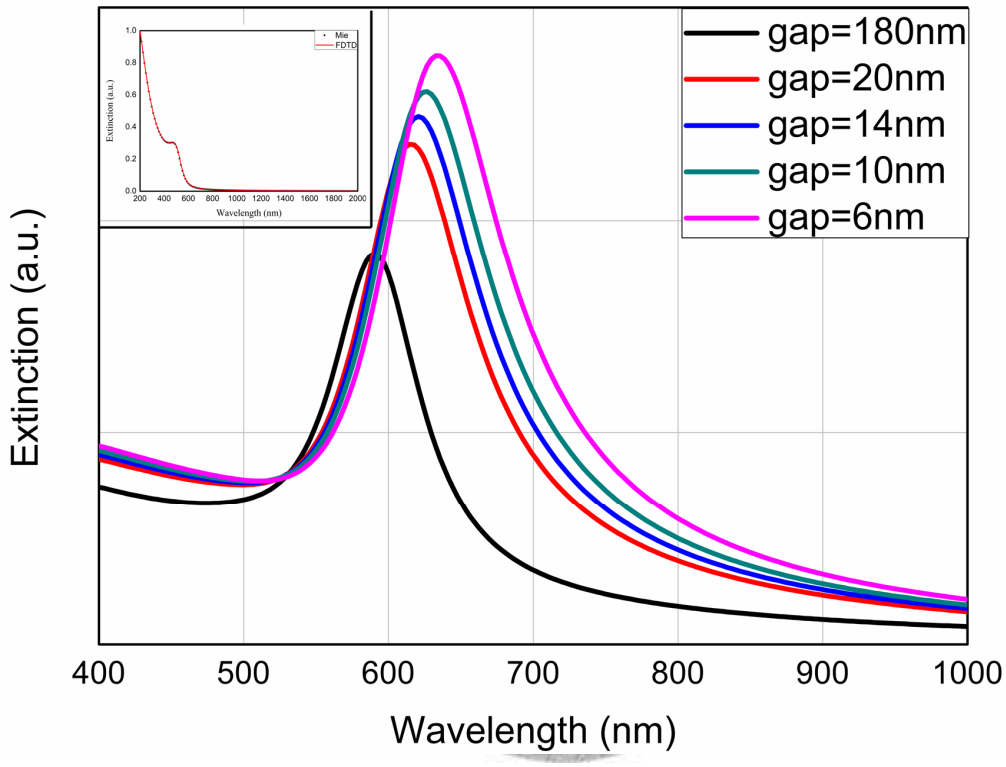

Figure 4.3 The dependence of the extinction spectrum of a pair of core–shell nanocylinders on the gap width between the nanocylinders. The plasmon resonance wavelength shifts from 590 nm to 632 nm when the gap width decreases from 180 nm to 6 nm. Inset: The extinction spectrum of a gold nanocylinder with a diameter of 40 nm obtained from the Mie theory (dots) and FDTD method (red lines) with the CP3 model.

nanocylinder oscillates in-phase with another (the dipole mode is symmetric binding mode whose electrons at outer surface is aligned symmetrically with the electrons at inner surface [7]). We don't see the out-of-phase dipole-dipole interaction mode because the mode which doesn't have dipole moment can't be induced by external light. Because the phase retardation effect needn't be considered in such a size smaller than 1/4 wavelength, there are no higher multipole modes in the extinction spectrum. In addition to changing the gap width, the ratio of the outer radius to inner radius of the core-shell nanocylinder, or the refractive index of the core can also be used to tune the resonance frequency.

4.4 Summary

An efficient dielectric function called CP3 model was developed and it was compared with the L4 model in the wavelength range between 180nm and 2000nm. The results show that the CP3 model can be used in studying the optical properties of gold and silver more efficiently and accurately than the L4 model. The CP3 model was then incorporated into FDTD to study the coupling of the silica-core gold-shell nanocylinder pair. The simulation result shows that for polarization direction parallel to the axis of the pair, the plasmon wavelength in the plasmon extinction maximum red-shifted from 590nm to 632nm when the edge-to-edge gap decreases from 180nm to 6nm.

References

[1] F. Hao and P. Nordlander, Chem. Phys. Lett. **446**, 115 (2007).

[2] A. Vial and T. Laroche, Appl. Phys. B **93**, 139 (2008).

[3] P. Johnson and R. Christy, Phys. Rev. B **6,** 4370 (1972).

[4] A. Taflove and S. C. Hagness, Computational Electrodynamics: The Finite-Difference Time-Domain Method, 3rd ed, (Artech House, Boston, 2005).

[5] A. Vial, J. Opt. A: Pure Appl. Opt. **9**, 745 (2007).

[6] C. F. Bohren and D. R. Huffman, Absorption and Scattering of Light by Small Particles (John Wiley & Sons Inc., New York, 1998)

[7] E. Prodan, C. Radloff, N. J. Halas, and P. Norlander, Science **302,** 419 (2003).

Chapter 5

The lightning-rod mode in a core-shell nanocylinder dimer

5.1 Introduction: a new plasmon mode associated with the core-shell nanocylinder pair

The plasmon modes of a solid nanostructure are characterized by the surface charge distributions on the surface of the solid nanostructure [1]. For the core-shell structures [2-4], the interaction between the surface charge distributions at the inner and outer surfaces of the core-shell structure splits the plasmon resonance modes into two different alignment plasmon modes and results in the large variation of the plasmon resonance wavelength for the core-shell nanostructure. The plasmon resonance wavelength of the core-shell structure can be tuned by the permittivity of the dielectric core and the ratio of the outer radius to inner radius [5]. By the same token, when two plasmon-resonant core-shell nanoparticles are brought together, the plasmon modes in the individual nanocylinders can interact with each other, leading to new resonance modes for the coupled system. These plasmon modes have been investigated in detail in [3, 6-9].

In this chapter, a new plasmon mode associated with the core-shell nanocylinder pair is reported. We found that a resonance mode resulted solely from the coupling of the electrons at the outer surfaces of the two core-shell nanocylinders can be observed when the size of the nanocylinder is large enough. The size-dependence and permittivity-dependence of this special plasmon mode indicate that this plasmon mode shows up as a

result of the screening effect of the metallic shell and reflection at the metal/dielectric boundary. Such a phenomenon is essentially caused by the lightning-rod effect, which occurs when metals approach to the perfect conductors in low frequency and the electric field concentrates in the gap of the nanocylinder dimer. A related discussion of plasmonic systems associated with the lightning-rod effect can be found in [15].

5.2 Calculation methods

The FDTD calculations were done accurately using a mesh size of 0.25 nm, a time step of 4.16666e-19s, and a Courant number of 0.5. The program codes have been checked with the analytical theory [10]. The optical response of gold is modeled using the three critical point pole pairs (CP3) model [11] which provides a good fit to tabulated experimental data [12]. The geometrical arrangement of the nanocylinder pair and the incident wave is shown in figure 5.1, the propagating direction of the incident wave is perpendicular to the axis that connects the nanocylinder pair, and the electric field of the incident wave is parallel to this axis.

5.3 Results and Discussions

We first investigate the extinction spectra of a silica-core gold-shell nanocylinder pair, for different sizes. The ratio of outer radius to inner radius is fixed at 6:5, the ratio of outer radius to separation distance between two nanocylinders is fixed at 5:1, and the outer radius is varied from 15nm to 135nm with an interval of 30nm. The extinction spectra as a function of the size of the nanocylinder pair, and the charge distribution of the plasmon modes in the nanocylinders are shown in figure 5.2. For outer radius of

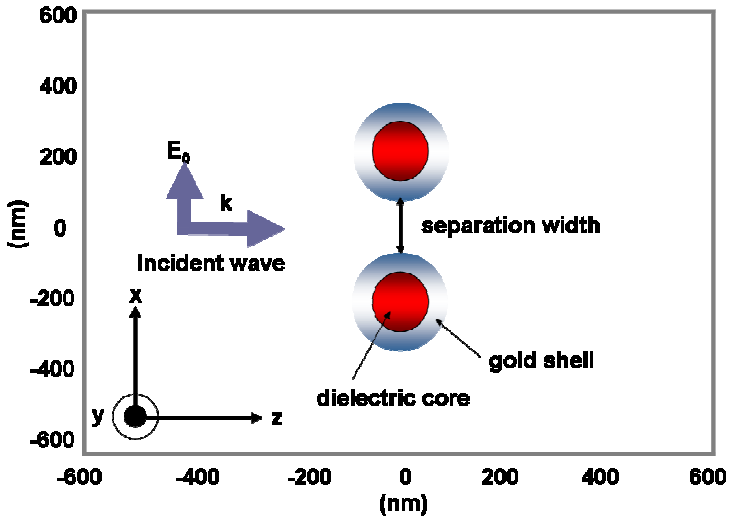

Figure 5.1 Schematic diagram of the geometrical arrangement of the dielectric-core gold–shell nanocylinder pair.

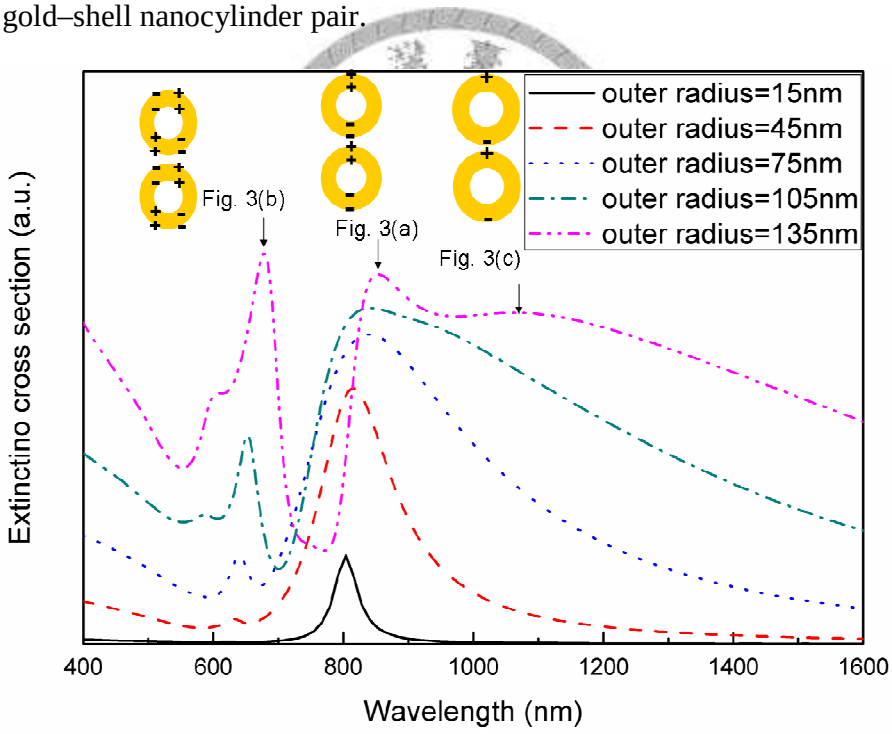

Figure 5.2 The extinction spectra as a function of size of the silica-core gold–shell nanocylinder pair from the outer radius of 15–135 nm. The ratio of the outer radius to inner radius is fixed at 6:5 and the ratio of the outer radius to the inter-nanocylinders spacing at 5:1.

15nm, the plasmon mode, near 800nm, corresponds to the in-phase symmetric dipolar (SD) mode. As the size increases, because of the phase retardation effect, the resonance wavelength of the SD mode also increases. There are other two peaks at shorter wavelength in the spectra which are the in-phase symmetric quadrupolar (SQ) mode and the in-phase symmetric octopolar (SO) mode. We can't observe the out-of phase plasmon modes in the spectrum because the out-of-phase plasmon modes have zero dipole moment and thus can't be excited by incident light. In addition to these plasmon modes discussed above, we can see in figure 5.2 that as the outer radius on the nanocylinder increases to 135nm, an additional in-phase dipolar plasmon mode shows up near 1085nm.

The origin of this new plasmon mode is studied by finding the electric field intensity of the silica-core gold-shell nanocylinder pair with outer radius of 135nm and the results are shown in figure 5.3. In these figures, the normalized electric field intensity distributions of the core-shell nanocylinder system are found by propagating plane waves at their respective plasmon resonance wavelengths. The results show that for the resonances that occur at 650 nm (figure 5.3(a)) and 850 nm (figure 5.3(b)), there is a non-uniform electric field intensity distribution inside the dielectric core. The non-uniform electric field intensity is due to the formation of the cavity modes inside the dielectric core, which implies that there is a non-zero charge distribution in the inner surface of the gold shell of the nanocylinder. However, for the electric filed intensity of the plasmon mode near 1085nm shown in figure 5.3(c), we can find that the amplitude of the electric field inside the dielectric core is zero. This implies that for this resonance mode, there are no induced charges at inner surface of the gold shell in the nanocylinder. We can thus infer that this

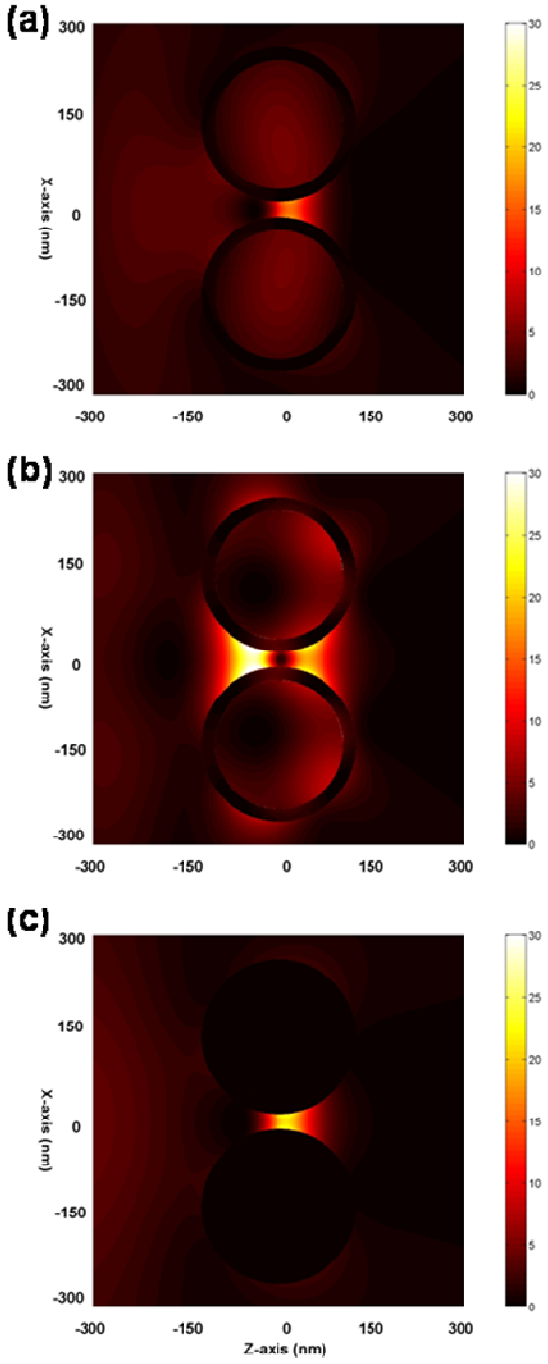

Figure 5.3 The normalized electric field intensity at the respective coupling plasmon modes wavelength of a silica-core gold–shell nanocylinder with outer radius of 135 nm and inner radius of 112.5 nm. Wavelengths of the incident light are (a) 851 nm, (b) 680 nm, and (c) 1085 nm.

special plasmon mode is resulted from the coupling of the electrons at outer surfaces between the two core-shell nanocylinders, similar to the coupling of surface plasmon between a pair of solid gold nanocylinders. This conclusion is also supported by the extinction spectra (shown in figure 5.4) obtained for a pair of solid gold nanocylinders with the same diameters as the outer diameter of the core-shell nanocylinders. We can see that resonance wavelength of both the solid gold nanocylinder pair and the core-shell nanocylinder pair occur at 1085 nm when the outer diameter of the nanocylinder is 135 nm. These results indicate that the appearance of this resonance mode is due to the metallic screening effect. As the resonance wavelength related to this plasmon mode is larger than that of known plasmon modes in the core shell nanocylinder pair, this plasmon mode can be observed in the spectrum. Because the skin depth of the gold near the resonance wavelength of 1085nm is small, the electric field is completely screened by the metal, no electric field, and no charge could be found in the inner side of the metallic shell.

In the following sections we will proof this special plasmon mode solely depends on the electrons at the outer surfaces of the nanocylinder pair by varying the dielectric core and shell thickness. The dependence of this plasmon mode on the permittivity of the dielectric core is studied in this section. In figure 5.5, we study the spectral characteristics of a dielectric-core gold-shell nanocylinder pair with outer radius of 135nm and inner radius of 112.5nm, for dielectric cores with permittivities of 2.1, 2.6, 3.3, and 4.1, respectively. The simulation results show that except for the plasmon mode near 1080nm, the resonance wavelengths of the other plasmon modes are red-shifted with increasing the permittivity of the dielectric core [14]. When the permittivity of the dielectric core is

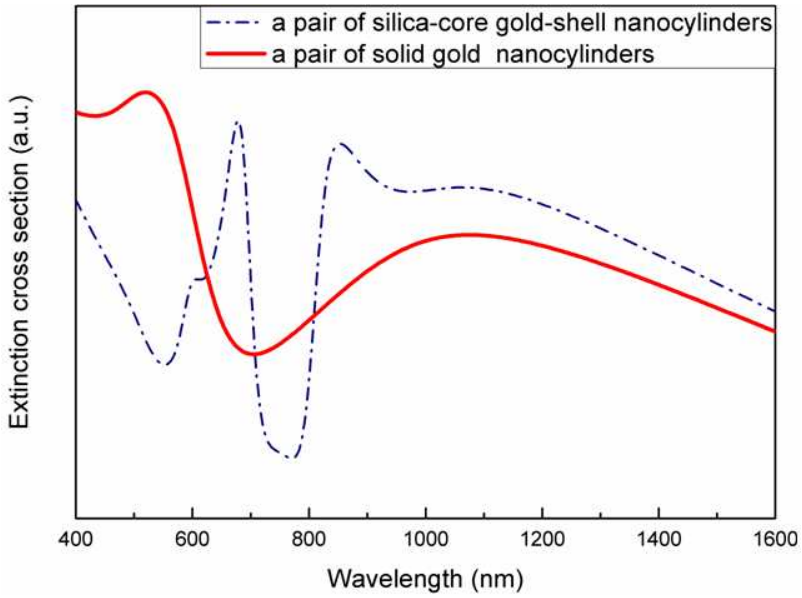

Figure 5.4 The comparison of extinction spectra between a dielectric-core gold-shell nanocylinder pair and a solid gold nanocylinder pair. Both of them have the same outer radius 135nm.

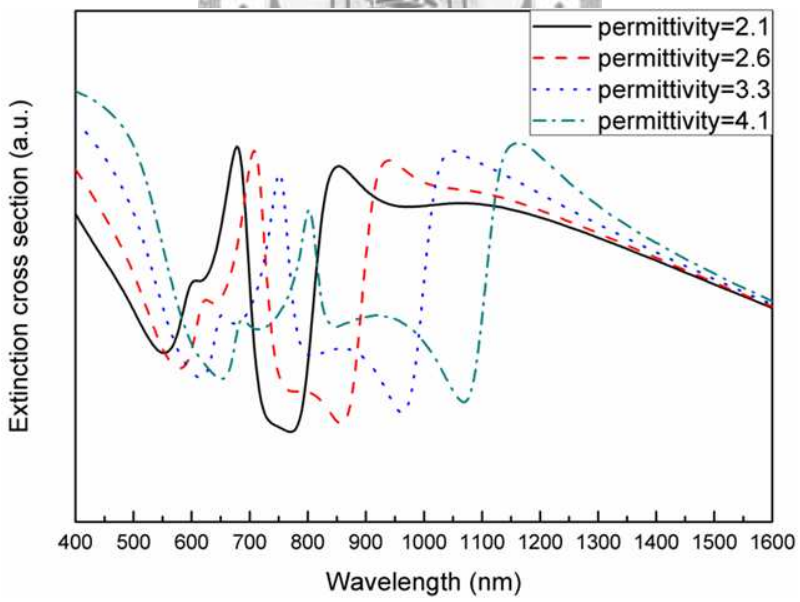

Figure 5.5 The dependence of the extinction spectra of the nanocylinder pair with outer radius of 135 nm and inner radius of 112.5 nm on the permittivity of the dielectric core.

larger than 3.3, the plasmon mode resulted from the outer surface charges near 1085nm disappears. This is because for comparably large dielectric-core gold-shell system, the symmetric dipolar (SD) mode inside the nanocylinder has the cavity resonance nature, which is similar to one-dimensional Fabry–Pérot resonance. A higher permittivity reduces the reflectance at the boundary of gold/dielectric due to a closer match in the magnitude of the real part of the dielectric constant and leads to reduce the blocking EM wave effect. Therefore, as the permittivity of the dielectric core increases, this plasmon mode disappears because the light can penetrate through the metallic shell.

We can also observe that as the permittivity of the dielectric core increases, an interesting weak plasmon mode near 924nm appears in the spectra. The weak plasmon mode corresponds to in-phase antisymmetric dipolar plasmon mode whose antisymmetric dipolar mode has an antisymmetric alignment of the inner and outer dipolar mode of the core-shell nanocylinder.

The existence of this plasmon mode in the extinction spectrum can be also controlled by varying the thickness of the metallic layer as well as the radius of the dielectric core. In order to observe this plasmon mode more clearly, we are able to enhance the screening effect and this can be achieved by increasing the thickness of the metallic shell. In figure 5.6 (a), the spectra were taken with the inner radius fixed at 112.5nm, the inter-nanocylinder separation distance fixed at 27nm, and the outer radius varied from 135nm to 165nm with an interval 10nm (corresponding to the thickness of the metallic shell from 22.5 nm to 52.5 nm). We can see clearly the existence of the resonance mode at 1085 nm in this figure when the thickness of the metallic shell increases. This resonance mode can also be made to disappear by changing the cavity confinement effect. The dependence of

the extinction spectra of the nanocylinder pair with the dielectric core permittivity 2.1, the outer radius 135nm, the inter-nanocylinder separation distance 27nm, and the inner radius varied from 117.5nm to 125nm on core-shell dimensions is shown in figure 5.6(b).

As the in-phase symmetric dipolar mode is broadened and shift to longer wavelength due to less cavity confinement, the plasmon mode resulted from the coupling of the electrons at outer surfaces of the nanocylinder pair disappear when the resonance wavelength of the in-phase symmetric dipolar mode is larger than its resonance wavelength. In addition to the permittivity of the dielectric core and the thickness of the gold shell, we can also tune the plasmon resonance modes by varying the separation distance between the two nanocylinders. The dependence of the extinction spectra of the nanocylinder pair with the dielectric core of permittivity 2.1, the outer radius of 135nm, the inner radius of 112.5nm, and the gap width between the nanocylinder pair varied from 25nm to 2.5nm is shown in figure 5.6(c). As the gap width between the nanocylinder pair decreases, the screening plasmon mode is stronger and red-shifted due to the larger coupling between the outer surfaces of the two nanocylinders.

5.4 Conclusion: two important factors that give rise to intense electric field can be applied in the surface enhanced spectrospies: one is hybridization plasmons and the other is the lightning-rod effect

In conclusion, we have shown that the plasmon modes of a dielectric-core gold-shell nanocylinder pair have an in-phase dipolar plasmon mode whose dipolar mode is from the electrons at outer surfaces of the nanocylinder pair due to the lightning-rod effect. As its plasmon resonance wavelength is larger than others related to the electrons at the inner

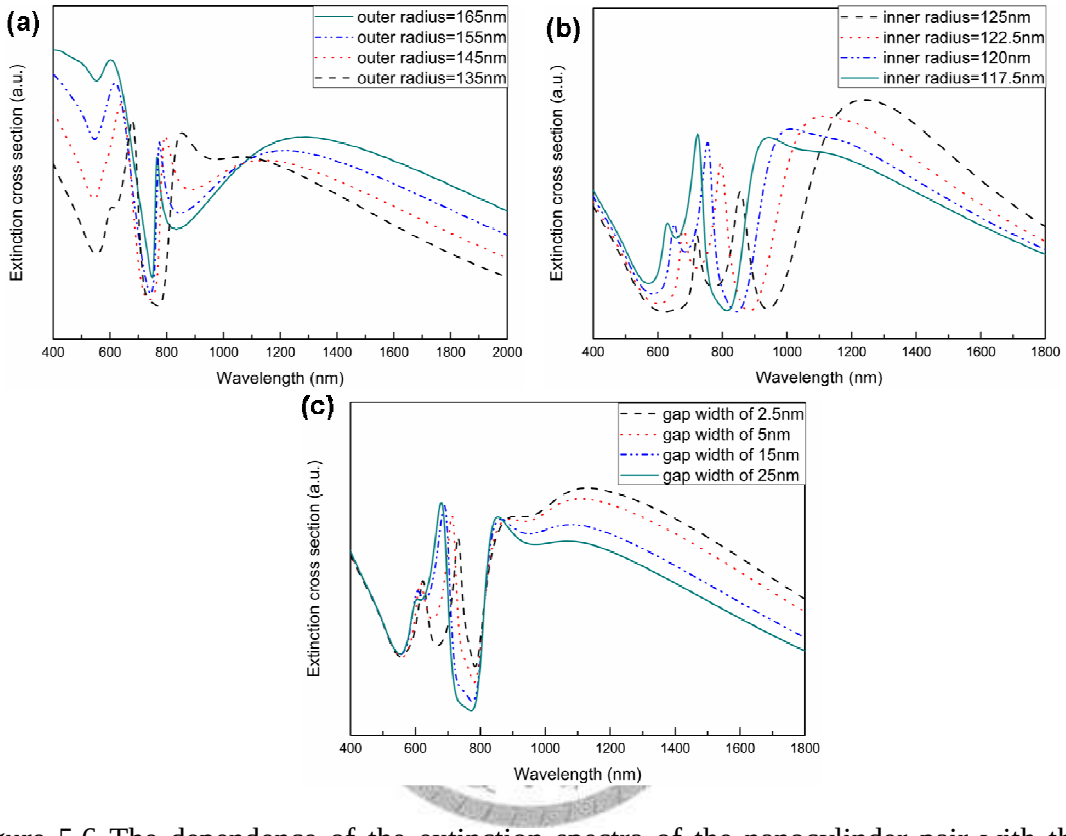

Figure 5.6 The dependence of the extinction spectra of the nanocylinder pair with the dielectric core of permittivity 2.1 on core-shell dimensions. (a) for different outer radius at fixed inner radius of 112.5nm , (b) for different inner radius at fixed outer radius of 135nm, and (c) for different gap width of the nanocylinder dimer at fixed outer radius of 135nm and inner radius of 112.5nm.

surface, it can be observed in the spectrum due to EM wave blocking by the gold shell and the gold/dielectric boundary. Therefore, we can control the existence of this plasmon mode by changing the shell thickness and the permittivity of the dielectric core. We expect that our findings can improve let us have a better understanding of the plasmonic properties and enable us to have better ability for designing a device tailored for specific applications such as surface enhanced Raman scattering (SERS) and surface enhanced infrared absorption spectra (SERIA). Thus we can infer two important factors that give rise to intense electric field can be applied in the surface enhanced spectrospies: one is hybridization plasmons and the other is the lightning-rod effect.

References

[1] J. Aizpurua, P. Hanarp, D. S. Sutherland, M. Kall, G. W. Nryant, and F. J. Garcis de Abajo, Phys. Rev. Lett. **90,** 057401 (2003).

[2] J. B. Lassiter, J. Aizpurua, L. I. Hernandez, D. W. Brandl, I. Romero, S. Lal, J. H. Hafner, P. Nordlander, and N. J. Halas, Nano Lett. **8**, 1212 (2008).

[3] H. Wang, Y. Wu, B. Lassiter, C. L. Nehl, J. H. Hafner, P. Norlander, and N. Halas, Acc. Chem. Res. **40**, 10856 (2006).

[4] H. Wang, D. W. Brandl, F. Le, P. Norlander, and N. J. Halas, Nano Lett. **6**, 827 (2006).

[5] E. Prodan, C. Radloff, N. J. Halas, and P. Norlander, Science **302**, 419 (2003).

[6] D. W. Brandl, C. Oubre, and P. Norlander, J. Phys. Chem. B **123**, 204701 (2005).

[7] C. Oubre, and P. Norlander, J. Phys. Chem. B **108**, 17740 (2004).

[8] J. W. Liaw, J. H. Chen, C. S. Chen, and M. K. Kuo, Opt. Express **17**, 13534 (2009).

[9] A. O. Pinchuk and G. C. Schatz, Appl. Phys. B **93,** 31 (2008).

[10] H. A. Yousif, R. E. Mattis, and K. Kozminski, Appl. Opt. **33**, 4013 (1994).

[11] J. Y. Lu and Y. H. Chang, Superlatt. Microstruct. **47**, 60 (2010).

[12] P. Johnson and R. Christy, Phys. Rev. B **6**, 4370 (1972).

[13] J. J. Penninkhof, A. Moroz, A. V. Blaaderen, and A. Polman, J. Phys. Chem. C **112,** 4146 (2008).

[14] N.K. Grady, N.J. Halas, and P. Nordlander, Chem. Phys. Lett. **399**, 167 (2004).

[15] F. Le, D. W. Brandl, Y. A. Urzhumov, H. Wang, J. Kundu, N. J. Halas, J. Aizpurua, and P. Nordlander, Acs Nano **2,** 707 (2008).

Chapter 6

Retardation-effect-induced plasmon modes in a silica-core gold-shell nanocylinder pair

6.1 Introduction to phase retardation effect

In chapter 6, we discuss the retardation effect on the plasmon modes in a silica-core gold-shell nanocylinder pair. For small nanoparticles where the quasi-static approximation is valid, only plasmon resonance modes containing dipole moments can be excited by the external light. Several recent studies have shown that by breaking the symmetry of a nanostructure, non-dipolar plasmon modes can be excited [1-2]. Another mechanism for exciting non-dipolar plasmon modes is phase retardation effect [3]. When the size of nanostructures is larger than a quarter of the wavelength of the incident wave, the spatial retardation effect over the volume of the nanostructure should be considered. In this chapter, we use the 2-D finite different time domain method to study the optical properties of a pair of silica-core gold-shell nanocylinders. The extinction spectra for the nanocylinder pair with different sizes and separation widths are studied in detail to understand the effect of the phase retardation effect on the plasmon oscillation in a nanocylinder pair.

6.2 Calculation methods

In chapter 6, the FDTD calculations [4] were done using a mesh size of 0.25 nm, a time step of 4.16666e-19s, and a Courant number of 0.5. The program codes have been

checked with the analytical theory [5], for a single silica-core gold-shell nanocylinder, as shown in the inset of figure 6.1. The permittivity of silica is taken as 2.1. The optical response of gold is modeled using the three critical point pole pairs (CP3) model [6] which provides a good fit to tabulated experimental data [7]. The values of fitting parameters can be found in [6]. The geometrical arrangement of the nanocylinder pair and the incident wave is shown in figure. 6.1, the propagating direction of the incident wave is along the axis that connects the nanocylinder pair, and the electric field of the incident wave is perpendicular to this axis.

6.3 Results and Discussion

We first investigate the spectral characteristics of the silica-core gold-shell nanocylinder pair by fixing the ratio of the outer radius to inner radius at 6:5 and the ratio of the outer radius to the inter-nanocylinders spacing at 5:1, and by changing the outer radius from 15nm to 135nm with a 15nm interval. In figure 6.2 the simulation results show that for outer radius of 15nm, only plasmon modes containing electric dipole moments can be induced by incident light. This is because in this case the quasi-static approximation is valid, so that the electromagnetic field across the extent of the nanocylinder pair can be assumed to be uniform. This plasmon mode, near 720nm, corresponds to in-phase symmetric dipole-dipole interaction mode, and the symmetric dipole mode is a result of the electrons at the inner surface of the core-shell nanocylinder aligned symmetrically with the electrons at the outer surface [8]. For outer radius of 30nm, the out-of-phase symmetric dipole-dipole interaction mode, near 790nm, appears in the spectrum. This out-of-phase plasmon mode is excited by the phase retardation effect. The strength of this

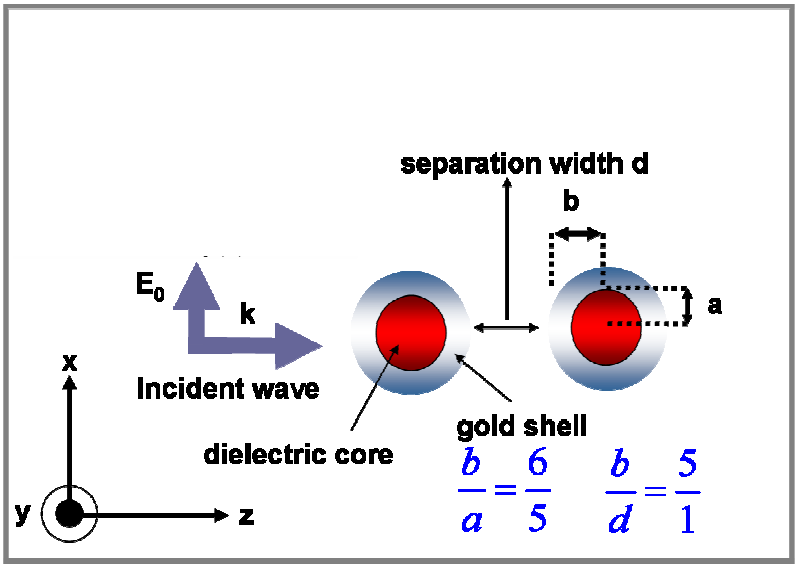

Figure 6.1 The Schematic diagram of a silica-core gold-shell nanocylinder pair and the incident direction is along the axis of the pair.

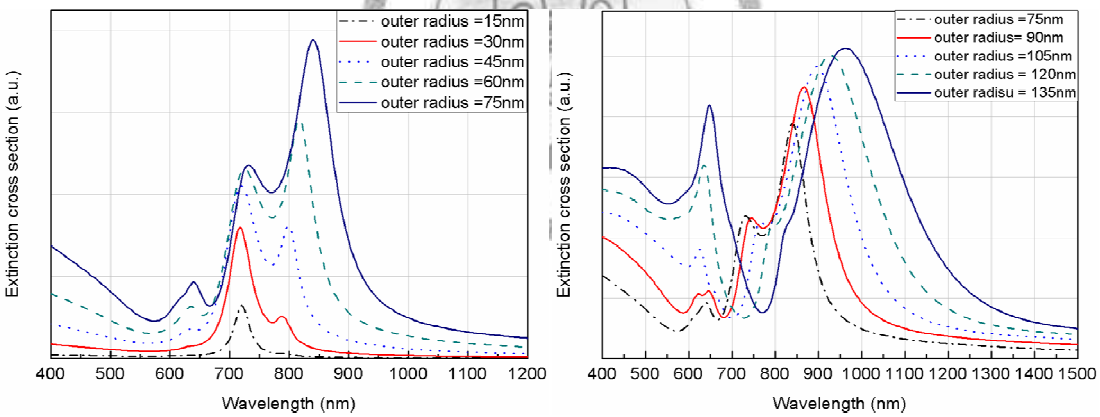

Figure 6.2 The extinction spectra as a function of radius of the silica-core gold-shell nanocylinder pair is studied from the outer radius of 15nm to 135nm. The core-shell nanocylinder pair is fixed the ratio of the outer radius to inner radius at 6:5 and the ratio of the outer radius to the inter-nanocylinders spacing at 5:1.

out-of-phase mode increases with the size of the nanocylinder pair. When the outer radius of the nanocylinder reaches 60nm, the out-of-phase symmetric dipole-dipole interaction mode becomes dominant in the extinction spectrum.

In addition to the dipole mode, the in-phase symmetric quadrupole-quadrupole interaction mode starts to appear at around 645 nm when the outer radius of the nanocylinder is 45 nm. The appearance of the quadruple mode is also the results of the phase retardation effect. The strength of this quadrupole-quadrupole interaction mode increases as the outer radius of the nanocylinder increases. The quadrupole-quadrupole interaction mode, in addition to the in-phase mode, can also have out-of-phase mode. For outer radius of 90nm, the extinction spectrum exhibits a double peak structure: one mode, near 645nm, is the in-phase symmetric quadrupole-quadrupole interaction mode and the other mode, near 625nm, is the out-of-phase symmetric quadrupole-quadrupole interaction mode. Because the retardation effect enhances the out-of-phase mode over the in-phase mode when the size of the nanocylinder increases, the strength of the out-of-phase grows in intensity. We can see in the figure that the resonance wavelength of this out of phase mode also increases, taking over the position originally occupied by the in-phase mode as the size of the nanocylinder increases. At the end the only quadrupole–related feature that can be seen in the spectrum is the out-of-phase quadrupole-quadrupole interaction mode.

The energy shifts in these plasmon modes have a notable distinction. The coupling between symmetric dipole modes of the nanocylinder pair leads to in-phase and out-of-phase symmetric dipole-dipole interaction modes. The resonance wavelengths of the out-of phase and in-phase symmetric dipole-dipole modes are red-shifted and blue-shifted as

compared to the original uncouple plasmon resonance energy, respectively. However, although the coupling between the symmetric quadrupole modes also results in the in-phase blue-shifted and out-of-phase red-shifted quadrupole-quadrupole resonance wavelengths but the resonance energy shifts in in-phase and out-of-phase symmetric dipole-dipole interaction modes are opposite to that of symmetric quadrupole-quadrupole interaction modes.

The shift in the resonance energy of localized surface plasmon modes in the coupled system can be understood by considering the restoring force of the coupled system. The resonance frequency of the plasmon oscillation is determined by the restoring force arising from Coulomb attraction between electron and nuclei and is thus sensitive to the electron charge distribution. In order to explain how the charge distribution affects the spectral behavior of the nanocylinder we show the charge distribution for each resonance mode in figure 6.3. The charge distribution of the out-of-phase dipolar plasmon mode near 860nm is shown in figure 6.3 (a). We can see in this figure that because same type of charges are distributed on the opposite sides of the two nanocylinders, the restoring force acting on a cylinder is reduced by the charge on the opposite side of another nanocylinder. This reduction in the restoring force makes the out of dipolar plasmon mode have a longer resonance wavelength than an uncoupled system. On the other hand, the resonance wavelength of the in-phase dipolar plasmon mode is blue-shifted due to the increase of the restoring force as same type of charges are distributed on the same positions in the two nanocylinders (figure 6.3 (b)). The charge distribution of the quadrupole plasmon mode, near 650nm, is shown in figure 6.3 (c). We can see that for the in-phase quadrupole mode the restoring force acting on a cylinder is reduced by the charge

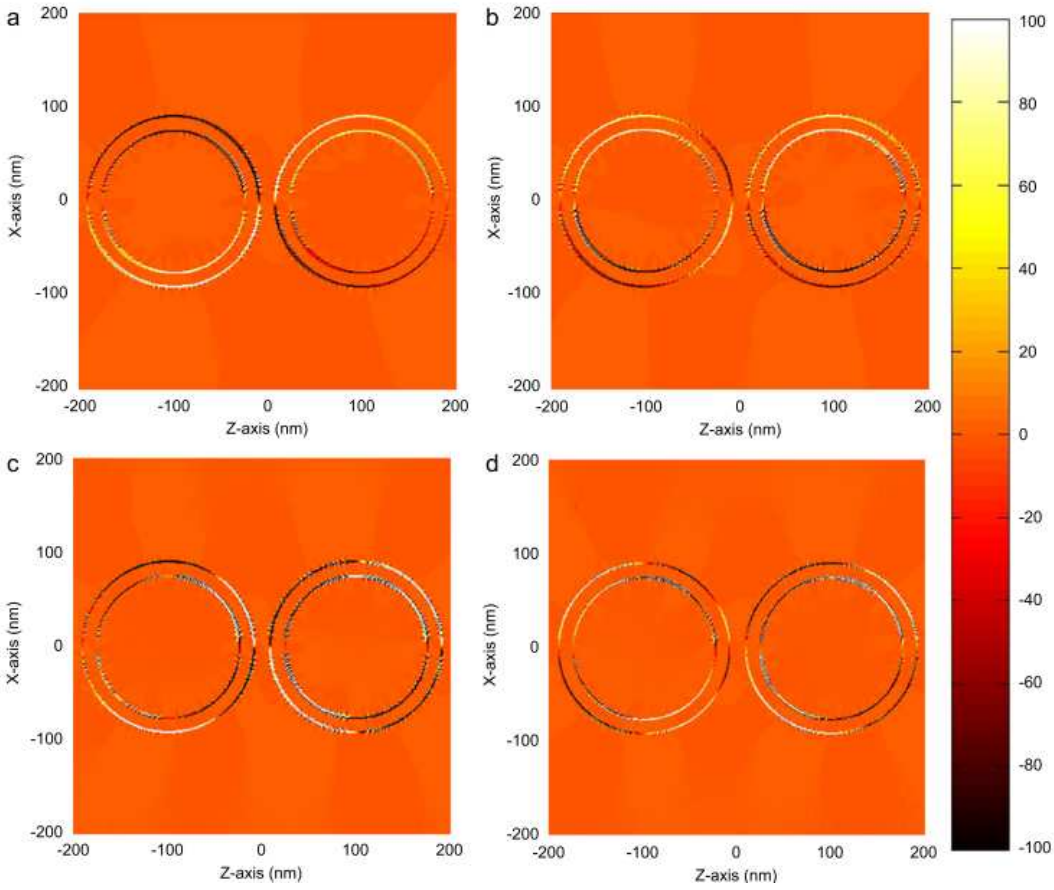

Figure 6.3 The charge distribution at the respective coupling plasmon resonance wavelengths of a silica-core gold-shell nanocylinder pair with outer radius of 90 nm and inner radius of 75nm. Wavelengths of the incident light are (a) 870nm, (b) 740nm, (c) 650nm, and (d) 625nm.

distribution near the gap of the other cylinder. As a result, the plasmon resonance wavelength of the in-phase quadrupole-quadrupole interaction has a longer wavelength than the resonance wavelength of the quadruploe mode of a single ore-shell nanocylinder. On the contrary, for the charge distribution in figure 6.3 (d), which corresponds to the charge distribution of the out-of-phase quadruple-quadruple interaction mode, the force constant in the nanocylinder is increased. Therefore, the out-of-phase quadrupole-quadrupole interaction plasmon mode has a shorter resonance wavelength, as compared to an uncoupled nanocylinder.

We also investigate the normalized electric field intensity at the respective plasmon modes of a silica-core gold-shell nanocylinder pair with the same geometry as above in figure 6.4. The simulation results show that the maximum electric field intensity changes from the left-handed core-shell nanocylinder to right-handed core-shell nanocylinder when the incident wavelength decreases. It is due to the metal screening effect because the skin depth of gold increases when the wavelength of incident wave decreases. From the normalized electric field intensity distribution at the respective plasmon modes, we find that the electric field intensity concentrates in the gap between the nanocylinder pair when the charge distributions on both sides of the gap between a core-shell nanocylinder pair are opposite in sign and attract each other. The effect of the separation width between the nanocylinder pair on the plasmon resonance modes was studied and the result is shown in figure 6.5. We can find in this figure that when the separation width increases, the phase retardation effect also increases. Therefore, the strength of the out-of-phase modes, including dipole-dipole and quadrupole-quadrupole interaction modes, increases and the in-phase interaction modes becomes invisible. In addition, we find that

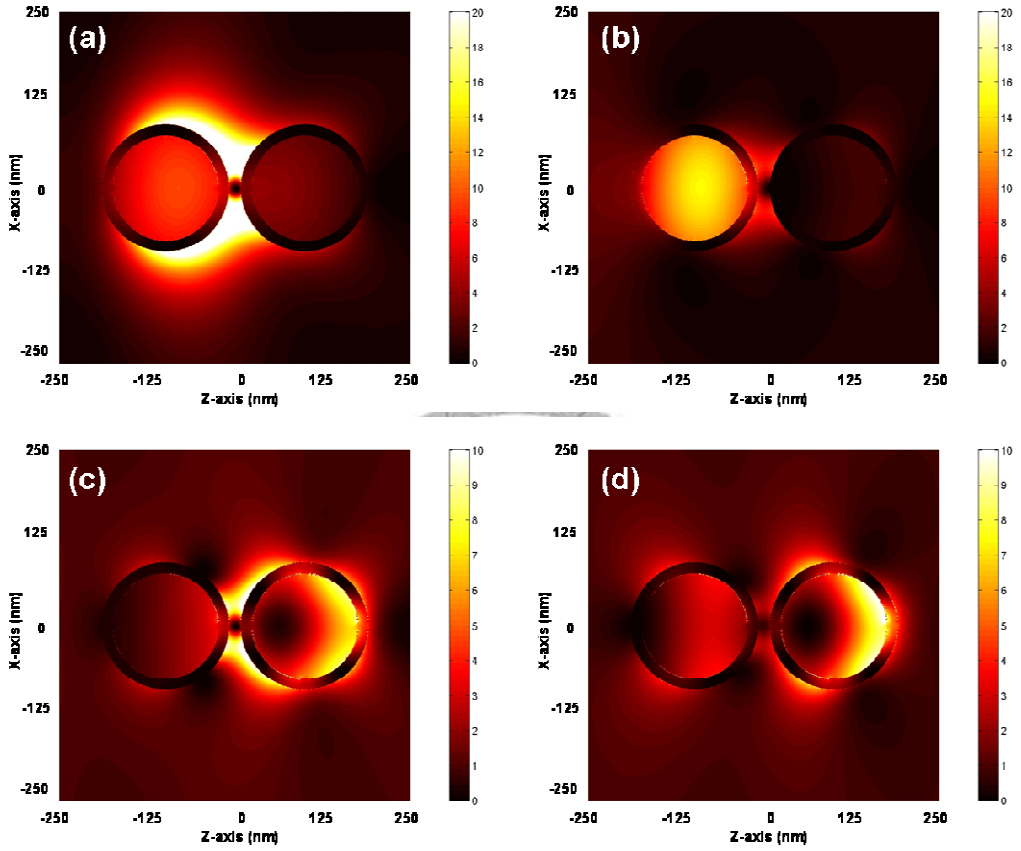

Figure 6.4 The normalized electric field intensity at the respective coupling plasmon modes of a silica-core gold-shell nanocylinder with outer radius of 90 nm and inner radius of 75nm. Fig (a) is for 870nm, Fig (b) is for 740nm, Fig (c) is for 650nm, and Fig (d) is for 625nm.

the difference of the resonance energy between the in-phase and out-of phase interaction plasmon modes is smaller when the separation width is larger. This is because the coupling between the two core-shell nanocylinders is reduced as the separation width is increased.

6.4 Conclusion

In conclusion, the retardation-effect-induced plasmon modes in a silica-core gold-shell nanocylinder pair are investigated by two dimension finite difference time domain method. The strength of this dipolar out-of-phase mode increases with the size of the nanocylinder pair and can have an intensity that is stronger than the non-retardation–effect-induced in-phase dipolar mode when the size of the nanocylinder is large enough. In addition to the dipole mode, quadrupole-quadrupole interaction mode starts to appear at around 645 nm when the outer radius of the nanocylinder is 45 nm. The quadrupole-quadrupole interaction modes can have both the in-phase and out-of-phase modes. Because the retardation effect enhances the out-of-phase mode over the in-phase mode, when the size of the nanocylinder increases, the strength of the out-of-phase mode grows in intensity, taking over the position originally occupied by the in-phase mode, and at the end becomes the only feature of the quadrupole-quadrupole interaction mode in the spectrum. The charge distributions in the nanocylinders for these resonance modes were studied to explain the energy shift observed in this coupled nanocylinder pair system.

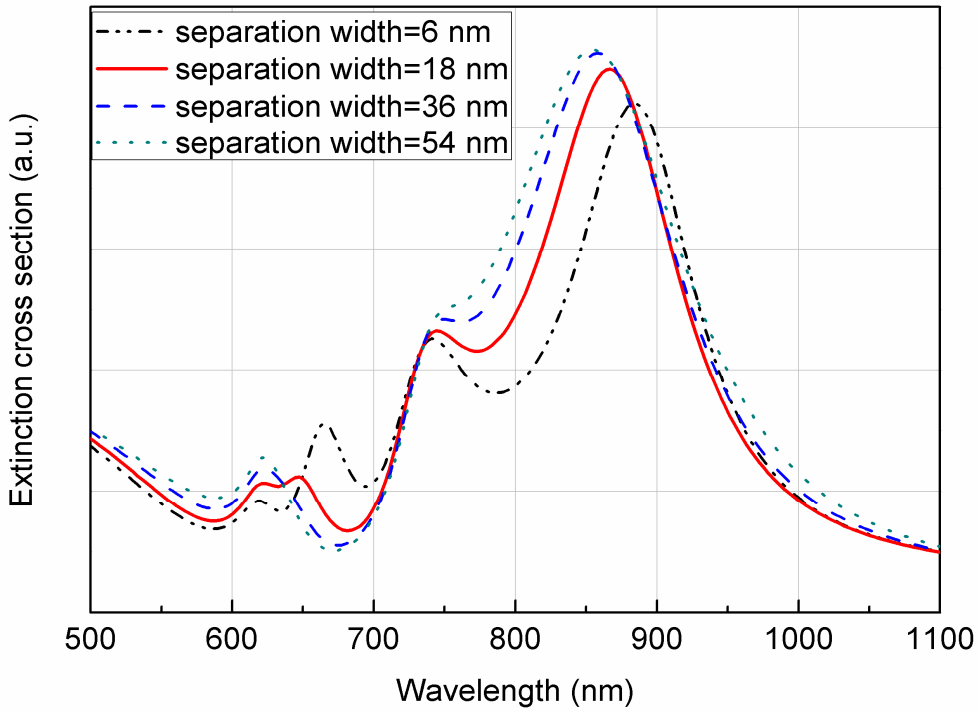

Figure 6.5 The dependence of the extinction spectrum of a pair of core-shell nanocylinders with outer radius of 90 nm and inner radius of 75nm on the separation width between the nanocylinder pair.

References

[1] H. Wang, Y. Wu, B. Lassiter, C. L. Nehl, J. H. Hafner, P. Norlander, and N. J. Halas, Proc. Natl. Acad. Sci. USA **103**, 10856 (2006) .

[2] V. A. Fedotov, M. Rose, S. L. Prosvirnin, N. Papasimakis, and N. I. Zheludev, Phys. Rev. Lett. **99**, 147401 (2007).

[3] J. P. Kottmann and O. J. F. Martin, Opt. Lett. **26,** 1096 (2001).

[4] A. Taflove and S. C. Hagness, Computational Electrodynamics: The Finite Difference Time Domain Method, 3rd ed, Artech House, 2005.

[5] H. A. Yousif, R. E. Mattis, and K. Kozminski, Appl. Opt. **9,** 4012 (1994).

[6] J. Y. Lu and Y. H. Chang, Superlattices Microstruct. **47**, 60 (2010).

[7] P. B. Johnson and R. W. Christy, Phys. Rev. B **6**, 4370(1972).

[8] J. Aizpurua, P. Hanarp, D. S. Sutherland, M. Kall, G. W. Bryant, and F. J. Garcia de Abajp, Phys. Rev. Lett. **90**, 057401 (2004).

Chapter 7

Optical singularities associated with the energy flow of two closely spaced core-shell nanocylinders

7.1 Introduction to optical singularities

The energy flow of an electromagnetic (EM) wave can exhibit unusual and complex pattern in the neighborhood of points where the amplitude of the field is zero. The phase singularities in the energy flow that was addressed in the seminal paper by Nye and Berry [1], has developed into an exciting field of optics, called singular optics [2]. For a metallic nanoparticle, it is shown that light scattering by such a particle exhibits features such as optical whirlpools [3] and optical vortices near the nanoparticle [4]. Optical vortices have also been observed in optical fibers, in nonlinear Kerr media [5], in super lens [6], and in the near field diffracted by subwavelength apertures [7–9]. The application of the singular optics includes nanoscale resolution in the focal plane of an optical microscope and optical trapping of viruses [10] and small particles [11].

A seemingly unrelated field in the study of the core-shell nanostructures such as nanorices [12], nanorings [13], and nanoshells [14] is of special interest due to the highly tunable localized surface plasmon modes. Such structures give rise to very large enhancement in the junction formed by the pair of the particles, which make them attractive as SERS substrate [15]. The dependence of the optical properties of the core-shell nanostructures on the size, dielectric core, shape, and surrounding medium has been an active field of research and can be found in numerous studies in the literature.

However, the optical singularities associated with the energy flow in these systems have not been investigated in detail yet. In this work we report our studies on the optical singularities associated with the energy flux of two closely spaced dielectric-core gold-shell nanocylinders.

Two-dimensional finite difference time domain method (FDTD) was employed for this study. For light polarized parallel to the axis connecting the pair, there are four zero energy points in the energy flow diagram, two saddle points and two optical vortices. Among these four points, the saddle points are outside the cylinders and the optical vortices are inside the cylinders. Both the width of the gap between the nanocylinder pair and the value of the permittivity of the dielectric core were found to have strong influence on the rotating direction of the optical vortices and their effects on the properties of the optical vortices were studied in detail.

7.2 The phase of the Poynting vector

The phase of the Poynting vector, ϕ_s , is defines as

$$\sin\phi_S \equiv S_z(x,z)/\left|\vec{S}\right|,$$

$$\cos\phi_S \equiv S_x(x,z)/\left|\vec{S}\right|, \qquad (7.1)$$

where $\left|\vec{S}\right|$ is the modulus of $\vec{S}$. At the point where the amplitude of the energy flux is zero, the phase $\phi_S(x,z)$ at that point is undefined according to equation (7.1) and thus it is a phase singular point. When the phase of the Poynting vector is singular, there are three possible situations in its neighborhood: (a) a rotating energy flow (optical vortex), (b) a saddle point, and (c) a sink or a source. In this work, the magnitude of the rotation and direction of the rotation of the optical vortex is called the circulation of the optical vortex

and is defined as,

$$Circulation = \int \nabla \times \vec{S} \cdot d\hat{a} \tag{7.2}$$

where the surface integral of the magnitude of $(\nabla \times \vec{S})_y$ is summed over the surface inside the dielectric core of the core-shell nanocylinder. When the circulation is larger than zero, it means that the rotating direction of the optical vortex is counterclockwise and the optical vortex is a right-handed optical vortex (RV). On the other hand, if the circulation is smaller than zero, it means that the rotating direction of the optical vortex is clockwise and the optical vortex is called a left-handed optical vortex (LV).

7.3 Numerical method

FDTD [16] was used to investigate the near field optical responses of the dielectric-core gold-shell nanocylinder pair. The optical response of gold is modeled using the three critical point pole pairs (CP3) model [17, 18]. The CP3 model can be expressed as

$$\varepsilon(\omega) = \varepsilon_\infty + \frac{\sigma/\varepsilon_0}{i\omega} + \sum_{p=1}^{3} \left(\frac{A_p \Omega_p e^{i\phi_p}}{\Omega_p - \omega - i\Gamma_p} + \frac{A_p \Omega_p e^{-i\phi_p}}{\Omega_p + \omega + i\Gamma_p} \right) \tag{7.3}$$

And the codes have been checked with the analytical theory [19]. Our FDTD simulation domain is separated into three regions from outside to inside: absorbing boundary, scattered field region, and the total field region. The FDTD calculations were done using a mesh size of 0.5 nm, a time step of 8.3333e-19s, and a Courant number of 0.5. The geometrical arrangement of the incident EM wave and the dielectric-core gold-shell nanocylinders is shown the incident EM wave and the dielectric-core gold-shell nanocylinders is shown schematically in figure 7.1. In this configuration, the EM wave is TM polarized, i.e., the only non-zero component of the magnetic field is in the y-

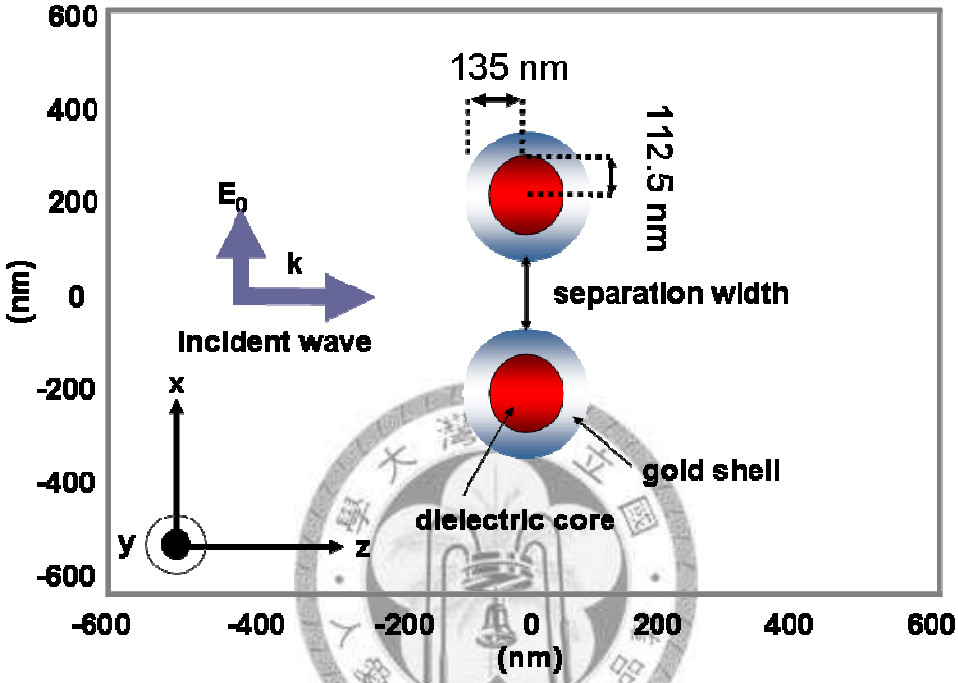

Figure 7.1 Schematic diagram of the geometric arrangement of the incident EM wave and the dielectric-core gold-shell nanocylinder pair. The propagating direction of the incident wave is in the x-direction and is perpendicular to the axis connecting the nanocylinder pair (z-direction). The electric field of the incident wave is in the x-direction.

direction. The inner radius and outer radius of the core-shell nanocylinder used in this work are 112.5nm and 135nm, respectively.

7.4 Phase singularities inside a core-shell nanocylinder pair

We first study the spectral characteristics of the core-shell nanocylinder pair in the wavelength range between 700nm and 1500nm. In this study the permittivity of the dielectric core is taken as 4.1, and the distance between the two cylinders is set at 27nm. The extinction, scattering, and absorption cross sections spectra for this system are shown in figure 7.2(a). We can find in these spectra that there are three major plasmon modes for the nanocylinder pair. The plasmon mode near 1161 nm is the in-phase symmetric dipolar (SD) mode. This plasmon mode is originated from the electrons at the inner surface of the core-shell nanocylinder aligned and oscillates symmetrically with the electrons at the outer surface [20]. The other two peaks in the figure are the in-phase antisymmetric dipolar plasmon (AD) mode near 935 nm, and the in-phase symmetric quadrupolar plasmon mode near 800nm. The charge density distributions associated with these plasmon modes are also shown in figure 7.2(a). In this work, we'll focus on the energy flow distribution in the proximity of the in-phase SD interaction mode.

The energy flow pattern of light scattering from such a core-shell nanocylinder pair of a monochromatic plane wave with incident wavelength of 1161nm is shown in figure 7.2 (b). We can see in this figure that there are four zero energy points in the energy flux diagram and these phase singularities are marked as S1, S2, RV and LV, respectively.

Among these four points, S1 and S2 are outside the cylinders and RV and LV are

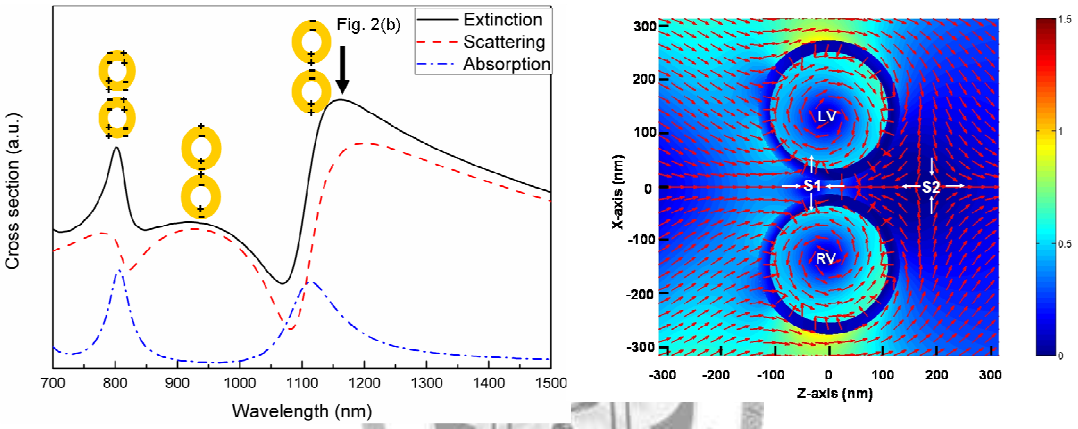

Figure 7.2 (a) The FDTD calculated extinction, scattering, and absorption spectra of a dielectric-core gold-shell nanocylinder pair with gap separation of 27nm. The permittivity of the dielectric core is 4.1. The charge distribution of the plasmon modes are shown in the inset. (b) The energy flow pattern near the nanocylinder pair.

inside the cylinders. We can find from the energy flow pattern in the figure that energy flows into S1 in z-direction and flows out of S1 in x-direction, flows into S2 in x-direction and flows out of S2 in z-direction, but for RV and LV, the energy flow circulates around these two points and deceases in magnitude as it get closer toward these two points. From the characteristics of the energy flow pattern around these four points we can identify S1 and S2 as saddle points, RV and LV as the centers of optical vortices. It is evident in these figures that optical singularities existed in the energy flux associated with two closely spaced core-shell nanocylinder pair.

7.5 The dependence of the circulating direction of the optical vortex on the inter-nanocylinder separation

In order to have a better understanding on the properties of the optical vortex associated with the nanocylinder pair, the effect of the width of the gap that separated the nanocylinder pair as well as the value of the permittivity of the dielectric core on the rotating direction of the optical vortex are studied. Figure 7.3 (a)-(d) are the energy flow patterns of the core-shell nanocylinder pair that have gap width of 20 nm, 35 nm, 70 nm, and 135 nm, respectively. As the geometrical arrangement is symmetrical with respect to the z-axis that passes through the center of the nanocylinder pair, it is not surprising to see in these figures that the rotating directions of the two optical vortices in the same figure are also symmetrical with respect to the z-axis that passes through the center of the nanocylinder pair. For the convenience of discussion we'll hence call the configuration with upper optical vortex rotating in a left-handed direction (LV) and lower vortex rotating in a right-handed direction (RV) as inward-type rotation, and the configuration

with upper right-handed optical vortex (RV) and lower left-handed optical vortex (LV) as outward-type rotation. From the energy flow patterns shown in these figures we can find that when the gap width between the nanocylinder pair are 20 nm and 35 nm the rotational type of the optical vortices are inward-type rotation, for gap width equals to 70 nm, no optical vortex could be found, but when gap width is 135nm, the rotational type of the vortices change to the outward-type rotation.

Examine these four figures carefully we can find that the relative intensity between the EM waves that flow through the gap and the outer edge (the edge that is opposite to the edge near the gap) of the cylinders play a major role in determining the circulating direction of the vortices. When the intensity of the EM wave is larger at the outer edge of the cylinder than that is in the gap, the circulating direction of the vortex follows the energy flow direction of the EM wave at the outer edge and thus the circulating direction for the upper vortex is left-handed and for the lower vortex it is right-handed. (figure 7.3 (a) and (b)). When the intensity of the EM wave is larger in the gap than that at the outer edge of the cylinder, the circulating direction of the vortex follow the energy flow direction of the EM wave in the gap and thus the circulating direction of the upper vortex is right-handed and the lower vortex is left-handed (figure 7.3 (d)). But when the strengths of the two energy flows are comparable, no vortex can be found in the energy flow pattern shown in figure 7.3 (c). Therefore, we can conclude that the gap width between the nanocylinder pair influences the strength of the energy flows in different regions and that in turn determines the rotational type of the optical vortices. A detail study of the rotating type of the optical vortices and their circulation defined by equations (7.2) as a function of the gap width was presented in figure 7.3 (e).

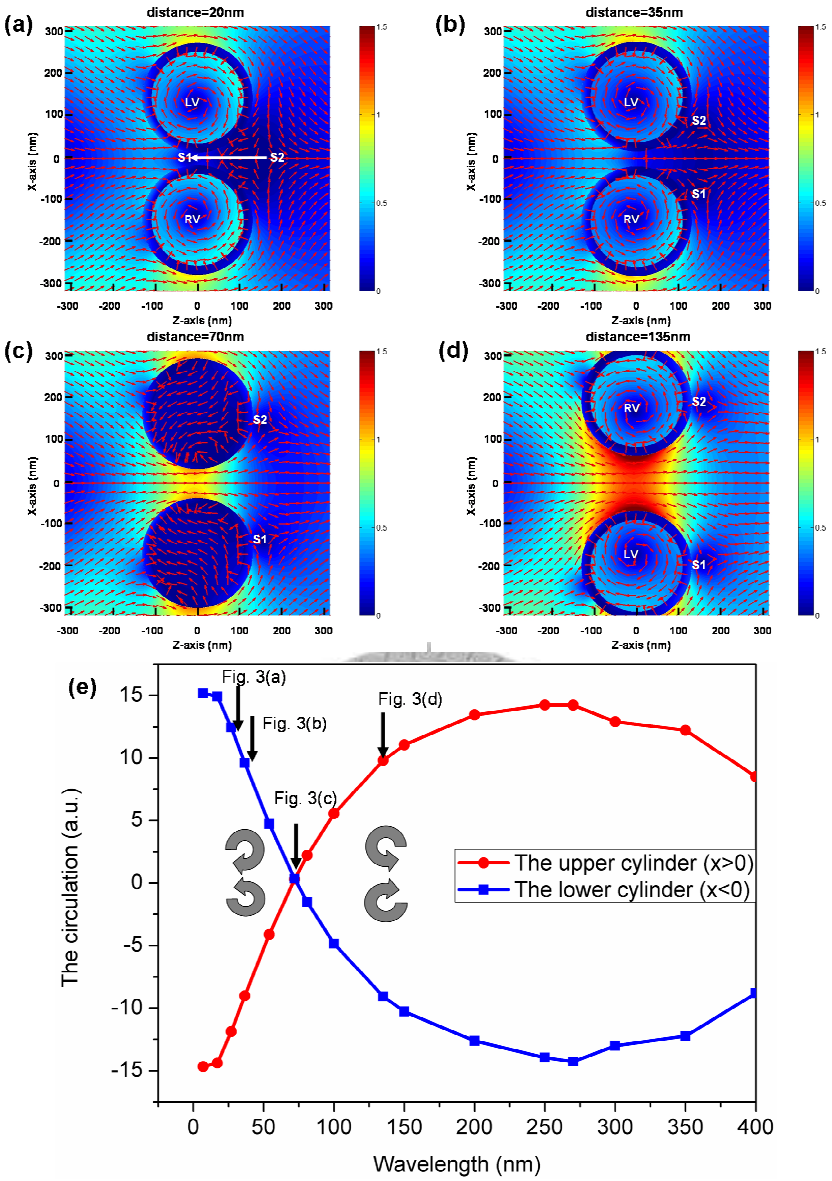

Figure 7.3 The energy flow patterns of the core-shell nanocylinder pair whose the separation distances between the nanocylinder pair are (a) is 20nm, (b) is 35nm, (c) is 70nm, (d) is 135nm. The optical vortices disappear when the separation distance is 70nm. (e) The variation of the circulation inside each core-shell nanocylinder with the separation distance between them. The circle-dotted red line and the square-dotted blue line represent the circulation inside the upper and the lower core-shell nanocylinders, respectively.

Figure 7.3(e) shows that when the gap width between the nanocylinder pair is larger than 70nm, the vortices are outward type rotation. This is because the energy flow direction of the incident wave is inclined to be gathered near the gap due to mutual coupling of the two plasmonic nanocylinders and this can be observed in figure 7.3(a)-(d). Therefore, except for the gap width between the nanocylinder pair small compared with the incident wavelength, the intensity of the EM wave is larger in the gap than that is at the outer edge of the cylinder, and thus the vortices are outward type. When the gap width between the nanocylinder pair is larger than 270 nm, the circulation of the outward type reduces due to the reduction of the near-field coupling.

7.6 The dependence of the optical vortices on the permittivity of the dielectric core

In addition to the gap width between the cylinder pair, we found that the value of the permittivity of the dielectric core can also be used to tune the rotation type of the optical vortex. Figure 7.4(a) shows the extinction cross sections of the core-shell nanocylinder pair with gap width of 27 nm and dielectric cores with permittivity of 2.1, 3.1, and 4.1, respectively, in the wavelength range between 700nm and 1600nm. The three peaks marked by the arrows at 852nm, 996nm, and 1161nm are the in-phase symmetric dipolar plasmon modes for these nanocylinder pairs. Because of the dielectric screening effect [21], the resonance wavelengths of these plasmon modes are red-shifted when the permittivity of the dielectric core increases.

The energy flow patterns of these core-shell nanocylinder pairs, calculated at their respective resonance wavelengths, are shown in figure 7.4 (b)-(d). We can see in these

figures that the rotation type of the vortices changes from the inward-type to the outward-type when the value of the permittivity of the dielectric core changes from 4.1 to 2.1. To explain the change in the rotating direction of the optical vortices, we first note that in figure 7.4 (a) the intensity of the EM wave at S1 is a saddle point and this is because, at this gap width, the gap width is much smaller the wavelength of the incident light and thus EM wave can't transmit through the gap. In this circumstance, the rotating direction of the optical vortex is dictated by the direction of the energy flow in the outer edge of the nanocylinders as was discussed in the previous section, and thus the rotational type is the inward-type when the value of the permittivity of the dielectric core is 4.1. However, as the permittivity of the dielectric core decrease, the EM wave is more likely to be trapped inside the nanocylinders then just penetrating through the nanocylinders, and the intensity of the EM wave inside the nanocylinders increases quite dramatically as the permittivity of the dielectric core decreases. The reason for this is that the cavity resonance mode inside the nanocylinders is similar to one-dimensional Fabry-Perot cavities. A higher permittivity of the dielectric core reduces the reflectance at a metal/dielectric boundary due to a closer match in the magnitude of the real part of the refractive index [22].

This EM field confinement effect inside the dielectric core, with the boundaries by the metal shell can be seen quite clearly in our simulation, the intensity of the EM field increases quite substantially from figure 7.4(b) to (d). As the EM wave that penetrates into and stays in the nanocylinders increases, the energy flow direction inside the nanocylinder will eventually be determined by the direction of EM wave that penetrates into the nanocylinders. We can see quite clearly in figure 7.4 (c) and (d) that when the

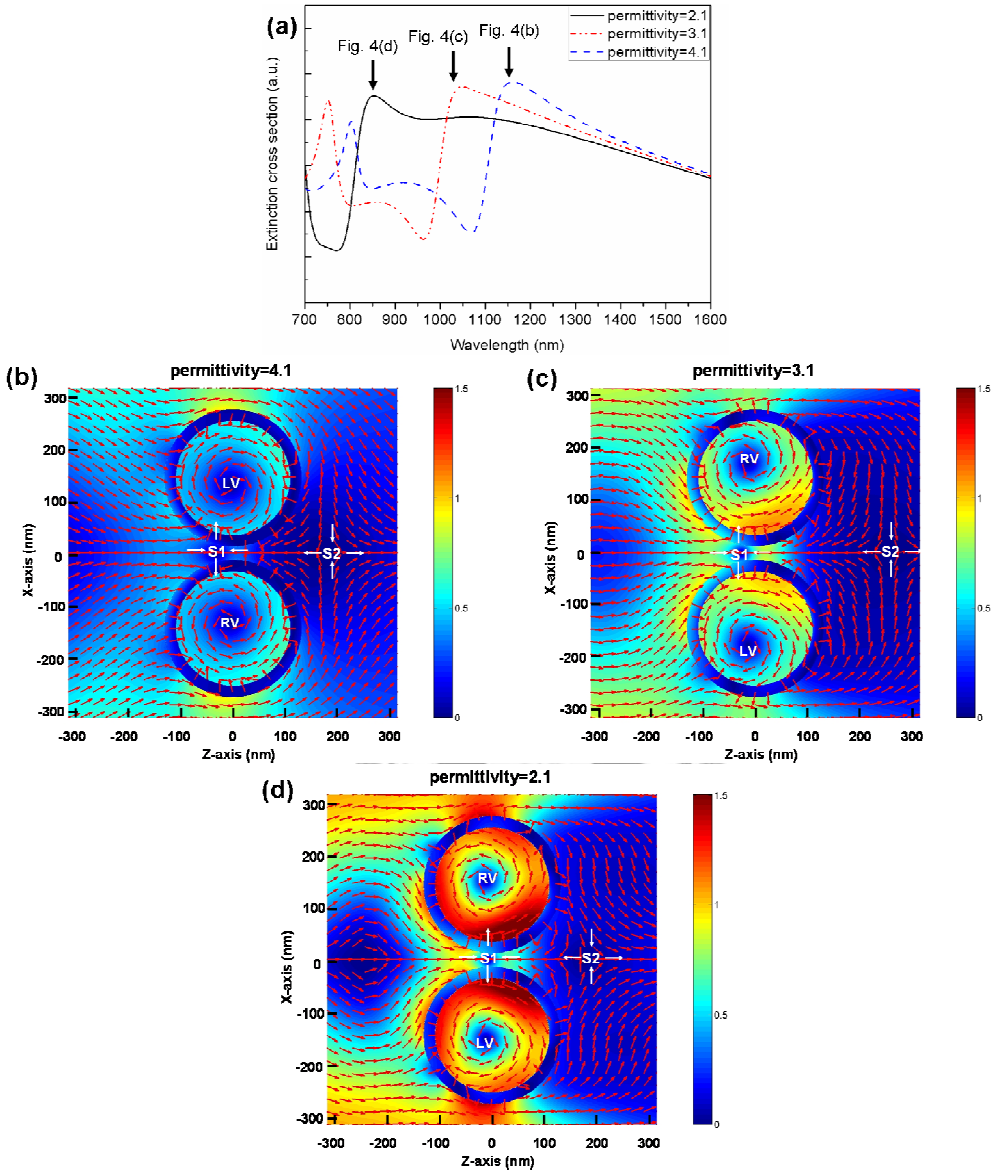

Figure 7.4 The calculated extinction spectra cross sections for the core-shell nanocylinder pair with different dielectric permittivity of 2.1, 3.1, and 4.1, respectively shown in (a). The energy flux distributions corresponding to the in-phase SD interaction modes are shown in (b), (c), and (d). Note that the rotating direction of the energy fluxes in (b) is opposite to the rotating directions of the energy fluxes in (c) and (d).

intensity of the EM wave inside the nanocylinder is larger than the intensity of the EM wave at the outer edge of the cylinders, the energy flow direction inside the nanocylinders is determined by the propagating direction of the EM wave that flow into the nanocylinder and the rotation type of the optical vortices in these cases became outward-type.

7.7 Summary

In conclusion, the energy flow associated with a pair of dielectric-core gold-shell nanocylinders were studied by two-dimension finite difference time domain method with light polarized to the axis connecting the nanocylinder pair. There are four zero energy (optical singular) points in the energy flow diagram, two saddle points and two optical vortices. Among these four points, the saddle points are outside the cylinders and the optical vortices are inside the cylinders. Both the width of the gap that separated the nanocylinder pair and the value of the permittivity of the dielectric core were found to have strong influence on the rotating direction of the optical vortices. The gap width between the nanocylinder pair affects the energy distribution near the nanocylinders and that in turns determines the rotational type of the optical vortices. The permittivity of the dielectric core determines the intensity of the EM field resonance inside the nanocylinders and thus can be used to control the energy flow direction inside the nanocylinders. Our studies show that optical vortices can be found in a core-shell nanocylinder pair and the rotating direction of the optical vortices associated with the nanocylinder pair can be controlled by changing either the spacing between the nanocylinders or by changing the permittivity of the dielectric core.

References

[1] J. F. Nye and M. V. Berry, Proc. R. Soc. London. Ser. A **336**, 165 (1974).

[2] J. F. Nye, Natural Focusing and the Fine Stuctures of Light (Institute of Physics, Bristol, 1999).

[3] M. V. Bashevoy, V. A. Fedotov and N. I. Zheludev, Opt. Express **13**, 8372 (2006),

[4] M. I. Tribelsky and B. S. Luk'yanchuk, Phys. Rev. Lett. **97**, 263902 (2006).

[5] T. W. Ebbesen, H. J. Lezec, H. F. Ghaemi, T. Thio, and P.A. Wolff, Nature (London) **391**, 667 (1998).

[6] H.F. Schouten, T.D. Visser, G. Gbur, D. Lenstra and H. Blok, Opt. Express **11**, 371 (2003).

[7] H.F. Schouten, T.D. Visser, G. Gbur, D. Lenstra and H. Blok, J. Opt. A: Pure Appl. Opt. **6**, 277 (2004).

[8] Yu. S. Kivshar and D. E. Pelinovsky, Phys. Rep. **331**, 118 (2000).

[9] G. D'Aguanno, N. Mattiucci, M. Bloemer, and A. Desyatnikov, Phys. Rev. A **77**, 043825 (2008).

[10] A. Ashkin and J. M. Dziedzic, Science **235**, 1517 (1987).

[11] K.T. Gahagan and G.A. Swartzlander, J. Opt. Soc. Am. B **16**, 533 (1999).

[12] H. Wang, D. W. Brandl, F. Le, P. Norlander, and N. J. Halas, Nano Lett. **6**, 827 (2006).

[13] J. Aizpurua, P. Hanarp, D. S. Sutherland, M. Kall, G. W. Nryant, and F. J. Garcis de Abajo, Phys. Rev. Lett. **90**, 057401 (2003).

[14] J. B. Lassiter, J. Aizpurua, L. I. Hernandez, D. W. Brandl, I. Romero, S. Lal, J. H. Hafner, P. Nordlander, and N. J. Halas, Nano Lett. **8**, 1212 (2008).

[15] M. Moskovits, Rev. Mod. Phys. **57**, 783 (1985).

[16] A. Taflove, Computational Electrodynamics: The Finite-Difference Time-Domain Method (Artech House, Boston, 1995).

[17] J. Y. Lu and Y. H. Chang, Superlatt. Microstruct. **47**, 60 (2010).

[18] P. Johnson and R. Christy, Phys. Rev. B **6**, 4370 (1972).

[19] H. A. Yousif, R. E. Mattis, and K. Kozminski, Appl. Opt. **9**, 4012 (1994).

[20] E. Prodan, C. Radloff, N. J. Halas, and P. Norlander, Science **302**, 419 (2003).

[21] N.K. Grady, N.J. Halas, and P. Nordlander, Chem. Phys. Lett. **399**, 167 (2004)

[22] J. J. Penninkhof, A. Moroz, A. V. Blaaderen, and A. Polman, J. Phys. Chem. C **112**, 4146 (2008).

Chapter 8

Multiple Metallic-shell nanocylinders for surface enhanced spectroscopes

8.1 Introduction

In chapter 8, we study the optical properties of multiple dielectric-core gold-shell nanocylinder pairs by using two-dimensional finite difference time domain method. The core-shell cylinders are assumed to be of the same dimension and composition. In the emerging field of plasmonics, dielectric-core metallic-shell nanostructures have attracted much attention due to their application in surface enhanced spectroscopies. Comparing to solid metallic particles, these core-shell nanostructures exhibit highly tunable plasmon modes that can be tuned over an extended wavelength range between visible and near infrared regions. The variation of the plasmon resonance wavelength is interpreted as originating from coupling of localized surface plasmon modes at the inner and outer surfaces of the core-shell structure [1-2].

The most widely used surface enhanced spectroscopy is surface enhanced Raman scattering (SERS) [3-4], where one wants to maximum the electric field intensity on the molecule in order to enhance the detected signals. The same effect can also be used to enhance infrared signals, which is called as surface enhanced infrared absorption (SEIRA) spectroscopy [5]. The enhancement is not as strong as for Raman spectroscopy in the visible range, but the enhancement factors is still proportional to the square of the electromagnetic field. Originally, the local field enhancement of surface plasmon

excitations in plasmonic nanostructures was mainly found in the visible and UV regions, which is suitable for SERS. Recently, nanoshell arrays have been found to possess ideal properties as a common substrate for both surface enhanced Raman scattering and surface enhanced infrared absorption spectroscopies. The reason for this is that nanoshell arrays can provide large electric field enhancement at the same spatial location in both the visible and infrared regions of the spectrum [6].

In this chapter, we investigate the plasmon modes of multiple dielectric-core gold-shell cylinder pairs for normal incidence. The simulation results show the multiple nanocylinder pairs provide large electromagnetic enhancement in the wide spectral range between the visible and infrared regions. The localized surface plasmon excitation occurring in the infrared region in spectrum is due to the efficient metallic screening effect at low frequency. The infrared plasmon resonance is identified as due to the interactions between the electrons at the outer metallic surfaces of the nanocylinders. The other plasmon modes of multiple nanocylinder pairs are only weakly red-shifted from the individual nanocylinder pair plasmon modes. Our analysis show how to tune the plasmon modes of multiple nanocylinder pairs by varying the pair-distance between the pairs, the gap-distance between the pair, the optical constant of the dielectric-core, and surrounding medium.

When the number of the cylinder pairs is three, we find that lightning rod effect results in two plasmon modes in the infrared region, which is similar to the open cavity mode of three solid metallic nanocylinder pairs presented by N. Y. Wu [7]. The strongest electric field enhancement of such a cavity mode exhibits in the gap of the second pair and the open cavity has a linear relation between the resonant wavelength and the radius of

nanocylinders. Therefore, the multiple core-shell nanocylinder pair contains the plasmon mode same as that of the solid metallic cylinder pairs at the long wavelength part of the spectrum.

8.2 Calculation methods

The FDTD calculations were done accurately using a mesh size of 0.5 nm, and a Courant number of 0.5. The program codes have been checked with the analytical theory [8]. The optical response of gold is modeled using the three critical point pole pairs (CP3) model [9] which provides a good fit to tabulated experimental data [10]. The inner radius and outer radius of the dielectric-core gold-shell nanocylinder are 60nm and 80nm, the propagating direction of the incident wave is along the axis that connects the nanocylinder pairs, and the polarization of the incident wave is parallel to this axis that connects the two nanocylinders of the pair. In this work the cylinder is the same in geometry and composition.

8.3 Results and Discussion

We first investigate the spectral characteristics of a single dielectric-core gold-shell nanocylinder pair. The geometry of the nanocylinder is shown in the inset of the figure 8.1 and the distance between the nanocylinders is 20nm. The dielectric constant of the dielectric core inside the nanocylinder is 2.1, which is the dielectric constant of the silica. From the figure 8.1 we can see that the extinction spectrum is characterized by two plasmon modes. The plasmon mode, near 700nm, corresponds to in in-phase symmetric dipole-dipole interaction mode, and the symmetric dipole mode is a result of the electrons

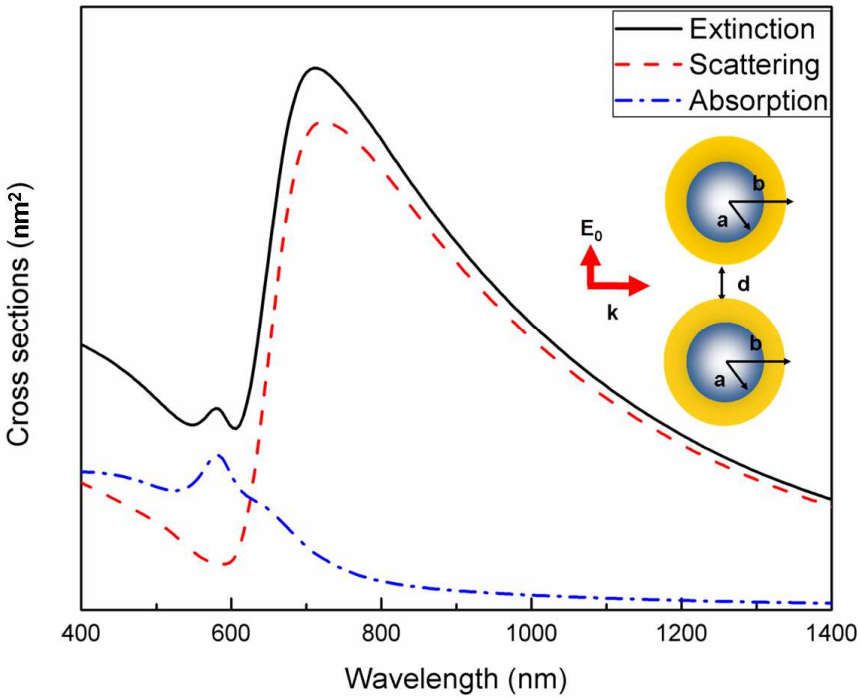

Figure 8.1 The FDTD calculated extinction, scattering, and absorption spectra of a dielectric-core gold-shell nanocylinder pair with separation distance of 20nm. The permittivity of the dielectric core is 2.1. The geometry is shown in the inset.

at the inner surface of the core-shell nanocylinder aligned symmetrically with the electrons at the outer surface [11].

The other plasmon mode, near 575 nm, corresponds to in in-phase symmetric quadrupole-quadrupole plasmon mode. We can not observe the out-of-phase plasmon mode in the spectrum. This is because the out-of-phase plasmon modes do not have any the dipole moment such that external light can not induce these modes.

When two core-shell nanocylinder pairs are brought together with the pair distance p of 20nm, the interaction between two nanocylinder pairs is strong and results in the energy splitting in the spectrum. The other parameters are the same as those shown in figure 8.1. The plasmon modes of two nanocylinder pairs are unveiled in figure 8.2, which shows four major plasmon modes in the spectrum between the visible and infrared regions. The plasmon mode, near 1100 nm, corresponds to the two in-phase symmetric dipole-dipole modes oscillating in the out-of-phase way. That is to say, when two nanocylinder pairs couple with each other, the in-phase symmetric dipole mode of a single dielectric-core gold-shell interacts with that of another nanocylinder pair. Phase retardation effect results in the out-of-phase oscillation for the two in-phase symmetrical dipole-dipole mode [14]. The plasmon mode near 890 nm is resulted from the interaction between in-phase dipole-dipole mode of the first nanocylinder pair and in-phase quadrupole-quadrupole mode of the second nanocylinder pair. The other Plasmon mode, near 820 nm, corresponds to two in-phase quadrupole-quadrupole mode oscillating in the out-of-phase way. Therefore, for normal incidence, the plasmon modes of two nanocylinder pairs are composed of the individual nanocylinder pair plasmon mode. In addition, we can find that one of the plasmon modes is excited at much longer wavelengths. The electric field distribution

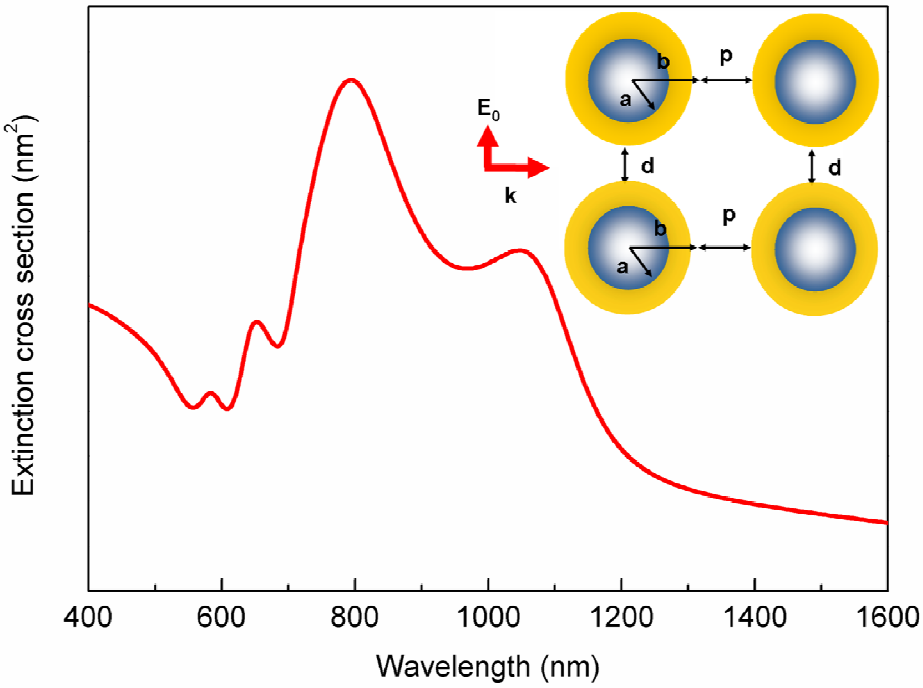

Figure 8.2 The extinction spectra of two silica-core gold-shell nanocylinder pairs with the gap width of 20nm and pair distance of 20nm.

shows that this mode is resulted from the interaction between the electrons at the outer surface of the four nanocylinders. The normalized electric field intensity is investigated by propagating a plane wave at the respective plasmon modes of two dielectric-core gold-shell nanocylinder pairs with the same geometry as above is shown in figure 8.3. We find that the electric field intensity decreases inside the dielectric core of the nanocylinder when the incident wavelength increases. This is resulted from the metal screening effect because the skin depth of gold increases when the wavelength of incident wave decreases. When the incident wavelength increases to 1050nm, the incident wave can not penetrate into the nanocylinder. The maximum electric field intensity concentrates in the gap between the nanocylinders and such a phenomenon is called lightning-rod plasmon mode [13]. The electric field is completely screened by the metal, no electric field, and no induced charges could be found in the inner side of the metallic shell. This plasmon mode is resulted from the coupling of the in-phase dipolar modes formed by the electrons at outer surfaces of the core-shell nanocylinders. From figure 8.3 we can know, except for this plasmon mode near 1050nm, other plasmon modes consist of the essential plasmon modes of the core-shell nanocylinder pair. We can't observe the lightning-rod plasmon mode for a single dielectric-core gold-shell nanocylinder pairs. This is because for just a single core-shell nanocylinder pair with the outer radius of 80nm, the resonance wavelength of the in-phase dipolar mode resulted from the outer surfaces does not exist in the infrared region [16]. When two core-shell nanocylinder pair interacts with each other, such a plasmon mode can be observed. The lightning-rod plasmon mode is red-shifted to longer wavelength than those of plasmon modes resulted from coupling of the individual nanocylinder pair plasmon modes due to the pair-pair interaction.

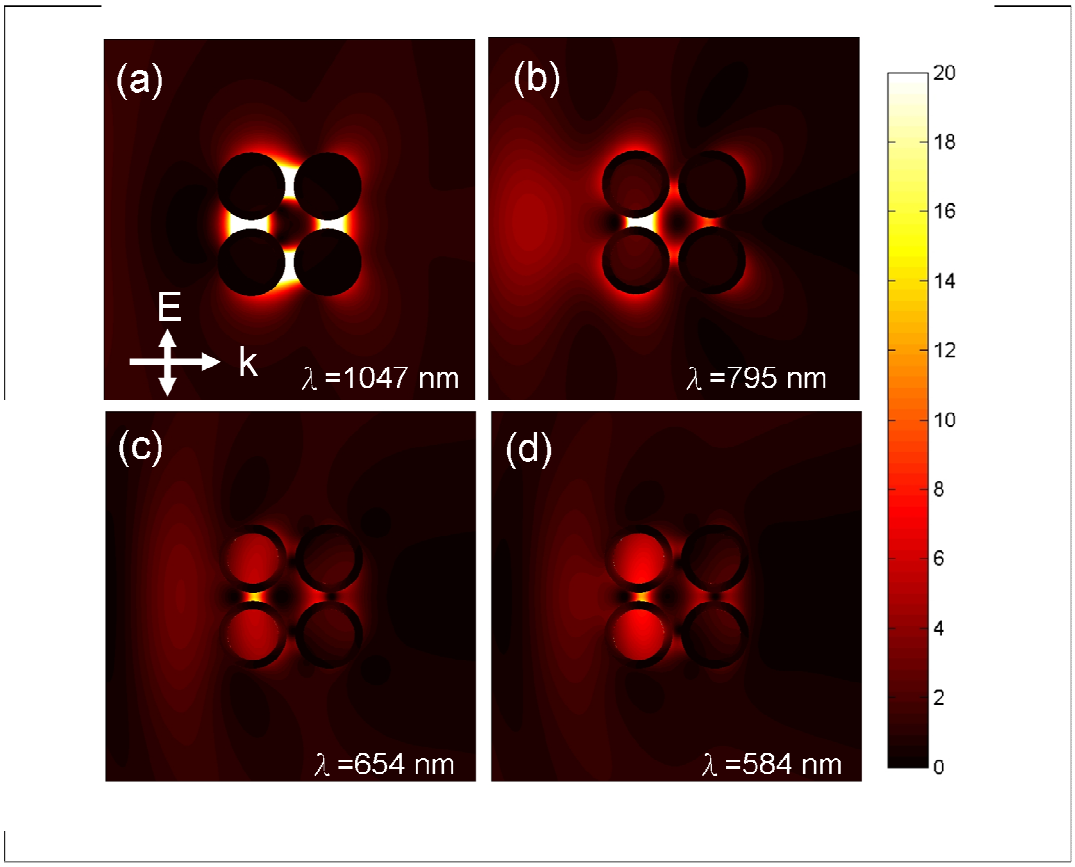

Figure 8.3 The normalized electric field intensity at the respective coupling plasmon modes wavelength of two silica-core gold-shell nanocylinder pairs with the same geometry shown in figure 8.2.

In the following sections, we will show that the plasmon modes of the two core-shell nanocylinder pairs can be tuned systematically by varying the gap-width d between the nanocylinder pair, pair-distance p between the pairs, the dielectric constant of the dielectric core inside the nanocylinders, and the surrounding medium. First, we simulate the two pairs by varying the gap-distance between the nanocylinder pair with the fixed pair-distance of 20nm. In figure 8.4(a), as the inter-cylinder distance decreases, the lightning-rod plasmon mode is red-shifted and enhanced due to the much stronger interaction of dipolar modes resulted from the electrons at the outer surface of the nanocylinders. As the intensity of this plasmon mode increases, the dramatically larger electric field concentrating in the gap of the nanocylinder pair. As for other plasmon modes resulted from the interactions of the individual core-shell nanocylinder par plasmon modes, the resonance wavelength and intensity almost remain the same. This is because the cavity mode inside the dielectric core has formed due to the enough effective length, which is similar to one-dimensional Fabre-Perot resonance mode. Therefore, these plasmon modes associated with the cavity mode don't change dramatically by outside of the nanocylinders.

Figure 8.4(b) shows that as pair-distance between the core-shell cylinder pairs decreases, the intensity of the plasmon mode, near 1100nm, decreases and red-shifted. The resonance energy shifts to lower energy because the two cylinder pairs oscillate in the out-of-phase way. As the pair-distance decrease, the static coulomb energy also decreases [10]. The interaction between the cylinder pairs gathers the energy flow inside the region between the pairs and this interaction also enhance backscattering effect [13]. However, the enhancement of the backscattering results in the reduction of the lightning

rod effect because the amount of the incident energy flow concentrating in the gap of the nanocylinder pair decreases.

We also simulate the two nanocylinder pair with different dielectric constants of dielectric cores in figure 8.4(c). We can find in this figure that as the refractive index of the dielectric core increases, the resonance energy of the plasmon modes reduces except for the lightning-rod plasmon mode. This is because for the core-shell nanocylinder pairs, the lightning-rod plasmon mode is only resulted from the electrons at the outer surface of the nanocylinders. A large real permittivity of the metal results in an efficient screening and thus results in a redshift of the plasmon energies [15]. The resonance energy of other plasmon modes associated with the electrons of the inner surface of the nanocylinders can be decreased by increasing the refractive index of the dielectric core. By the similar way, as we increases the refractive index of the surrounding medium in figure 8.4(d), the resonance energy of all the plasmon modes will decrease. This is because all the plasmon modes are dependent on the electrons at the outer surface of the nanocylinders. The simulation results of three nanocylinder pairs with different pair-distances p from 20nm to 2nm are shown in Figure 8.5(a), and the spectra become more complex. Two lightning-rod plasmon modes can be found in the infrared range in the extinction spectra and the resonance wavelengths are 979nm and 1218nm, respectively. From the electric intensity of these two plasmon modes shown in figure 8.5(b) and 8.5(c), we can be convinced that the two plasmon modes are resulted from to the dipolar coupling of three solid metallic pairs but with different charge distributions. A very interesting situation occurs when the wavelength of the incident light is 979nm, in which case the maximum electric field intensity occurs in the gap of the second pair. M. Y. Ng and W. C. Liu [9]

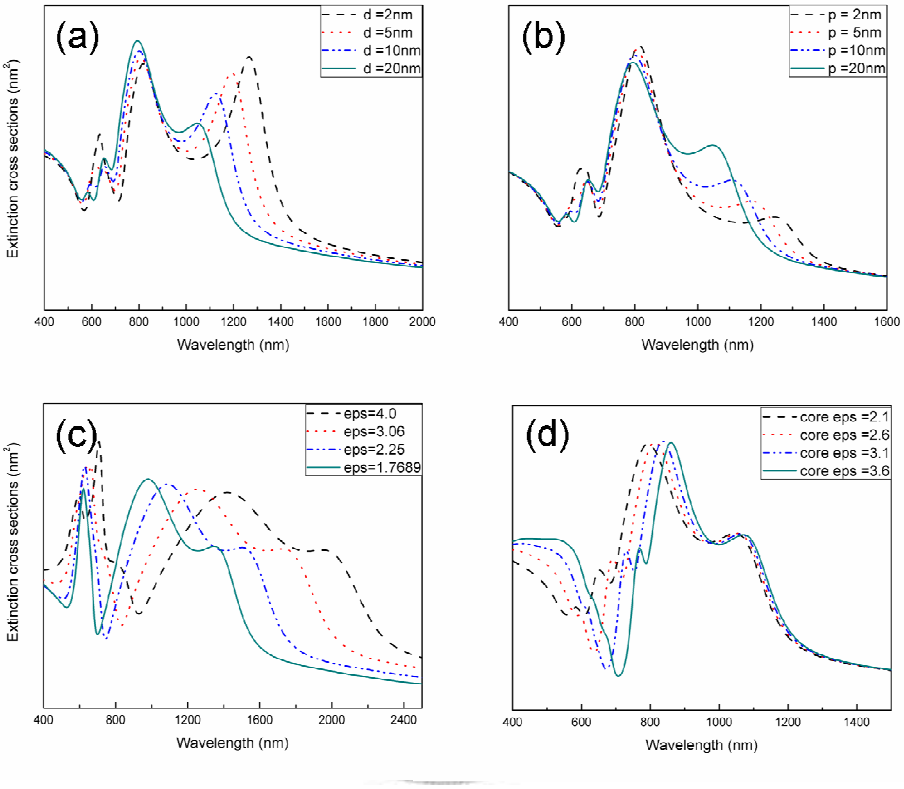

Figure 8.4 The dependence of the extinction spectra of two dielectric-core gold-shell nanocylinder pairs on dimensions. (a) For different gap widths between the nanocylinders with the pair distance p of 20nm, (b) for different pair-distances between the nanocylinder pairs with the gap width of 20nm, (c) for different dielectric constant of the dielectric cores, (d) for different surrounding medium.

pointed out that a cavity mode confined by three nanocylinder pairs can be found in the plasomonic spectra of the three-pair metallic nanocylinders. In this work, we find that such a cavity mode of three solid nanocylinder pairs is essentially the same as the lightning-rod mode near 979nm. Therefore, the multiple core-shell nanocylinder pairs show higher tenability than those of the solid nanocylinder pairs and we can know how the properties of the lighting-rod plasmon mode of three core-shell nanocylinder pairs are.

From the simulation results discussed above, we can understand that for the multiple nanocylinder pairs, how to control the light-rod plasmon modes and other plasmon modes resulted from coupling of the individual core-shell nanocylinders. Multiple nanocylinder pairs can provide the enhancement of the electric field intensity on the gap between the nanocylinder pair in the spectra from visible to infrared region. Therefore, they efficiently combine two surface-enhanced Raman scattering and surface enhanced infrared absorption substrates on a single substrate.

8.4 Conclusion

In conclusion, the plasmonic properties of multiple nanocylinder pairs are investigated by two-dimensional finite-difference time-domain method. The lightning-rod effect on the interactions between the dipolar modes of nanocylinders results in a longer wavelength plasmon mode in the infrared region. Other plasmon modes of multiple nanocylinder pairs are resulted from the interactions between the essential a single core-shell nanocylinder plasmon modes. We can systematically control the strength and resonance energy of these plasmon modes by varying the pair-distance between the pairs, the gap-distance between the pair, the optical constant of the dielectric-core, and

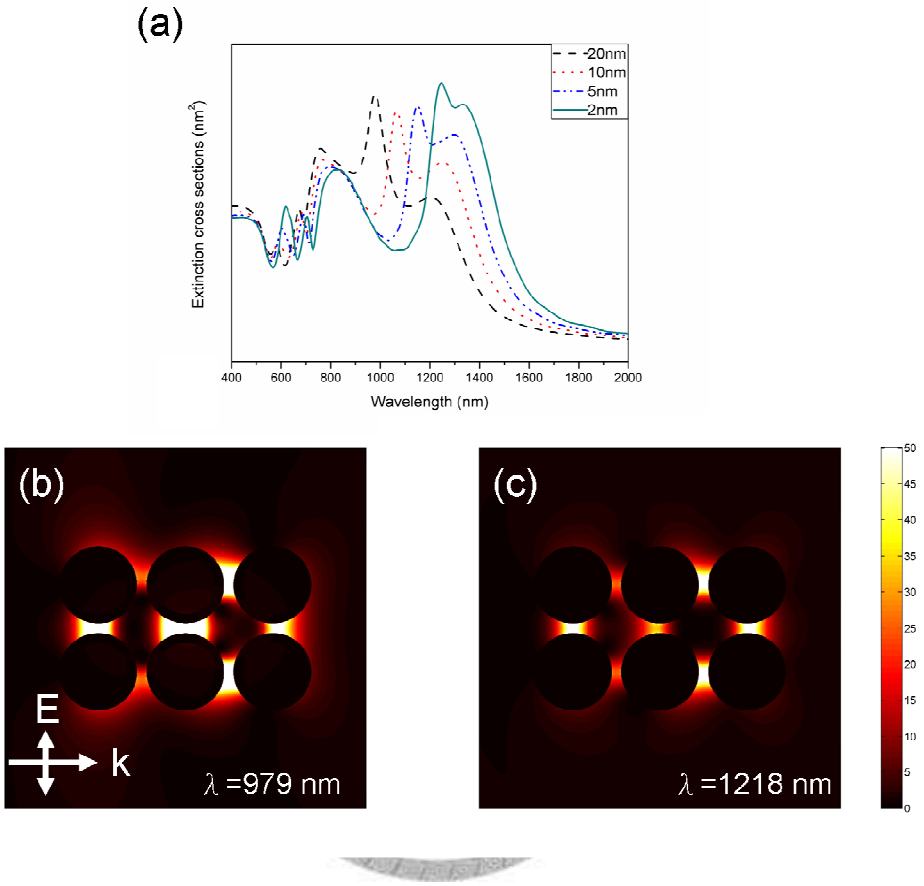

Figure 8.5 (a) The dependence of the extinction spectra on the pair distance between the three nanocylinder pairs. (b) For the pair distance of 20nm, the electric field intensity at the wavelength of 979 nm. (c) For the pair distance of 20nm, the electric field intensity at the wavelength of 1218 nm.

surrounding medium. Therefore, the core-shell nanocylinder pairs possess an ideal property which can enhance the electric field intensity at the same spatial positions in the wide wavelength range between the visible to infrared regions. From simulation results we can find that for normal incidence, the diffraction spectra of multiple cylinder pairs contain the lightning-rod plasmon mode, and the electric field intensity is concentrated in the gap between the nanocylinder pair in the infrared region. The resonance wavelength and local field enhancement of this plasmon mode can be tuned by varying the pair-distance between the pairs, the gap-distance between the pair, the optical constant of the dielectric-core, and surrounding medium. The large electric field intensity in the infrared region at long wavelength makes multiple core-shell cylinders an ideal candidate for surface enhanced spectroscopies.

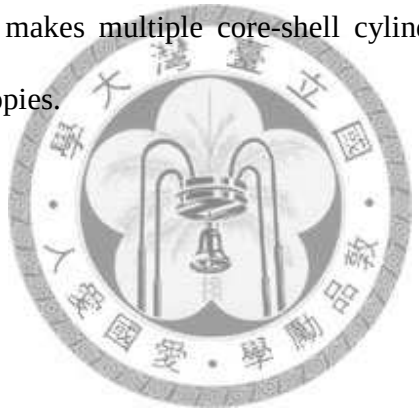

References

[1] J. Aizpurua, P. Hanarp, D. S. Sutherland, M. Kall, G. W. Bryant, and F. J. Garcia de Abajp, Phys. Rev. Lett. **90**, 057401 (2004).

[2] E. Prodan, C. Radloff, N. J. Halas, and P. Norlander, Science **302**, 419 (2003) .

[3] S. Ushioda and Y. Sasaki, Phys. Rev. B **27**, 1401 (1983).

[4] P. C. Lee and D. Meisel, J. Phys. Chem. **86**, 3391 (1982).

[5] J. Kundu, F. Le, P. Nordlander, and N. J. Halas, Chem. Phys. Lett. **452,** 115 (2008).

[6] J.B. Lassiter, J. Aizpurua, L.I. Hernandez, D.W. Brandl, I. Romero, S. Lal, J.H. Hafner, P. Nordlander, and N.J. Halas, Nano Lett. **8**, 1212 (2008).

[7] M. Y. Ng and W. C. Liu, Opt. Express **14**, 9422 (2003).

[8] H. A. Yousif, R. E. Mattis, and K. Kozminski, Appl. Opt. **9**, 4012 (1994).

[9] J. Y. Lu and Y. H. Chang, Superlattices Microstruct. **47**, 60 (2010).

[10] P. B. Johnson and R. W. Christy, Phys. Rev. B **6,** 4370 (1972).

[11] C. Radloff and N. J. Halas, Nano Lett. **4** , 1323 (2004).

[12] J. Y. Lu, Y. H. Chang, Physica E,doi:10.1016/j.physe.2009.12.010.

[13] H. Y. She, L. W. Li, S. J. Chua, W. B. Ewe, O. J. F. Martin, and J. R. Mosig, J. Appl. Phys. **104**, 064310 (2008).

[14] J. Y. Lu and Y. H. Chang, Opt. Commun. **283**, 2627 (2010).

[15] H. Wang, F.Tam, N. K. Grady, and N. J. Halas, J. Phys. Chem. B **109**, 18218 (2005).

Chapter 9

Conclusions

In this dissertation, we have realized the acceleration of finite-difference time-domain (FDTD) by using graphics processor units (GPU). Compared with the CPU-Based FDTD, the GPU-Based FDTD is about 25 times faster. The FDTD has an advantage that it can get full spectra in a single simulation, but it requires a good analytical model for description of the dispersion of materials. In order to obtain such an analytical dispersion model, we develop the three critical point poles model, which can get a better fit for gold and silver in a wide wavelength ranges between 180nm and 2000nm. This efficient dielectric function was implemented into our GPU-Based FDTD to simulate the localized plasmon modes in the core-shell nanocylinders.

In chapter 5, the plasmon modes of a single dielectric-core gold-shell nanocylinder pair is studied. The simulation results show that for polarization direction parallel to the axis of the pair, the plasmon modes of a dielectric-core gold-shell nanocylinder pair could contain an in-phase dipolar plasmon mode. The in-phase dipolar mode is from the electrons at outer surfaces of the nanocylinder pair due to the lightning-rod effect. Thus we can infer two important factors that give rise to intense electric field can be utilized for the surface enhanced spectrospies: one is hybridized plasmon modes and the other is the lightning-rod effect.

In chapter 6, the retardation effect on the plasmon modes of a single silica-core gold-shell nanocylinder pair is studied. We show that for light polarized perpendicular to the

axis connecting the pair, the spectrum depends sensitively on the size of nanocylinder pair. As the size increases, several retardation-induced non-dipolar plasmon modes including multipolar modes appear in the spectrum and the resonance wavelength and strength of its plasmon modes can be tuned by changing separation width between the nanocylinder pair.

In addition to the electric field distributions and extinction spectra, the energy flow associated with two closely spaced core-shell nanocylinders are discussed in chapter 7. Four zero energy (optical singular) points appear in the energy flow diagram: two saddle points and two optical vortices. Among these four points, the saddle points are outside the cylinders and the optical vortices are inside the cylinders. Both the width of the gap between the nanocylinder pair and the value of the permittivity of the dielectric core are found to have strong influence on the rotating direction of the optical vortices. The gap width between the nanocylinder pair affects the energy distribution near the nanocylinders and that in turn determines the rotational type of the optical vortices. The permittivity of the dielectric core determines the magnitude of the EM field intensity inside the nanocylinders and thus can be used to control the energy flow direction inside the nanocylinders. Our studies show for the first time that optical vortices can be found in a core-shell nanocylinder pair and the rotating direction of the optical vortices associated with the nanocylinder pair can be controlled by changing either the spacing between the nanocylinder pair or by changing the permittivity of the dielectric core.

In chapter 8, the optical properties of multiple core-shell nanocylinder pairs are studied. We can find that for normal incidence, the diffraction spectra of multiple cylinder pairs contain the lightning-rod plasmon mode and hybridized plasmon modes. The electric

field intensity of the lightning-rod plasmon mode is concentrated in the gap between the nanocylinder pair in the infrared region. The resonance wavelength and local field enhancement of this plasmon mode can be tuned by varying the pair-distance between the pairs, the gap-distance between the pair, the optical constant of the dielectric-core, and surrounding medium. Therefore, multiple nanocylinder pairs can provide the enhancement of the electric field intensity on the gap between the nanocylinder pair in the spectra from visible to infrared region. Therefore, they efficiently combine two surface-enhanced Raman scattering and surface enhanced infrared absorption substrates on a single substrate.

Appendix A

For the stimulation window, Δx is the spatial size and Δt is the temporal time. In order to implement the CP3 model into FDTD method, we introduce the new vector field Ψ_{CP} known as the recursive accumulators and the update equations become

$$\vec{\Psi}_{CP1}\Big|^{n} = C_{cp1}^{\rho}\vec{\Psi}_{CP1}\Big|^{n-1} + C_{cp1}^{\delta}\vec{E}\Big|^{n} \tag{A1}$$

$$\vec{\Psi}_{CP2}\Big|^{n} = C_{cp2}^{\rho}\vec{\Psi}_{CP2}\Big|^{n-1} + C_{cp2}^{\delta}\vec{E}\Big|^{n} \tag{A2}$$

$$\vec{\Psi}_{CP3}\Big|^{n} = C_{cp3}^{\rho}\vec{\Psi}_{CP3}\Big|^{n-1} + C_{cp3}^{\delta}\vec{E}\Big|^{n} \tag{A3}$$

$$E\Big|^{n+1} = C^{\alpha}\vec{E}\Big|^{n} + C^{\beta}\nabla\times\vec{H}\Big|^{n+1/2} + C^{\gamma}\mathrm{Re}(\vec{\Psi}_{CP1}\Big|^{n} + \vec{\Psi}_{CP2}\Big|^{n} + \vec{\Psi}_{CP3}\Big|^{n}) \tag{A4}$$

$$\vec{H}\Big|^{n+3/2} = \vec{H}\Big|^{n+1/2} + \frac{\Delta t}{\mu_0 \Delta x}\nabla\times\vec{E}\Big|^{n+1} \tag{A5}$$

The coefficients defined for the update equations of Ψ_{CP} and the electric field $\vec{E}$ in equations (A1-A3) are as follows:

$$C_{cpm}^{\rho} = -\mathrm{i}\frac{2\mathrm{A_m}\Omega_\mathrm{m}\,\mathrm{e}^{(-\mathrm{i}\phi_\mathrm{m})}}{\Gamma_\mathrm{m}-\mathrm{i}\Omega_\mathrm{m}}(1-\mathrm{e}^{(-\Gamma_\mathrm{m}+\mathrm{i}\Omega_\mathrm{m})\Delta t})^2 \qquad \mathrm{m}=1\sim3 \tag{A6}$$

$$C_{cpm}^{\delta} = \mathrm{e}^{(-\Gamma_\mathrm{m}+\mathrm{i}\Omega_\mathrm{m})\Delta t} \qquad \mathrm{m}=1\sim3 \tag{A7}$$

The constants $\mathrm{A_m}$, Ω_m, Γ_m, σ, and ϕ_m in the CP3 model can be obtained in Table 4.1, and we define the χ_0 used in the update equation (A4) of the electric field $\vec{E}$

$$\chi_0 = -\sigma\Delta t + \mathrm{Re}\left[\sum_{\mathrm{m}=1}^{3} -\mathrm{i}\frac{\mathrm{A_m}\Omega_\mathrm{m}\mathrm{e}^{-\mathrm{i}\phi_\mathrm{m}}}{\Gamma_\mathrm{m}-\mathrm{i}\Omega_\mathrm{m}}(1-\mathrm{e}^{(-\Gamma_\mathrm{m}+\mathrm{i}\Omega_\mathrm{m})\Delta t})\right] \tag{A8}$$

The ε_0 is the permittivity of free space, and μ_0 is the magnetic permeability of free space, and C^{α}, C^{β} and C^{γ} for the update equations (A5-A6) of the electric field $\vec{E}$ and the magnetic field $\vec{H}$ are as follows:

$$C^{\alpha} = \frac{\varepsilon_{\infty}}{\varepsilon_{\infty} + \chi_0} \tag{A9}$$

$$C^{\beta} = \frac{\Delta t}{\Delta x \varepsilon_0 (\varepsilon_{\infty} + \chi_0)} \tag{A10}$$

$$C^{\gamma} = \frac{1}{\varepsilon_{\infty} + \chi_0} \tag{A11}$$